

AD-A119 906

DELAWARE UNIV. NEWARK DEPT OF CIVIL ENGINEERING

F/O 8/3

WAVE KINEMATICS AND SEDIMENT SUSPENSION AT WAVE

BREAKING POINT. (U)

JUN 82 P. A. HWANG, H. WANG

N00014-81-K-0297

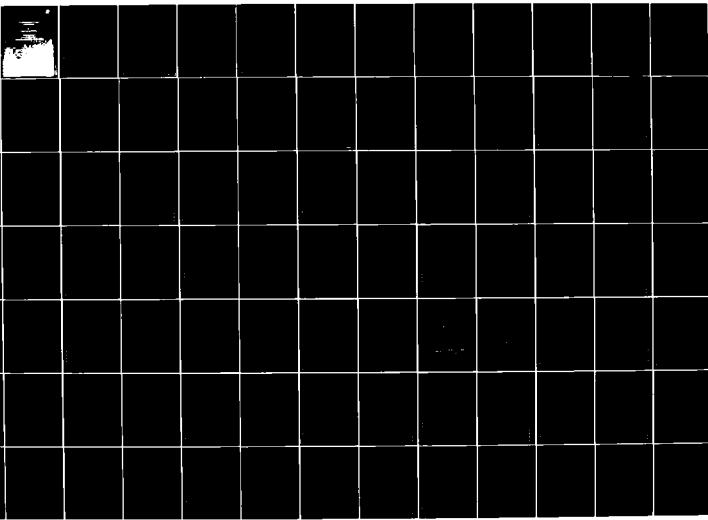
UNCLASSIFIED

CE-82-27

NL

1 of 2

100k



AD A119906

WAVE KINEMATICS AND SEDIMENT SUSPENSION

AT WAVE BREAKING POINT

By

Paul Anche Hwang and Hsiang Wang

Technical Report No. 13

Contract No. N00014-81-K-0297

with the Office of Naval Research, Geography Programs

RESEARCH REPORT CE-82-27

June 1982

Ocean Engineering Program

Department of Civil Engineering

University of Delaware

Newark, Delaware

19711

DISTRIBUTION STATEMENT A  
Approved for public release;  
Distribution Unlimited

ABSTRACT

↓  
The flow field and sediment suspension at wave breaking point were studied in the laboratory.

The flow field concerns mainly the drift velocity on sloping beach. The drift velocity profiles as well as the mean drift velocity strength were established through laboratory measurements. Various existing theories were examined and compared with laboratory results.

A sediment suspension model was proposed based on the diffusion model including the considerations of the fall velocity reduction in an oscillatory flow field, the sediment grading, and the degree of agitation in the flow field. The model reduced the dependence of the data-fitted coefficients to a minimum. Comparison of this model with data from various sources was made. The results are encouraging.



Accession For	<input checked="" type="checkbox"/>	<input type="checkbox"/>	<input type="checkbox"/>
NTIS GRA&I			
DTIC TAB			
Unannounced			
Justification			
By			
Distribution/			
Availability Codes			
Avail and/or			
Dist Special			
			A

The breaking wave spectra in a finite water depth were discussed. A modified Wallops spectral model using finite depth Stokes waves and cnoidal or solitary waves for different ranges of water depths was suggested. The model was also extended by using the stream function wave theory which was found to give the most satisfactory results on the wave spectral prediction both in terms of the variance and the spectral shape.



## TABLE OF CONTENTS

	Page
ACKNOWLEDGEMENT	iii
ABSTRACT	iv
TABLE OF CONTENTS	vi
LIST OF FIGURES	viii
LIST OF SYMBOLS AND SUBSCRIPTS	xii
1 INTRODUCTION	1
2 MEAN DRIFT VELOCITY AT BREAKING POINT	3
2.1 Introduction	3
2.2 Laboratory Experiment	7
2.2.1 Experimentation	7
2.2.2 Laboratory Results	14
2.2.3 Vertical Distributions	19
2.3 Mean Offshore Drift Velocity	26
2.4 Results and Comparison	36
2.5 Conclusion	44
3 SUSPENDED SEDIMENTS	46
3.1 Introduction	46

3.2	Field Experiment	49
3.3	Laboratory Experiment	67
3.4	On the Theory of Vertical Concentration Distribution	69
3.5	Diffusion Coefficient Selection	79
3.6	Fall Velocity Reduction	86
3.7	Determination of Reference Level $z_0$	90
3.8	Field and Laboratory Data Presentation	93
4	BREAKING WAVE PROFILES AND PARTICLE VELOCITIES	110
4.1	Introduction	110
4.2	A Brief Summary of the Wallops Spectral Model	111
4.3	Wallops Spectrum in Finite Depth Water	113
4.4	Velocity Spectra	126
4.5	Comparison with Observations	128
5	CONCLUSION AND RECOMMENDATIONS	143
	REFERENCES	147
APPENDIX	LAGRANGIAN MASS TRANSPORT BY STREAM FUNCTION THEORY	154

## LIST OF FIGURES

<u>Figures</u>	<u>Caption</u>	<u>Page</u>
2.1	Definition of breaking wave	6
2.2	Test range in terms of relative water depth criterion	10
2.3	Breaker types in terms of the surf parameter	10
2.4	Schematic diagram showing measuring apparatus	12
2.5	Examples of tracer trajectories	13
2.6	Definition of mean drift velocity	15
2.7	Areal distributions of drift velocities and of locally averaged values	16
2.8	Isolines of drift velocity near the breaking point	18
2.9	Vertical distribution of drift velocity at the breaking point	20
2.10	Comparison of shapes of drift velocity profiles	21
2.11	Coordinate system	27
2.12	Limits of offshore drift depths, $h_1$ , $h_2$	35
2.13	Results of mean offshore drift velocity vs. $kh$	39
2.14	Results of mean offshore drift velocity vs. $u^2$	40

2.15 Effects of bottom slope on mean offshore drift velocity	43
3.1 Site location and area hydrograph	51
3.2 Suspended sediment pump sampler	52
3.3 Suspended sediment bottle sampler	55
3.4 Instrument arrangement at test site	56
3.5 Concentration profiles of September 3, 1978 experiment	60
3.6 Beach profile and sediment size distribution (September 3, 1978)	61
3.7 Beach profiles and sediment size distribution (September 26-28, 1979)	66
3.8 Conceptual sketch of mechanisms that generate high concentration at higher elevation	76
3.9 Functional relationship of the concentration profiles with $z_0/h$ , $V$ and $w_0/H\sigma$	85
3.10 Fall velocity reduction in an oscillating flow field	89
3.11 Reference concentration at boundary layer level as a function of Shields parameter	92
3.12 Comparison of the suspension model with the present laboratory data	95
3.13 Goodness of fit of the experimental data with the theoretical results	101
3.14 Comparison of the suspension model with North Sea data	102
3.15 Comparison of the suspension model with data from Nielsen & Green (1981)	104

3.16 Concentration profiles under breaking and nonbreaking waves. (from Fig. 6.25, Nielsen, 1979)	106
3.17 Comparison of different sediment suspension models with experimental data	108
4.1 Variation of $m$ and $\xi$ based on Stokes finite depth wave theory	115
4.2 Variation of $\beta$ as a function of $kh$ and $\xi$	116
4.3 RMS variance of cnoidal and solitary waves vs. $Ur$	124
4.4 Spectral slopes as a function of $Ur$ (spilling breakers)	129
4.5 Comparison of $\eta$ , $u$ and $w$ spectra with various theories	131
4.6 Harmonic amplitudes vs. $kh$	138
4.7 Comparison of linear and stream function wave theories: total variance	139
I-1 Comparison of stream function drift velocity with Stokes solution	161

LIST OF TABLES

<u>Table</u>	<u>Caption</u>	<u>Page</u>
2.1	Laboratory test conditions of drift velocity experiment	8
2.2	Mean drift by stream function theory	34
2.3	Offshore drift velocity summary	38
3.1	Suspended sediment pump data (September 3, 1978)	58
3.2	Field conditions (September 3, 1978)	59
3.3	Suspended sediment pump data (September 26-27, 1979)	62
3.4	Suspended sediment bottle data (September 26-27, 1979)	63
3.5	Field conditions (September 26-27, 1979)	64
3.6	Wave conditions of sediment experiment	70
3.7	Summary of $\epsilon$ and the resulting C profiles	75
I .1	Lagrangian vs. Eulerian mass transport	158
I .2	Comparison between mass transport by Stokes theory and stream function theory	160

## LIST OF SYMBOLS AND SUBSCRIPTS

### SYMBOLS

- a Wave amplitude; Fourier coefficients (even)
- b Fourier coefficients (odd)
- C Suspended sediment concentration
- c Wave celerity; Fourier harmonic coefficients
- d Sediment diameter
- E Wave energy; Complete elliptic integral of the second kind
- F Dimensionless depth averaged return flow velocity
- f Shape function of drift velocity; drag coefficient
- G Gravity force
- g Gravitational acceleration
- H Wave height
- h Water depth
- K Complete elliptic integral of the first kind
- k Wave number
- L Wave length
- l Length scale
- M Mass transport

m Spectral slope  
 q Nome of complete elliptic integral  
 R Coefficient of fall velocity reduction  
 S Spectrum  
 s bottom slope  
 T Wave period  
 t Time coordinate  
 U Mean velocity  
 Ur Ursell number ( $=\bar{\eta}^3/k^2h^3$ )  
 Ur' Ursell number ( $=H/k^2h^3$ )  
 u Horizontal velocity (in x-direction)  
 V Variance of sediment distribution  
 v Vertical velocity (in z-direction)  
 W Amplitude of vertical velocity in an oscillating flow  
 w Particle fall velocity  
 X Stream function coefficients  
 x Longitudinal space coordinate  
 y Cross-sectional space coordinate  
 z Vertical coordinate  
 $\beta$  Coefficient for spectral model  
 $\delta$  Boundary layer thickness  
 $\epsilon$  Eddy viscosity  
 $\eta$  Surface elevation  
 $\eta_r$  Ripple amplitude

$\kappa$  Ripple wave number  
 $\lambda_r$  Ripple length  
 $\Psi$  Shields parameter  
 $\psi$  Stream function  
 $\nu$  Kinematic viscosity  
 $\xi$  Horizontal particle excursion amplitude  
 $\zeta$  Vertical particle excursion amplitude  
 $\sigma$  Wave angular frequency  
 $\tau$  Shear stress  
 $\Phi$  Phase lag; velocity potential  
 $\theta$  Phase function ( $=kx-\sigma t$ )  
 $\delta$  Significant wave slope

SUBSCRIPTS

b bottom; breaking  
 c Cnoidal theory  
 o Reference properties  
 s Solitary theory; sediment properties  
 T Stokes theory  
 w Wave properties  
 ' Turbulent properties

## CHAPTER 1 INTRODUCTION

It is a common practice to treat the breaking point as a natural boundary for various studies of surf zone problems. The breaking point itself, however, has not been widely investigated. In an attempt to obtain a clearer understanding of this region, the author studied the Lagrangian drift velocity, the vertical and horizontal velocities, the wave forms and the sediment suspension at this specific location. Due to the diverse nature of the problems involved, the literature review and theoretical derivations of each topic were included in respective chapter that deals with the specific topic.

Two sets of laboratory experiments were conducted for the research. Chapter 2 deals with the drift experiment and its results. Chapter 3 describes the sediment experiments which collected simultaneous data of surface elevation, vertical and horizontal velocities and

Island of Sylt, West Germany are also discussed in that chapter. A sediment suspension model based upon turbulent diffusion is presented for the core region of the wave field. The comparison of the model results with present experiments as well as experiments by other investigators were discussed.

Chapter 4 studied the wave and velocity spectra. A modification of Wallops spectral model using finite depth Stokes wave theory, cnoidal theory, solitary theory and stream function wave theory is proposed for finite depth water application. However, the direct spectra of the stream function generated waves are found most satisfactory both in terms of the total variance and the spectral shape. The comparison of wave and velocity spectra of various wave theories with those of the collected data are presented.

The last chapter presented the conclusion for the entire study and recommendations for future studies.

## CHAPTER 2 MEAN DRIFT VELOCITY

### 2.1 Introduction

Drift velocity in a wave field is the velocity of a mean current resulting from open orbital motions of water particles. It plays an important role in material transport in the nearshore zone and is also known as the mass transport velocity. Stokes (1847) was the first to point out this property and treated the problem analytically for a channel of infinite length and constant depth. His solution, based upon classic second-order wave theory, resulted in a mean flow in the direction of wave propagation.

Longuet-Higgins (1953) treated the problem in a finite-length channel with due consideration of fluid viscosity in the surface and bottom boundaries. His solution indicated that the drift velocity is in the direction of wave propagation near the surface and the bottom but against the wave in the middle section. Later on, Huang (1970), Wang and Liang (1975), Mei et al.

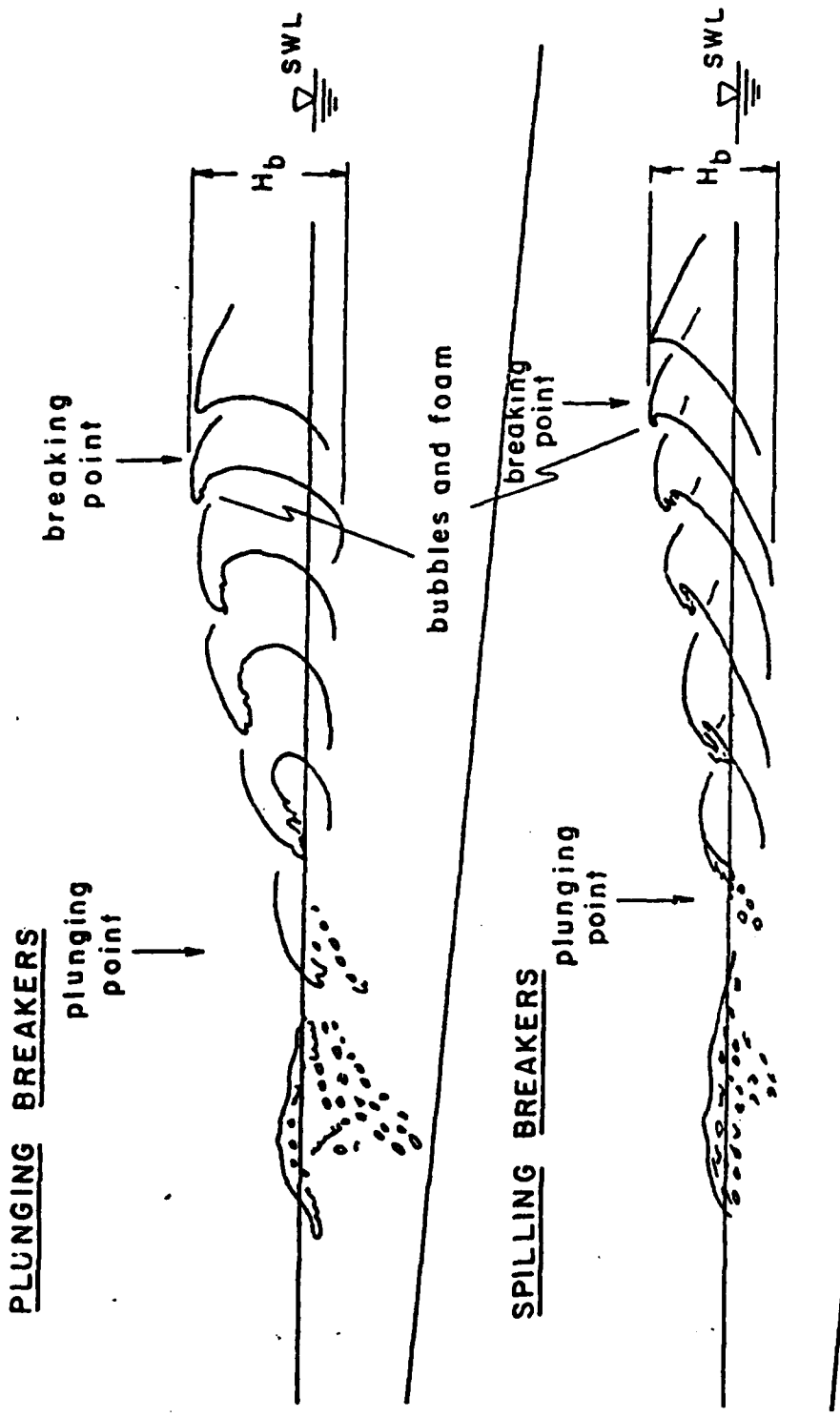
(1972) and Dalrymple (1976) carried out further analytical studies, all of them dealing with finite channel of horizontal bottoms. The drift velocity distributions obtained by them, except Dalrymple's are all similar to that of Longuet-Higgins. Dalrymple's formulation was based on Dean's (1965) stream function theory and his solution was in the Eulerian sense as opposed to the Lagrangian drift velocity used by the other investigators. The Lagrangian drift velocity using stream function theory is developed in this study. The drift velocity profile is similar to that of the Stokes.

Experimentally, Russell and Osorio (1957) and Mei et al. (1972) measured drift velocity distribution in a horizontal finite-length channel. Bijker et al. (1974) investigated the influence of bottom slope on drift velocity. Most of their measurements were made before wave breaking with emphasis on near-bottom flow. For the bottom drift velocity, Bijker et al. modified Longuet-Higgins' solution by the incorporation of shoaling effect. The theoretical values, however, are found to be considerably larger than those obtained in the experiments.

The present wave tank study concentrated on measurements of the drift velocity at the breaking point under different types of breaking waves on a rigid plane beach. The difference in breaker types would probably influence the vertical drift velocity profile at the breaking point, which would in turn control the sediment transport pattern across the surf zone. An attempt is made here to clarify the drift velocity patterns under these breakers. The data are compared with existing theories.

Further comparison with theories is made for a depth averaged offshore drift velocity (defined in Eq. 2-3). The smoothing effect of the vertical integration eliminates some of the data scatter due to measurement. The theories thus agree far better.

For convenience of reference, we define (1) the breaking point as a starting point of wave breaking, which is characterized by the existence of maximum height of waves, usually showing the initiation of bubble and foam formation, and (2) the plunging point as a point where the shape of breaking waves completely disintegrate when their crest impinges against water (see Fig. 2.1). The drift velocity distributions were largely measured



$H_b$ : breaker height Fig.2.1. Definition of breaking wave.

within these limits. The material of this chapter appeared partially in Sunamura, et al. (1980) and Wang et al. (1982).

## 2.2 Laboratory Experiment

### 2.2.1 Experimentation

The experiment was conducted in a steel wave flume 26 m long, 0.5 m wide and 1.3 m deep. At one end is a Scotch Yoke piston type wave generator. A glass section 7 m long is located 10 m from the generator. A plane beach made of plywood coated with black paint was placed at the other end of the tank. Two beach slopes, 1/10 and 1/15, were used during the test. Sixteen runs of experiments were conducted with conditions listed in Table 2.1. The last three cases were difficult to obtain velocity profiles for, but the wave data are used in Chapter 4 for wave form analysis. For the rest of the chapter, the discussion is concerned with the first thirteen runs. Based upon the relative water depth criterion, i.e., the ratio of still water depth to wavelength at breaking,  $(h/L)_b$ , the test conditions were all in the lower end of the intermediate depth range

Table 2.1 Laboratory test conditions of drift experiment

case	T (sec)	H <sub>c</sub> (cm)	h <sub>c</sub> (cm)	H <sub>b</sub> (cm)	h <sub>b</sub> (cm)	$\bar{U}$ (cm/s)	s	kh type*
1	1.00	8.0	40.0	9.5	12.1	1.0	1/15	sp .760
2	1.33	11.7	40.0	14.0	18.3	2.2	1/15	sp .694
3	1.34	9.0	40.0	11.5	13.1	2.0	1/15	tr .570
4	1.47	11.9	40.0	14.5	18.6	2.3	1/15	tr .625
5	1.56	8.4	40.0	12.5	13.7	2.6	1/15	pl .495
6	1.65	13.6	40.0	16.5	18.3	2.6	1/15	pl .545
7	1.89	12.5	40.0	16.5	17.1	4.8	1/15	pl .454
8	1.22	10.0	35.0	11.7	14.0	0.9	1/10	pl .657
9	1.50	11.5	45.0	15.4	16.7	2.0	1/10	pl .576
10	1.58	11.0	35.0	12.4	13.0	2.4	1/10	pl .475
11	1.61	9.5	35.0	12.6	15.0	0.9	1/10	pl .502
12	1.80	8.0	35.0	12.4	13.5	1.5	1/10	pl .422
13	1.89	10.0	35.0	15.2	15.1	1.6	1/10	pl .425
14**	0.84	9.3	40.0	7.5	14.0		1/10	sp .972
15**	1.16	12.2	40.0	13.0	19.7		1/10	sp .818
16**	1.81	6.4	40.0	9.5	13.2		1/10	pl .407
17+	1.14	11.6++	+	11.9	15.3		1/35	sp .749
18+	2.21	11.5++	+	11.7	14.9		1/35	pl .379

\* sp: spilling                      \*\* no mean velocity profiles  
tr: transitional                ++ deep water wave height  
pl: plunging                        based on calculation

+ from Flick et al. (1981), no mean velocity profile,  
constant depth between 45 to 55 cm

close to shallow water condition (Fig. 2.2). As far as breaker types are concerned, two of the tests were spilling, nine of them were plunging breakers and the remaining two were transition types. These groupings were based upon the magnitudes of the surf zone parameter as suggested by Galvin (1968), Battjes (1974) and later amplified by Wang and Yang (1980). The surf zone parameter is a non-dimensional quantity defined as  $H / g T s$ , where  $H$  is the breaking wave height,  $T$  is the wave period,  $s$  is the bottom slope and  $g$  is the gravitational acceleration. The values of this parameter for the test conditions and the breaker type designations are shown in Fig. 2.3.

Input wave characteristics were recorded by a capacitance type wave gauge installed at a place of constant water depth 1.5 m in front of the beach toe. The wave-induced water particle movement near the breaking point was tracked by neutrally buoyant, polystyrene beads. These were yellow-colored with a diameter of approximately 2 mm. Not all the beads had exactly the same density as the water which actually resulted in a more uniform vertical distribution of beads in the water column.

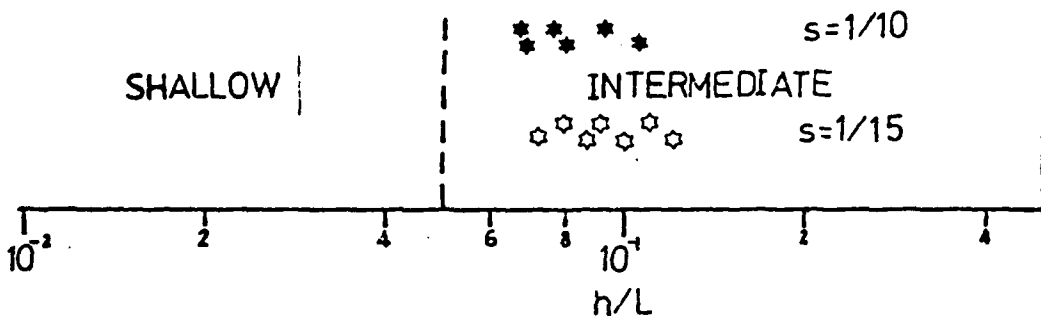


Fig.22. Test range in terms of relative water depth criterion.

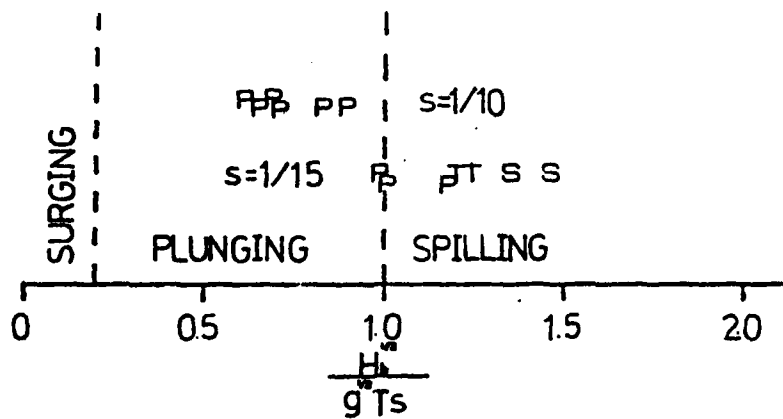


Fig.23. Breaker types in terms of surf parameter.

Fig. 2.4 illustrated the apparatus at the measuring section. The neutrally buoyant particles were mixed with water in a tracer feeder made of a transparent plastic tube with an outer diameter of 1 cm. One tapered end of the feeder was placed on the bottom under the breaking point, while the other end was connected to a rubber ball by a rubber tube. By squeezing the ball during wave action, many tracers were ejected from the feeder tip into the water. Some tracers, slightly lighter than water, went up slowly, so that almost uniform tracer-distribution around the breaking point was attained in a few wave cycles after the ejection.

The movement of the tracers was filmed, over 10 or more consecutive wave cycles for each run, by using a 16 mm movie camera (Bolex H-16 EBM Electric) operated at a speed of 24 and 25 frames/sec for 1/15 and 1/10 beach slopes, respectively. Color films (Kodachrome 40) were used. A 100 mm telephoto lens was applied to reduce the parallax.

The trajectories of beads were traced, as many as practical, from the films with the aid of a film analyzer (L-W International, Model 224A). Examples of trajectory diagrams are shown in Fig. 2.5. Greater turbulence

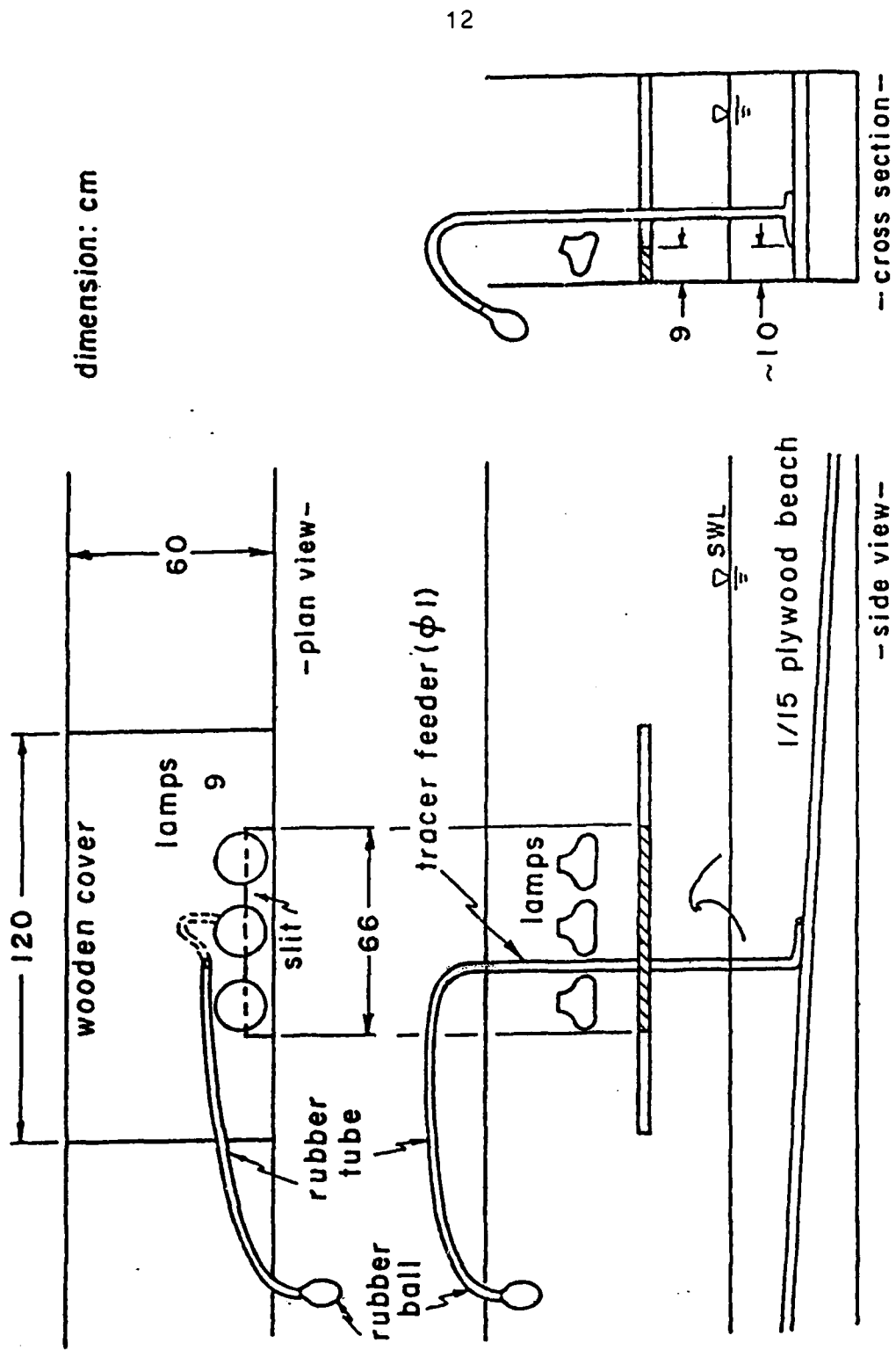
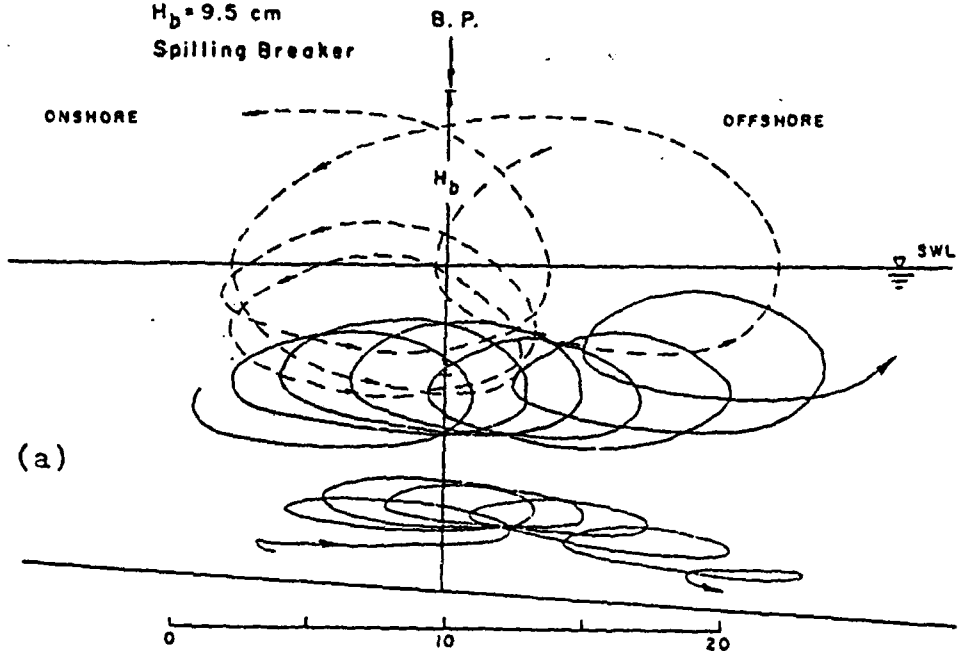


Fig.2.4. Schematic diagram showing measuring apparatus.

Run 1  
T=1.0 sec  
H<sub>b</sub>=9.5 cm  
Spilling Breaker



Run 7  
T=1.89 sec  
H<sub>b</sub>=15.5 cm  
Plunging Breaker

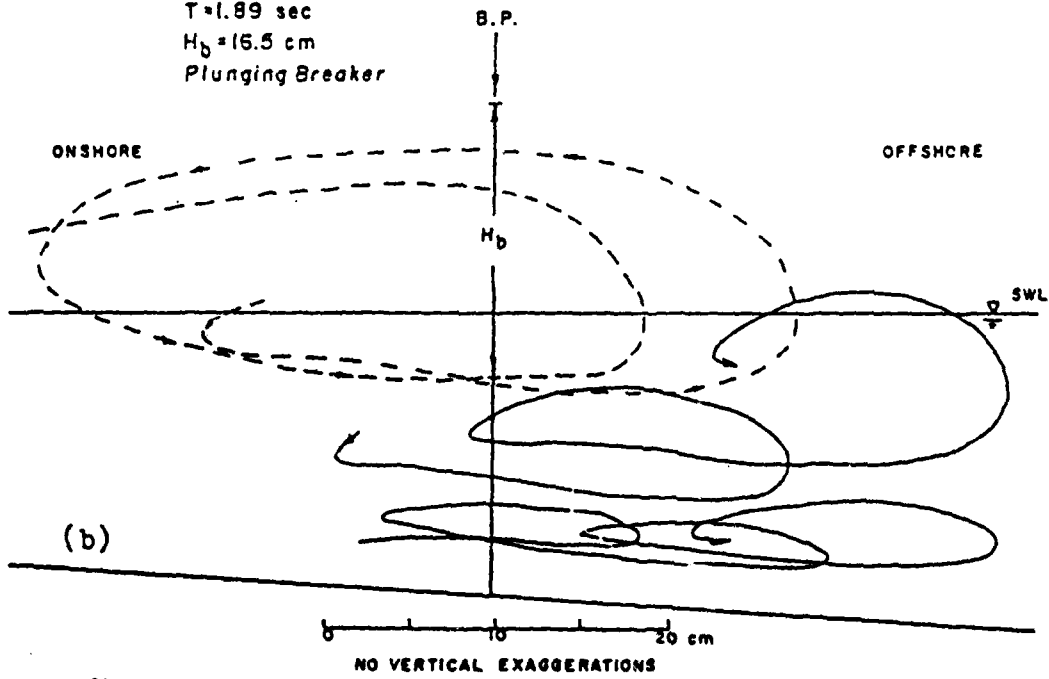


Fig. 75 Some of tracer trajectories

caused by water-mass impinging at the plunging point, particularly in the case of plunging breakers of larger heights, affected the two-dimensionality of the flow field in the vicinity of the breaking point, thus influencing the movement of the tracers. Consequently, long term trajectory tracing was difficult in the plunging breaker cases (compare Figs. 2.5a and 2.5b).

Fig. 2.6 shows the definition of mean drift velocity,  $U$ , used in our data analysis at a point,  $(x/2, y/2)$ :  $U=(a+b)/2T$ , where  $T$  is the wave period,  $a$  and  $b$  are the displacements of a tracer measured with positive values in the offshore direction, and  $x$  and  $y$  are horizontal and vertical dimensions of the trajectory under consideration, respectively. Since the mean drift velocity obtained from the trajectory diagrams showed considerable spatial scatter (Fig. 2.7 as an example, the variance of the scatter is about 40%), local averaging was done by grouping the data as demonstrated by dashed closures in Fig. 2.7. Some ambiguity remained in the selection of averaging areas.

### 2.2.2 Laboratory Results

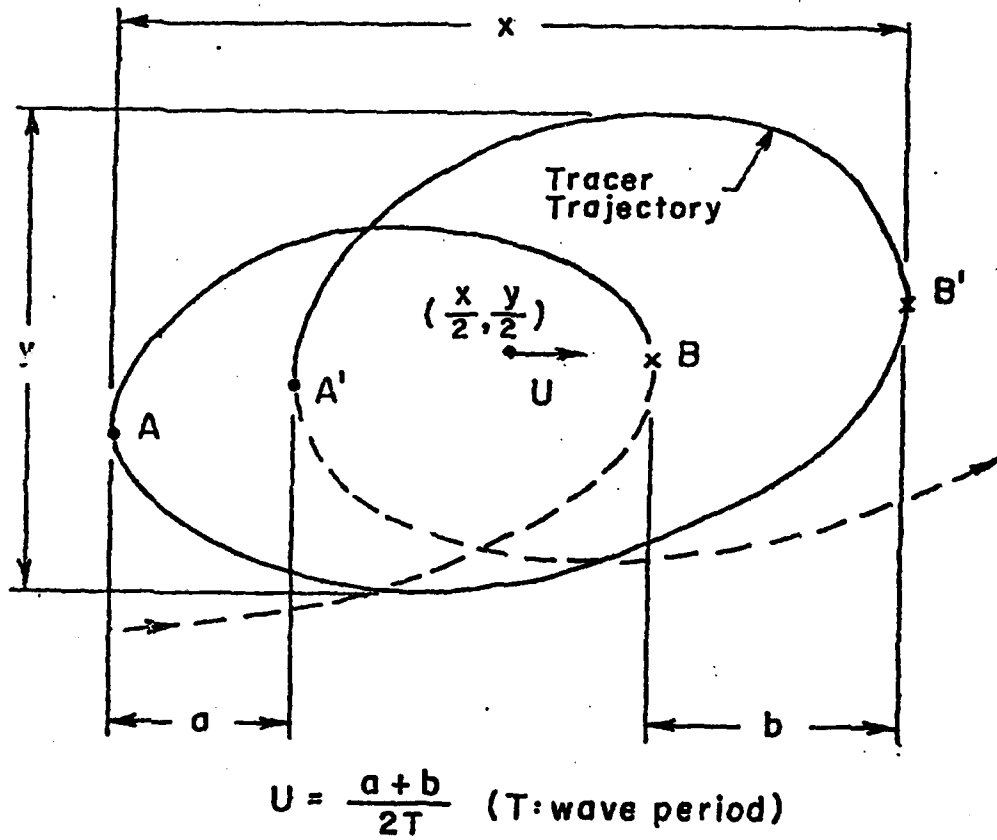


Fig.26. Definition of mean drift velocity,  $U$ .

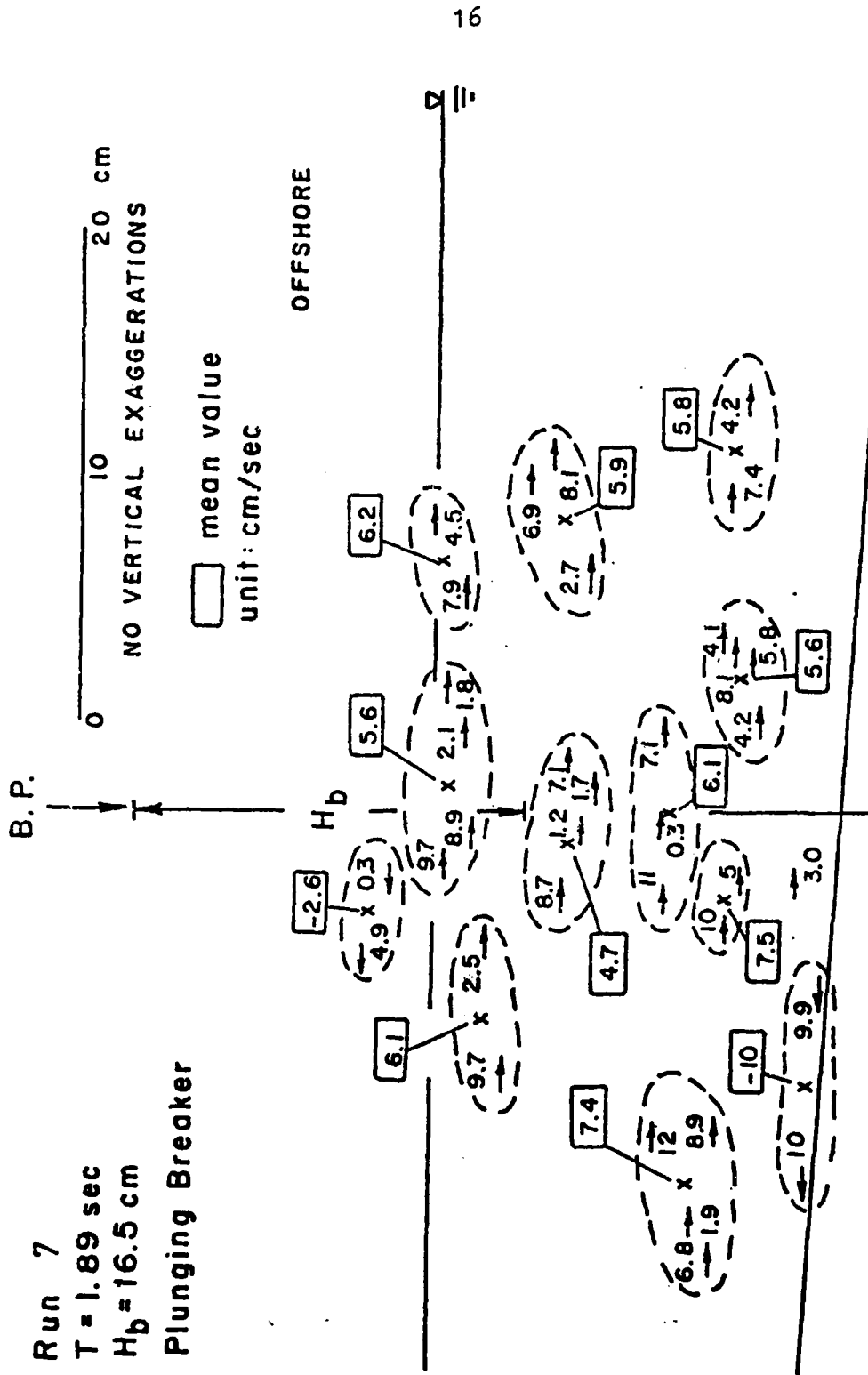


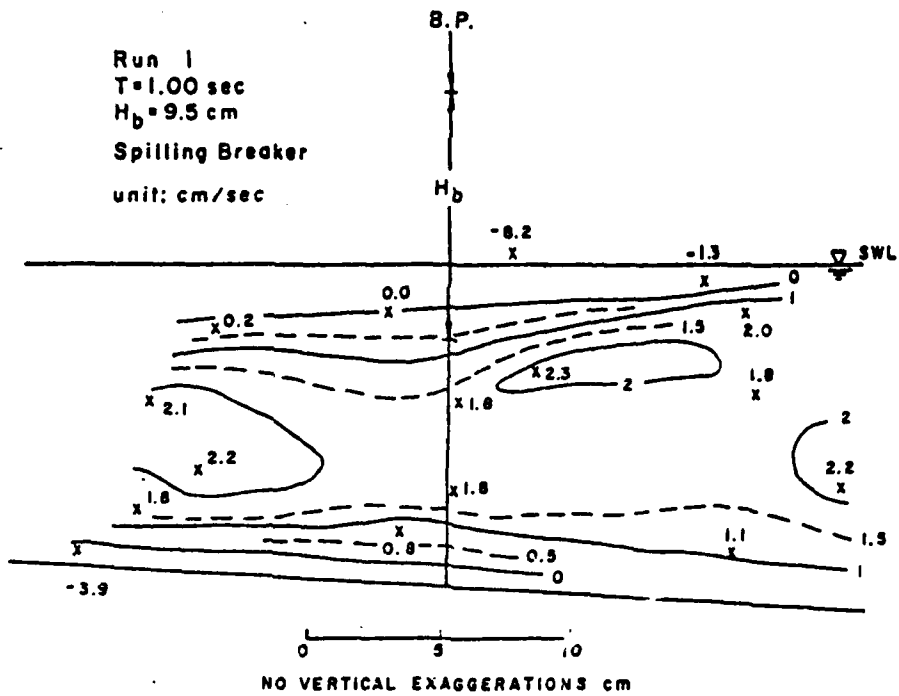
Fig. 37. Areal distributions of drift velocities and of locally averaged values.

On the basis of the locally averaged values, isolines were drawn to indicate drift velocity distribution near the breaking point. The result is illustrated in Fig. 2.8, in which offshore drift is chosen as positive.

The lack of data points near the bottom is partially due to the difficulty of differentiating the tracers crowded in the vicinity of the bottom. The film analyses showed that there always exists a thin bottom layer having onshore drift velocity, irrespective of breaker types. This layer is about 1 cm or less in depth for the cases of 1/15 slope, and may exceed 3 cm in 1/10 beach.

A wide mid-layer shows offshore mass transport (Fig. 2.8). Since continuity has to be satisfied, onshore mass transport must exist near the water surface to balance the net offshore flow in the water column, i.e., the mid-layer offshore discharge minus the bottom layer onshore discharge. Adequate measurement of the upper layer onshore mass movement velocity was not practical by the tracer method because a large quantity of air bubbles formed at the initial stage of wave breaking.

Run 1  
 T=1.00 sec  
 $H_b = 9.5$  cm  
 Spilling Breaker  
 unit: cm/sec



Run 3  
 T=1.34 sec  
 $H_b = 17.5$  cm  
 Transitional  
 unit: cm/sec

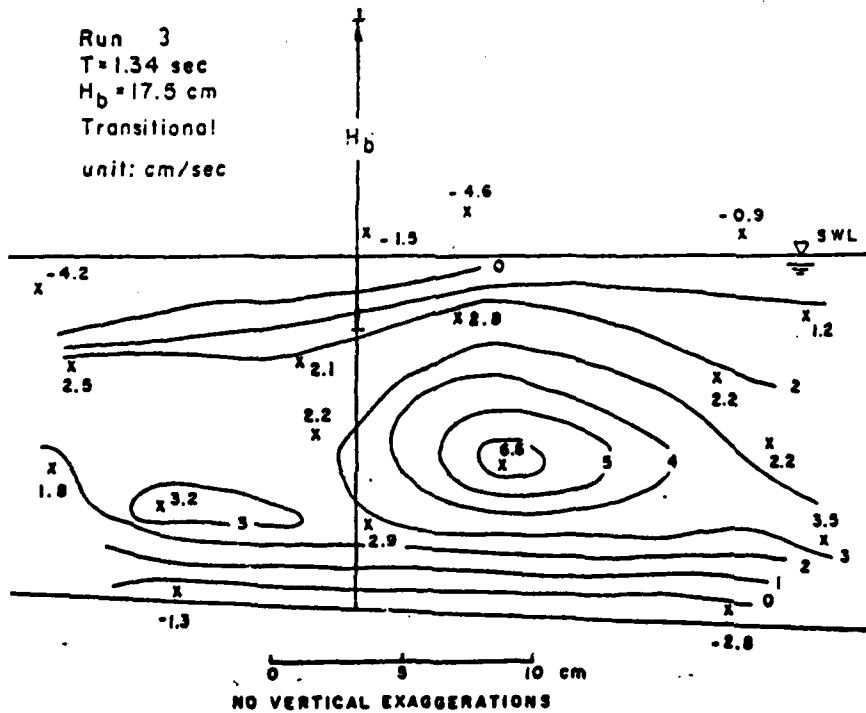


Fig. 2B. Example of isoclines of drift-velocity near the breaking point.

Fig. 2.9 shows some of the vertical distributions of drift velocity at the breaking point. The values were based on isolines intersecting with a vertical plane at the breaking point. Again, quantitative determination of the velocities on the bottom and at the surface could not be made.

### 2.2.3 Vertical Distributions

Vertical distribution of drift velocity at the breaking point is qualitatively similar to that in the offshore zone on a sloping beach (Bijker et al., 1974) and, to an extent, similar to that on a horizontal bottom (Russel and Osorio, 1957; Mei et al., 1972). Fig. 2.10 compares the shapes of the vertical distribution as obtained by experiments with the theories. The offshore drift velocity in the interior region, in general, shows a fairly uniform vertical distribution much more uniform than in the offshore region. These smoother profiles near the breaking point may be attributed to strong turbulent mixing. There seems to be little difference in the offshore drift velocity profiles between plunging and spilling breakers. The former might have a slight bulge in the lower or middle part of the profile, while the

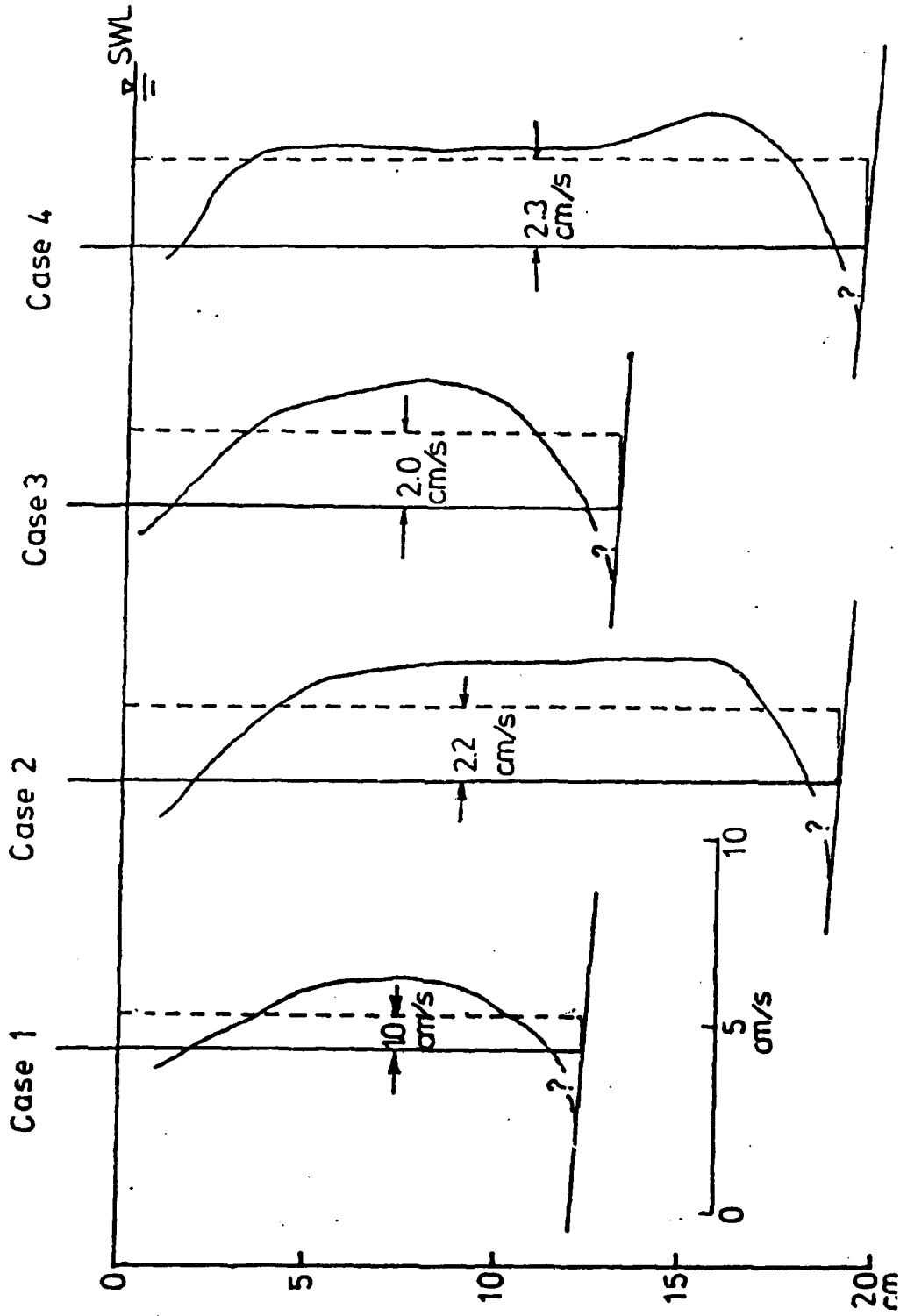
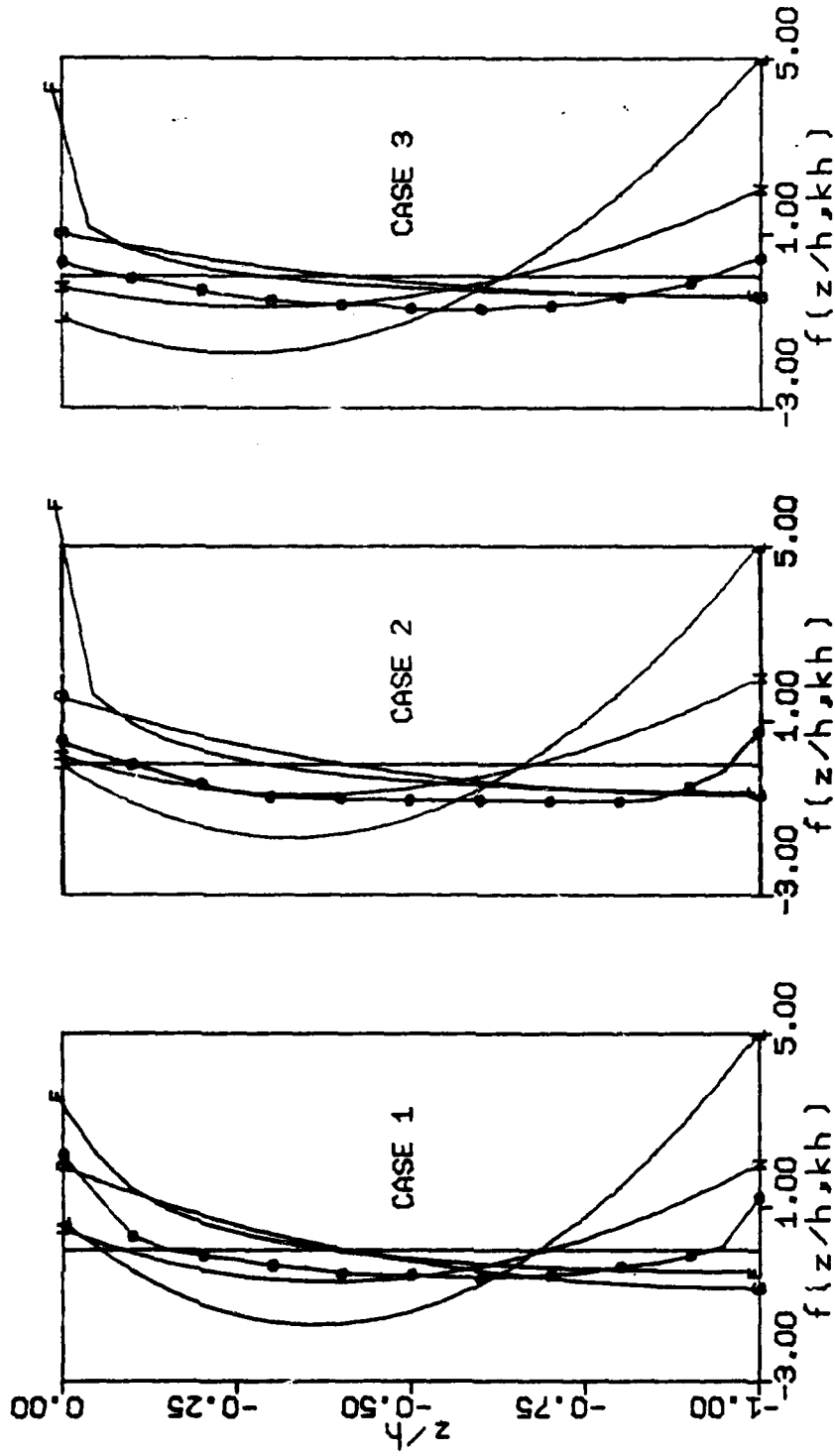


Fig.2.9. Vertical distribution of drift-velocity near the breaking point.



Legend: o-o-o Present Experiment, L--L Longuet-Higgins, S--S Stokes  
 W--W Wang & Liang, P--P Stream Function

Fig. 2.10 Comparison of shapes of drift velocity profiles.

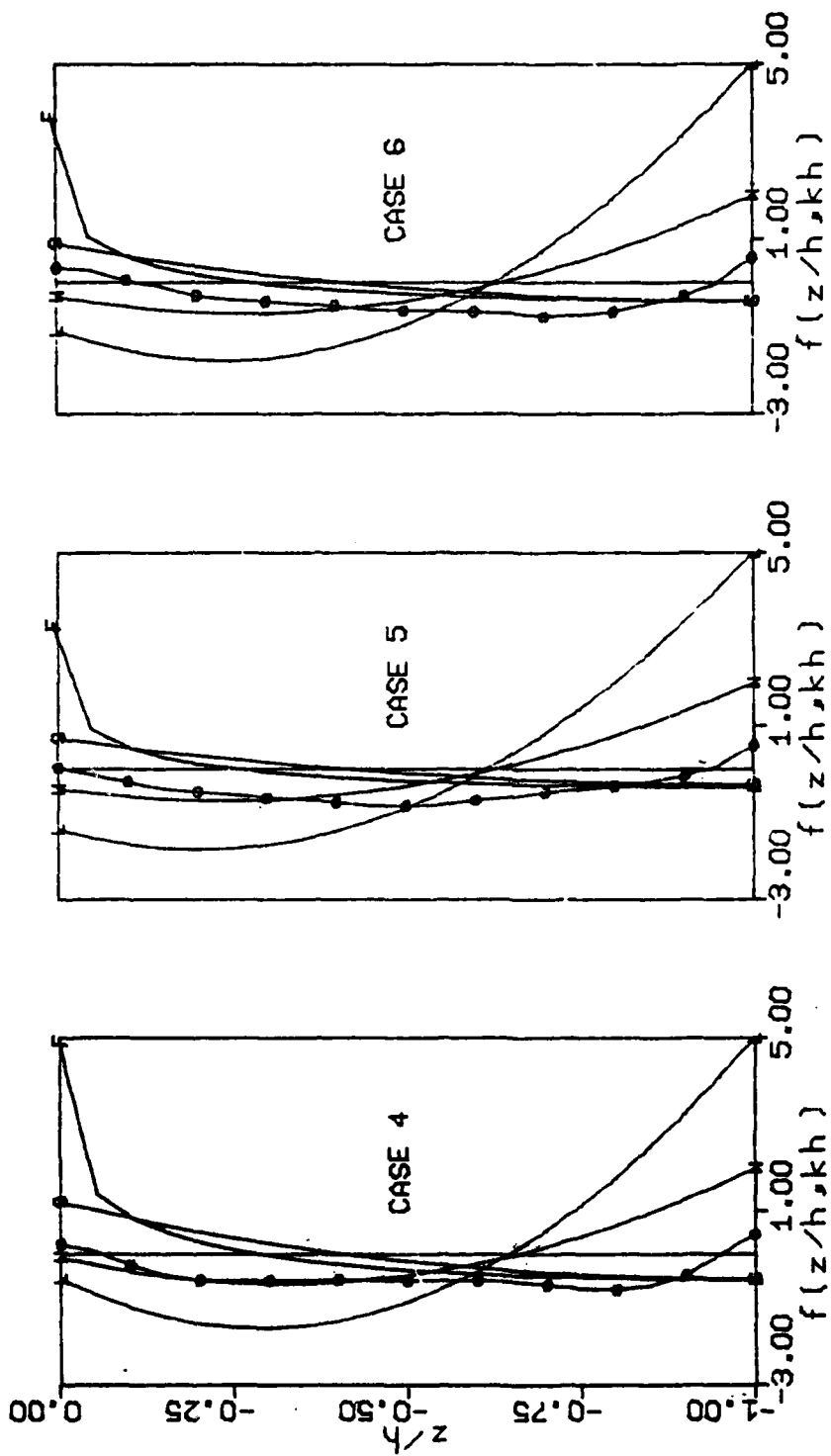


Fig. 2.10 (continued)

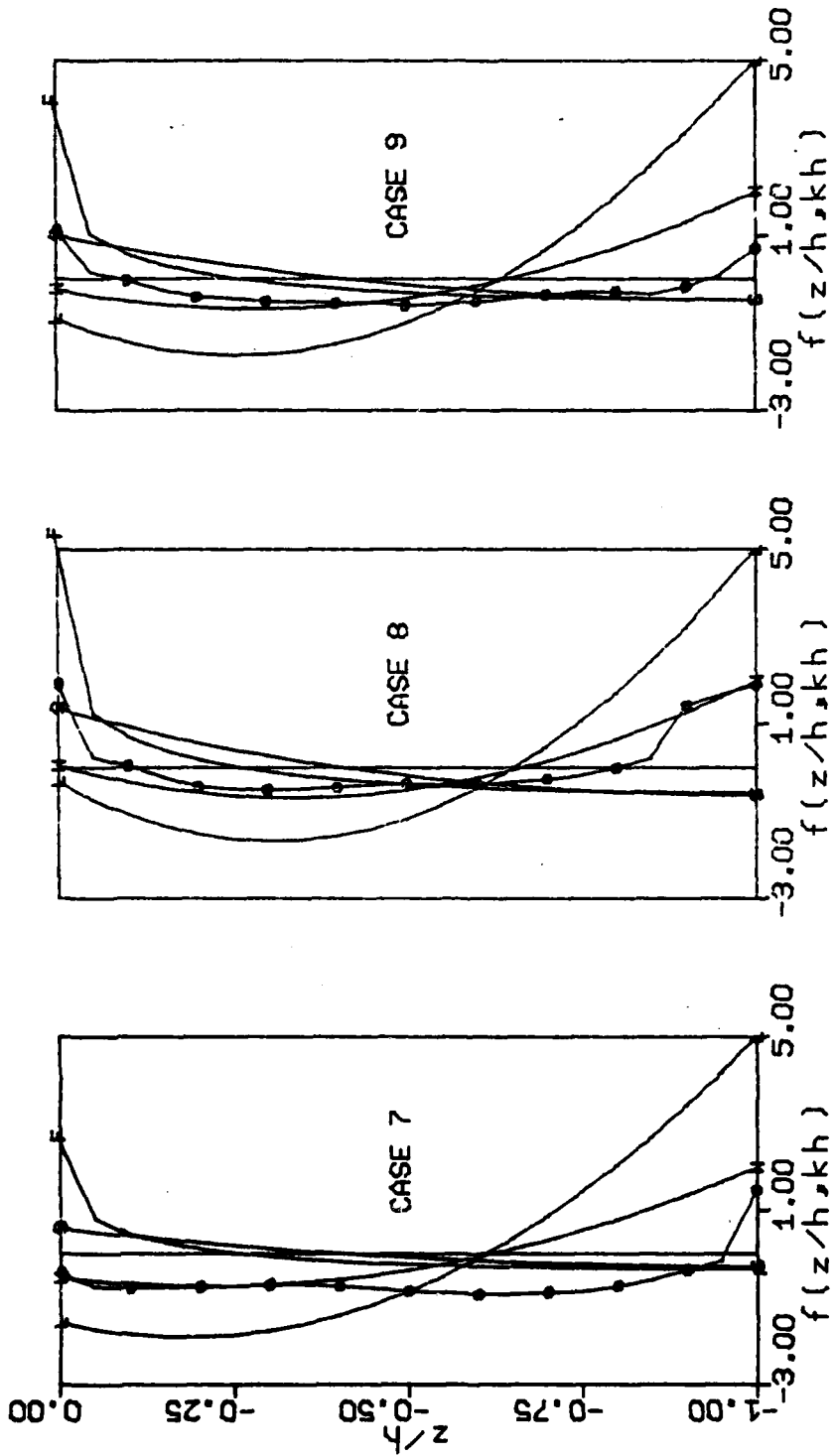


Fig. 2.10 (continued)

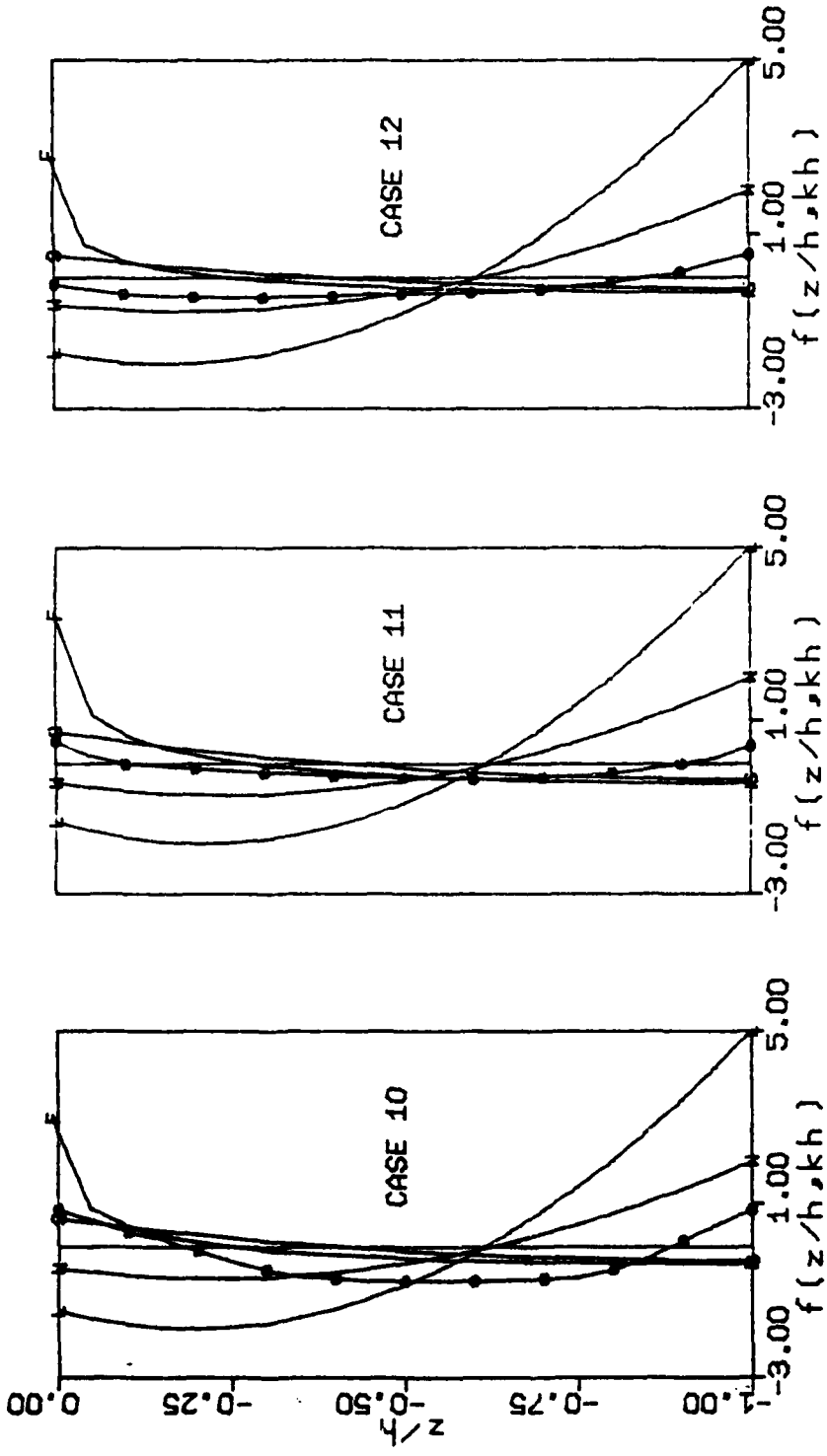


Fig. 2.10 (continued)

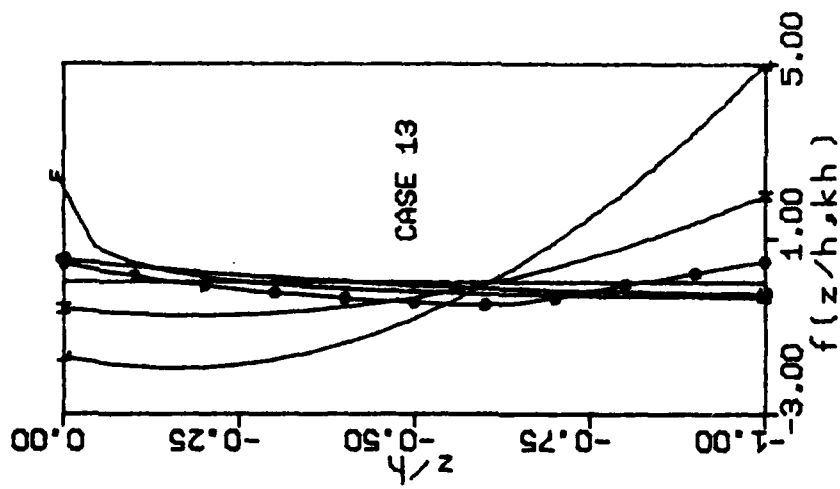


Fig. 2.10 (continued)

later has none.

### 2.3 Mean Offshore Drift Velocity

At present, there are a number of theories which can be used to estimate the mean drift velocity. All of these are, however, for water of constant depth. The results are summarized here with reference to the coordinate system shown in Fig. 2.11.

#### Longuet-Higgins' drift velocity

Longuet-Higgins' solution (1953) is for the interior region in a channel of constant depth with a laminar boundary layer:

$$U(z) = \frac{\rho^2 \sigma k}{4 \sinh^2 kh} f(kh, z/h) \quad (2-1)$$

where

$$f(kh, z/h) = \{2 \cosh 2kh(z/h+1) + 3 + kh[3(z/h)^2 + 4(z/h) + 1] \sinh 2kh + 3[2 \frac{\sinh 2kh}{2kh} + 3/2][(z/h)^2 - 1]\} \quad (2-2)$$

and  $U(z)$  is the drift velocity at depth  $z$ .

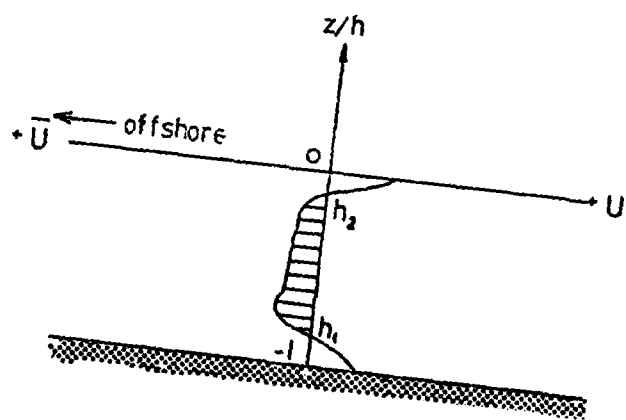
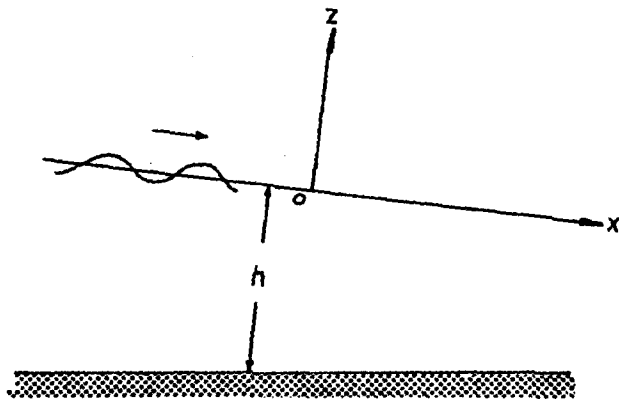


Fig.2.11. Coordinate system.

We define here the depth averaged offshore drift velocity as

$$\bar{U} = -1/h \int_{h_1'}^{h_2'} U(z) dz \quad (2-3)$$

where  $h_1'$  and  $h_2'$  are the upper and lower limits of the offshore flow, respectively. The non-dimensional drift velocity becomes

$$\bar{U}/a^2 \sigma k = F(kh)/4 \sinh^2 kh \quad (2-4)$$

where  $F(kh) = - \int_{h_1}^{h_2} f(kh, z/h) d(z/h)$ ,  $h_1$  and  $h_2$  are the dimensionless limits.

For large values of  $kh$  (deep water case),  $h_1 = -1$ ,  $h_2 = -1/3$ , and we have

$$\bar{U}/a^2 \sigma k = 2kh/27 = 0.074 kh \quad (2-5)$$

for shallow approximation, it becomes

$$U/\sqrt{gh} = 0.060 \kappa^2 \quad (2-6)$$

where  $\kappa = (H/h)_b$ .

Solution by Wang and Liang

Wang and Liang (1975) derived a mass transport solution similar to that of Longuet-Higgins except that an empirically determined turbulent boundary layer solution was used for the bottom matching condition. their solution takes the form:

$$U = \left\{ \frac{a^2 \sigma k}{4 \sin^2 kh} [2 \cosh(2kh(\frac{z}{h}+1))] + \frac{3 \sinh 2kh}{2kh} [(\frac{z}{h})^2 - 1] \right\} \\ + \frac{a^2 \sigma^2 k}{4\nu(E^2 + 0.09\beta^2)} \left\{ \left[ \frac{1.2\beta E}{E^2 + 0.09\beta^2} - 0.075 \frac{\beta}{E} \left[ \frac{3}{2} \left(\frac{z}{h}\right)^2 - \frac{1}{2} \right] \right\} \quad (2-7)$$

where  $E = 133 \sinh kh / a\beta D$ ,  $\beta = \sqrt{g/2\nu}$ ,  $\nu$  = kinematic viscosity of the fluid, and  $D$  is the bottom roughness.

For the case of a smooth bottom the shape function becomes

$$f(kh, z/h) = 2 \cosh 2kh (z/h+1) + \frac{3 \sinh 2kh}{2kh} [(z/h)^2 - 1] \quad (2-8)$$

For large values of  $kh$ ,  $U \rightarrow 0$ ;

for small values of  $kh$ , we have

$$\bar{U} / a^2 \sigma k = 0.096 / (kh) \quad (2-9)$$

Again, for shallow water approximation,

$$U/\sqrt{gh}=0.024 \kappa^2 \quad (2-10)$$

### Stokes drift velocity

The classic expression of mass transport velocity due to Stokes (1847) is

$$U = \frac{a^2 \sigma k \cosh 2kh \left(\frac{z}{h} + 1\right)}{2 \sinh^2 kh} + C_1 \quad (2-11)$$

with  $C_1$  is an arbitrary constant. For a system with zero total horizontal transport such as the present case, we must have

$$C_1 = - \frac{a^2 \sigma \sinh 2kh}{4h \sinh^2 kh} \quad (2-12)$$

consequently,

$$U = \frac{a^2 \sigma k}{4 \sinh^2 kh} \left\{ 2 \cosh 2kh \left(\frac{z}{h} + 1\right) - \frac{\sinh 2kh}{kh} \right\} \quad (2-13)$$

This solution is also for uniform water depth. The Stokes solution is for inviscid fluid and the velocity profile is basically different from that of the previous two cases as can be seen in Fig. 2.10. the mean offshore drift velocity is

$$\bar{U} = 1/h \int_0^{h_2} U dz = \int_0^{h_2} U d(z/h) \quad (2-14)$$

with the lower limit  $h_1$ , always equal to zero and the upper limit  $h_2$ , determined by letting  $U=0$  in Eq. (2.13), i.e.,

$$h = -1 + \frac{\cosh^{-1} \left( \frac{\sinh 2kh}{2kh} \right)}{2kh} \quad (2-15)$$

For the case of shallow water, both terms on the RHS of Eq. (2.13) become large quantities and the velocity distribution is subject to large variation for small numerical error. Substituting

$$\cosh 2kh(z/h+1) = 2 \sinh^2 kh(z/h+1) + 1$$

and using a small argument approximation, Eq. (2.13) can be reduced to

$$U = a^2 \sigma k (z/h+1)^2 \quad \text{for small } kh$$

To satisfy the zero net drift condition, the profile must be shifted such that

$$U = a^2 \sigma k [(z/h+1)^2 - 1/3] \quad (2-16)$$

The mean offshore drift velocity now becomes

$$\bar{U}/a^2 \sigma k = 0.179 \quad (2-17)$$

For shallow approximation,

$$\bar{U}/\sqrt{gh} = 0.0445 H^2 k^2 = 1.76 (h/L)^2 \kappa^2 \quad (2-18)$$

#### Numerical solution of stream function theory

Based on the stream function theory by Dean (1965), a wave stream function is defined as

$$\Psi(x, z) = Lz/T + \sum_{n=1}^{N_A} X(n) \sinh\left[\frac{2\pi n}{L}(h+z)\right] \cos\left(\frac{2\pi n}{L}x\right) \quad (2-19)$$

The elevation of a particular streamline,  $\Psi_*$ , can be written as

$$z_*(x) = T\Psi/L - T/L \sum_{n=1}^{N_A} X(n) \sinh\left[\frac{2\pi n}{L}(h+z_*)\right] \cos\left(\frac{2\pi n}{L}x\right) \quad (2-20)$$

The particle velocity along the streamline is then

$$u(x, z_*) = - \sum_{n=1}^{NL} X(n) \cosh\left[\frac{2\pi n}{L}(h+z_*)\right] \cos\left(\frac{2\pi n}{L}x\right) \quad (2-21)$$

Averaging  $u$  for one wave cycle using finite summation, the Lagrangian mass transport velocity is obtained

$$U(\bar{z}_*) = \frac{1}{\sum_{j=1}^{NL} \Delta t_j} \sum_{i=1}^{NL} u(x_i, z_{x_i}) \Delta t_i \quad (2-22)$$

where  $NL$  is the total segment number of one wave length,  $\Delta t_j = \Delta x_j / u_j$ , is the time fraction the particle travelled over  $\Delta x_j$  relative to wave motion, and  $\Delta x_i$  is the length of each small segment. Evaluating  $U(\bar{z}_*)$  for different  $\psi_*$ , the vertical drift velocity profile can be constructed.

Details of the Lagrangian mass transport by stream function theory are given in Appendix I. Applying this numerical scheme, the values of  $h_2$ , the upper intersect, and  $\bar{U}$  can also be determined. The results for the current experimental conditions are tabulated in Table 2.2.

Fig. 2.12 shows the dimensionless depth  $h_1$ ,  $h_2$  for the four theories discussed above. The data of the current experiment as well as those of Russel and Osorio, and Mei et al. are plotted on the same figure for

Table 2.2 Mean drift by stream function theory

case	$(H/h)_0$	$U/\sqrt{gh}$	$4\bar{U}/(\sqrt{gh}k^2H^2)$	$kh$	$U/a^2\sigma k$	$h_z$
1	.616	.0083	.080	.645	.117	-.380
2	.585	.0120	.135	.594	.213	-.280
3	.771	.0120	.222	.469	.249	-.274
4	.608	.0113	.160	.531	.238	-.288
5	.832	.0115	.286	.400	.289	-.278
6	.814	.0122	.248	.444	.260	-.274
7	.931	.0115	.355	.360	.312	-.278
8	.699	.0129	.171	.550	.218	-.270
9	.850	.0127	.231	.470	.246	-.274
10	.910	.0121	.340	.377	.308	-.277
11	.706	.0107	.248	.415	.302	-.288
12	.843	.0098	.343	.339	.336	-.277
13	1.014	.0118	.431	.331	.341	-.277

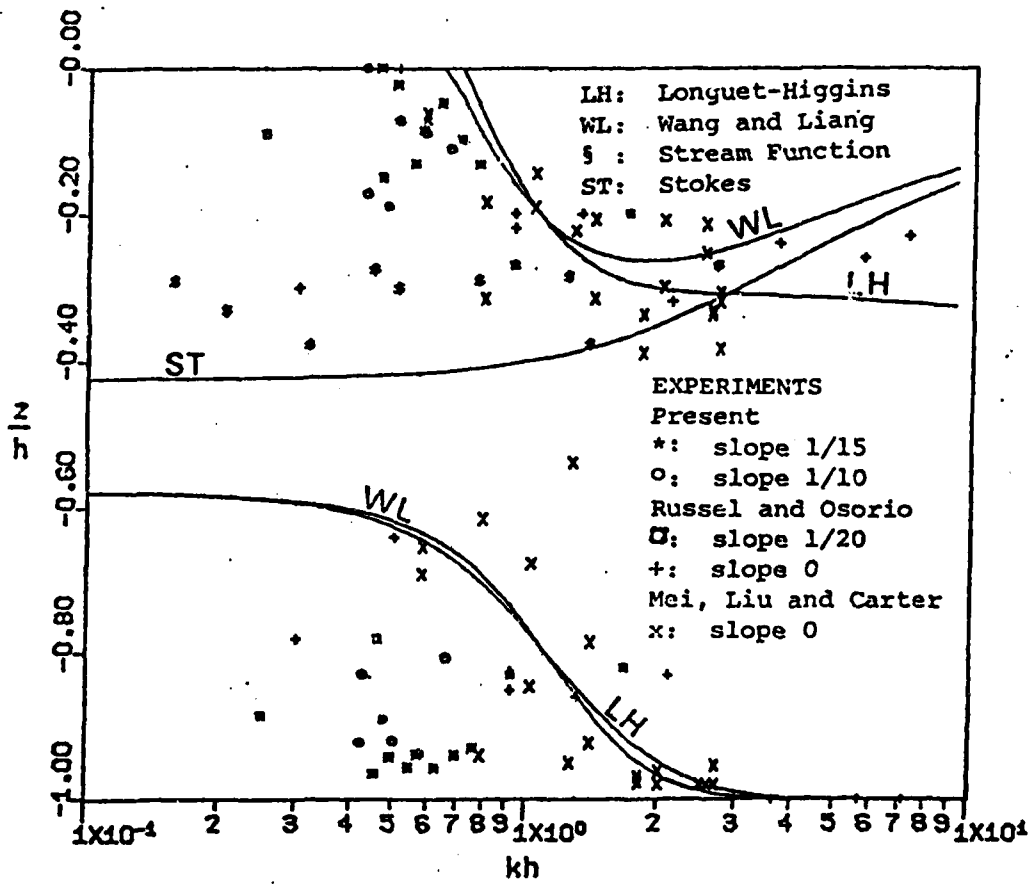


Fig.2.12. Limits of offshore drift depths,  $h_1$ ,  $h_2$ .

comparison. Data from sloping beach cases are found to have larger deviation from theories than those from constant depth. Also,  $h_2$  obtained by stream function theory is not just a function of  $kh$  as suggested by the other three theories. The depth averaged drift velocity derived above are summarized in Table 2.3.

#### 2.4 Results and Comparison

Since the drift velocity is a second order property, it was normalized by  $a^2\sigma k$ . In terms of shallow water parameters, the drift is found to be proportional to wave celerity and  $\kappa^2$ . We now proceed to compare these results with the experimental data. Fig. 2.13 plots the dimensionless offshore drift velocity,  $\bar{U}/a^2\sigma k$ , vs.  $kh$  on a semi-log scale. The four theoretical solutions are different in shape. Longuet-Higgins' solution (LH) first decreases with increasing  $kh$ , reaches a minimum around  $kh=1.1$ . For  $kh$  larger than 1.1, the drift velocity increases again, which is physically unlikely to happen. The Stokes solution (ST) is a monotonically decreasing function with increasing  $kh$  and the value almost maintains constancy for  $kh < 1$ . The solution by Wang and Liang (WL) is similar to Longuet-Higgins for  $kh < 1$ . For a

larger value of  $kh$ , the solution becomes closer to the Stokes' results. Stream function solution shows a similar trend as that of Wang and Liang's, but generally underestimates  $\bar{U}$  for  $kh < 0.5$ . However, it certainly is better than Stokes theory at shallow water. Most of the experimental data, as can be seen, fall in between the curves of LH and WL. The WL curve seems to agree better with the data, at least for  $kh > 0.5$ . The Stokes solution is apparently inadequate for shallow water. In this figure, the basic formulas are used, i.e., column 2 in Table 2.3. Figure 2.14 compares the experimental results with shallow water approximation, column 4 of Table 2.3. The dimensionless offshore drift velocity is plotted against  $k^2$ . It should be noted here that the parameter used in the ordinate is different for the Stokes solution as should be evident from Table 2.3. Both parameters are calculated for stream function theory and are given in Table 2.2. The non-dimensional parameter  $\bar{U}/\sqrt{gh}$  as computed seems to vary in a very narrow range around 0.012 which compares well with the data range. Least square fitting of the data yields a slope of 0.022, very close to WL curve, which could just be a coincidence. LH curve gives a much higher estimate compared to the data. Using the second parameter,  $\bar{U}/(a^2 k^2 \sqrt{gh})$ , results from

Table 2.3 Offshore mean drift velocity

Theory	Basic formula	Deep	Shallow
Longuet-Higgins	$\frac{\bar{U}}{a^2 \sigma k} = \frac{F(kh)}{4 \sinh^2 kh}$	$\frac{\bar{U}}{a^2 \sigma k} = 0.074 kh$	$\frac{\bar{U}}{\sqrt{gh}} = 0.060$
Wang and Liang	$\frac{\bar{U}}{a^2 \sigma k} = \frac{F'(kh)}{4 \sinh^2 kh}$	$\bar{U} \rightarrow 0$	$\frac{\bar{U}}{\sqrt{gh}} = 0.024$
Stokes	$\frac{\bar{U}}{a^2 \sigma k} = \frac{F''(kh)}{4 \sinh^2 kh}$	$\bar{U} \rightarrow 0$	$\frac{\bar{U}}{\sqrt{gh}} = 1.76 H^2 / L^2$

$$F(kh) = - \int_{h_1}^{h_2} \{ 2 \cosh 2kh (z/h + 1) + 3 + kh [ 3(z/h)^2 + 4(z/h) + 1 ]$$

$$\sinh 2kh + 3 [ \sinh 2kh / 2kh + 3/2 ] [ (z/h)^2 - 1 ] \} d(z/h)$$

$$F'(kh) = - \int_{h_1}^{h_2} \{ 2 \cosh 2kh (z/h + 1) + \frac{3 \sinh 2kh}{2kh} [ (z/h)^2 - 1 ] \} d(z/h)$$

$$F''(kh) = \int_{h_1}^{h_2} \{ 2 \cosh 2kh (z/h + 1) - \sinh 2kh / kh \} d(z/h)$$

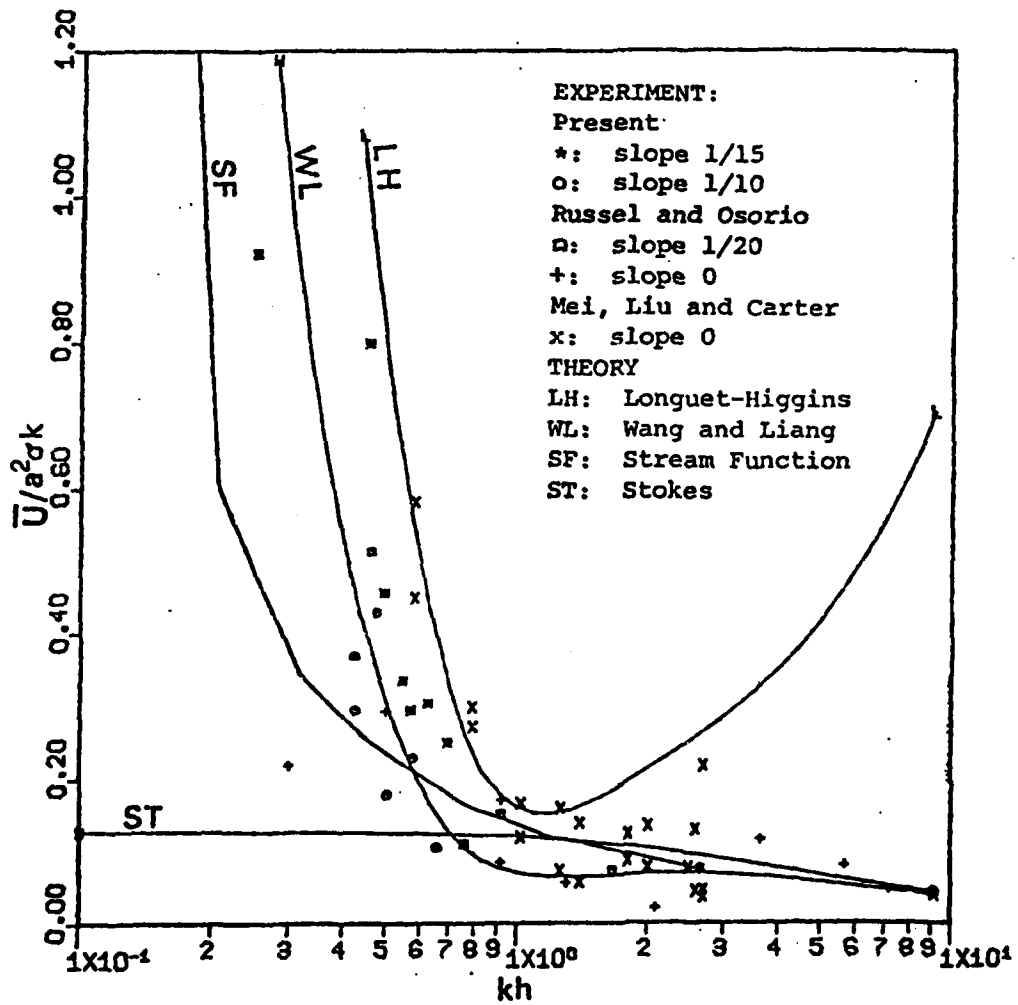


Fig.2.13. Results of mean offshore drift velocity vs.  $kh$ .

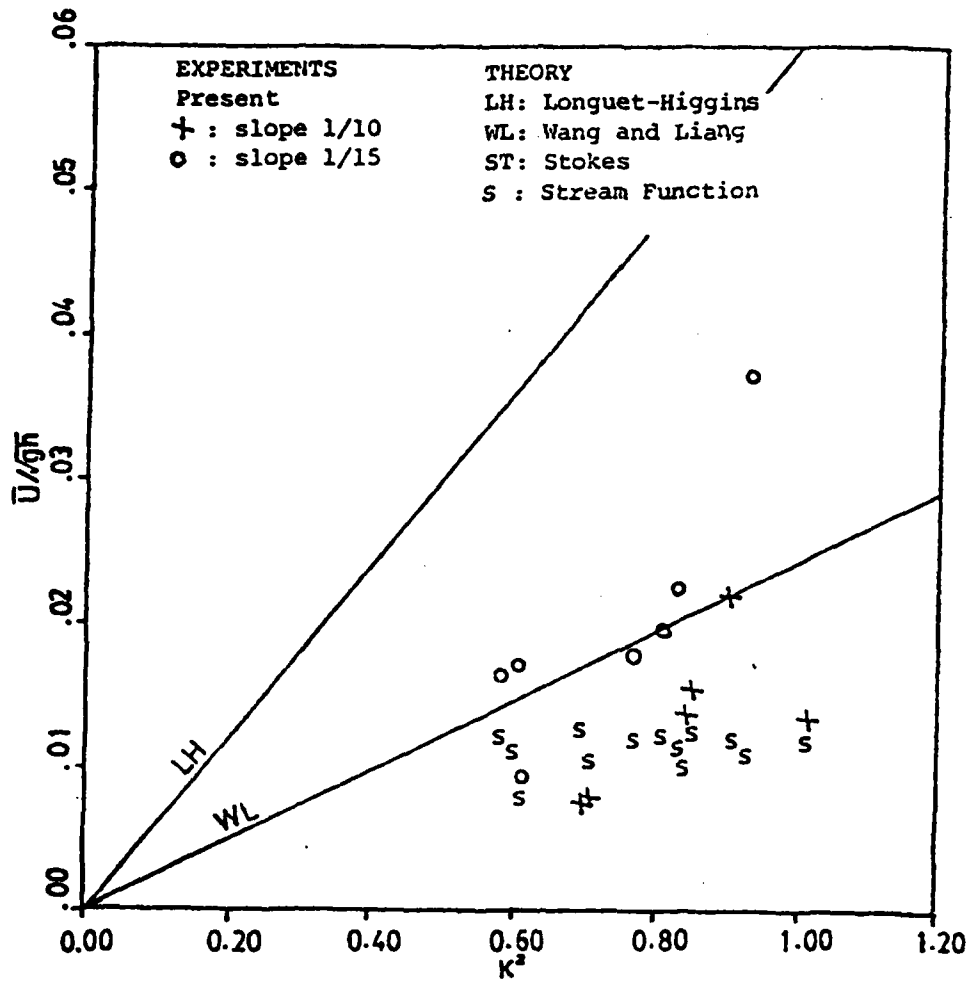


Fig.2.14a Results of mean offshore drift velocity vs.  $k^2$ .

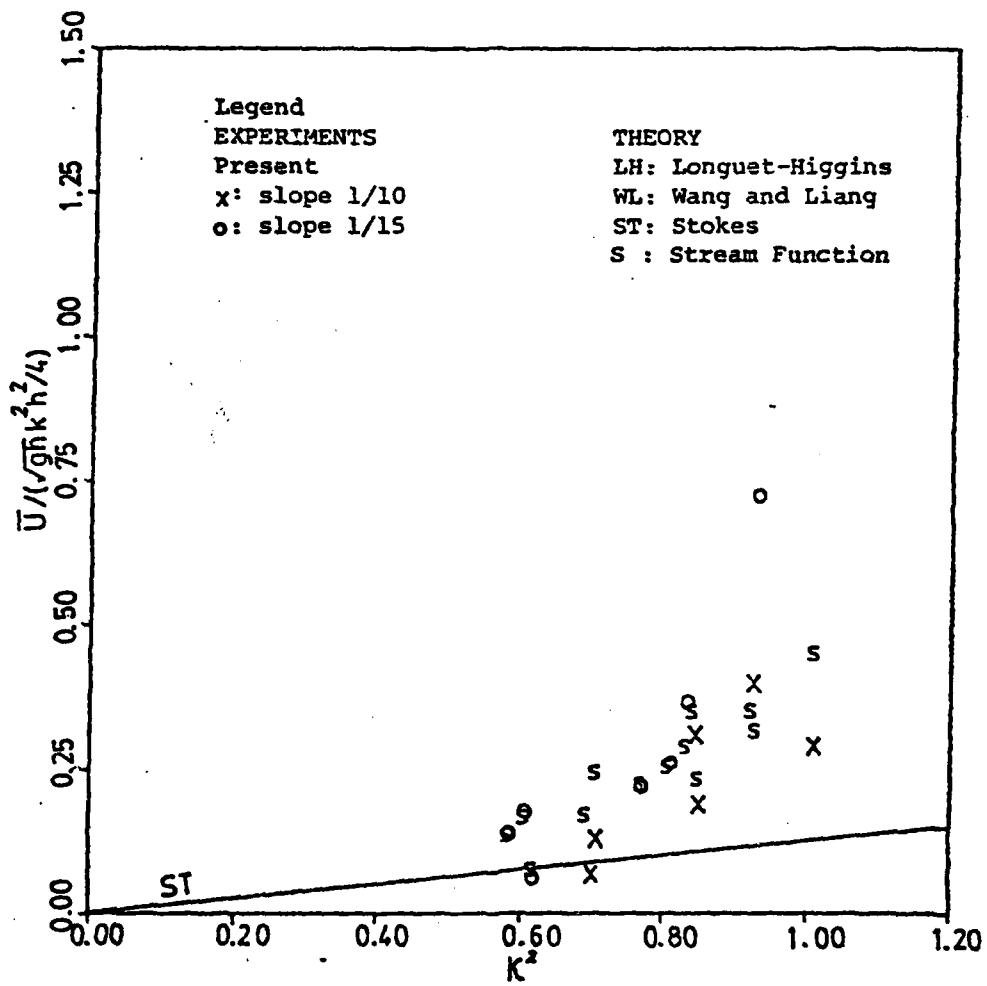


Fig.214b Results of mean offshore drift velocity vs.  $\kappa^2$ .

stream function show excellent agreement with the data. Since the data range is not truly in shallow water range, it is not understood why this latter expression is better for stream function results.

Comparing Figs. 2.13 and 2.14, one observes that the general formulas yielded better results than their shallow water approximation except for stream function. This is partially explainable as the range of  $kh$  tested all fall in the intermediate water depth range (on the lower end close to the shallow water case).

All the solutions presented here are for constant water depth. The effect of beach slope is not included. At present, there is no analytical solution for the sloping beach case to facilitate comparison. Based upon the three data sets, offshore drift velocity on the mild slope cases, in general, is higher than that of the steeper slope cases. Fig. 2.15 compares the cases when the drift velocity is plotted against  $kh$  to that when the drift velocity is plotted against a modified dimensionless parameter,  $kh^{1/2}$ . Because of the limited cases (only three different slopes), conclusions could not be made other than that the slope effect is probably not as important as the local water depth and input wave

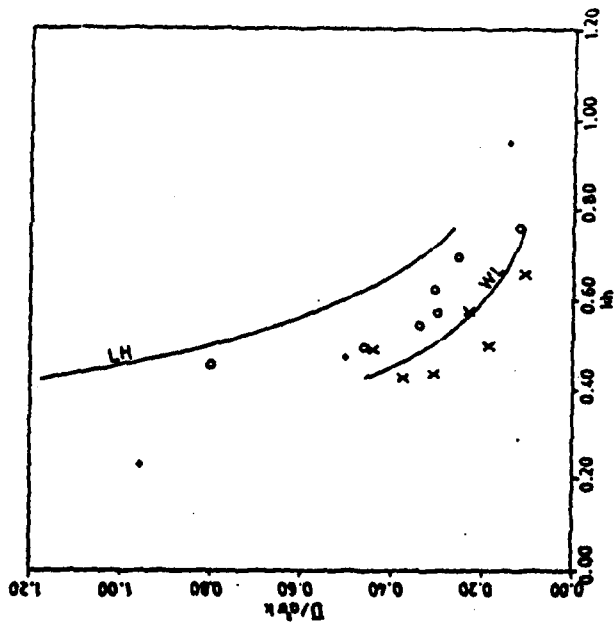
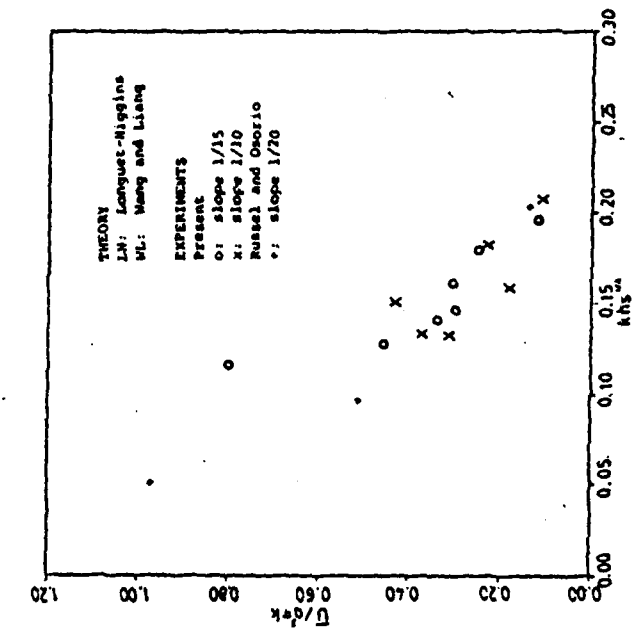


Fig. 15. Effects of bottom slope on mean offshore drift velocity.

conditions.

## 2.5 Conclusion

Laboratory experiments were conducted to determine the drift velocity at the breaking point on sloping beaches. It was found that, irrespective of breaker types, the drift velocity is in the onshore direction near the surface and close to the bottom. In the main flow column, the drift velocity is always offshore. The offshore drift velocity shows a more uniform vertical distribution than that in the offshore region probably due to the increased vertical momentum transfer by turbulence near the breaking point. This vertical distribution is very similar whether the breaker is plunging or spilling.

The predominant offshore drift velocity should play an important role in offshore sediment transport. Since the vertical distribution is rather uniform, the vertically averaged offshore drift velocity is a meaningful index. Four different constant depth wave theories were used to compute the mean vertically averaged offshore drift velocity. The solutions of Longuet-Higgins and Wang and Liang were found to compare

reasonably well with experiments in the range tested, with the latter being a better fit. The Stokes theory performs poorly. Results from stream function are significantly better than Stokes' but still underestimate the drift velocity in shallower water cases.

The test range was rather limited both in terms of wave parameter,  $kh$  and slope variations. Further laboratory studies should be continued to cover wider ranges.

Techniques for obtaining Lagrangian drift velocity needs improvement. The particle tracing method used may not produce enough data at the desired location and generally produced very scattered results especially near breaking.

Reflection from beach was not measured, since the drift velocity is proportional with amplitude squared, the effect may be small in comparison with the uncertainty in measurements.

## CHAPTER 3    SUSPENDED SEDIMENTS

### 3.1 Introduction

Measurement of suspended sediment in the surf zone has not been a favored topic among investigators. Documented field data are scarce. Yet, such information is imperative to a better understanding on the basic mechanics of littoral processes under breaking waves of which our present knowledge is rather rudimentary. For instance, practically all the existing longshore sediment transport formulas are based upon the wave energy flux approach with no real considerations of the fundamental mechanics. Such an approach leaves little room for future improvement. As far as onshore/offshore sediment transport is concerned, there exists no predictive formula even at the purely empirical level.

A number of factors can be cited that hinder the progress of the research toward this direction. First of all, surf zone measurement is a tedious and difficult task. Secondly, there is no proven instrument to measure

suspended sediment in the surf zone; all the existing techniques appear to be primitive. Thirdly, the most useful data are those collected under extreme weather with simultaneous measurement of all the pertinent environmental factors; hence, successful measurement is often a chance event. Fourthly, surf zone data often appear to be random with large variance which makes interpretation difficult and presentation unimpressive.

Perhaps the earliest serious attempt to measure suspended sediment distribution in water column in the surf zone was by Watts (1953). He designed a pump sampler that took time averaged samples by pumping sediment-laden water through intake nozzles situated at various elevations. The sampler was laboratory tested. He stipulated that if the nozzle opening is of the order of 1.27 cm and the pumping velocity is approximately twice the maximum water particle velocity, the sample collected should be within about 15 percent of the true suspension on a time averaged basis. The experiments were conducted from a pier located at Pacific Beach, Mission Bay, California. Wave data were partially visually observed and partially measured by a pressure gage. Using a similar device, Fairchild (1972) took in

excess of 800 suspended sediment samples along the City Pier, Ventnor, New Jersey, and Jennettes Pier, Nags Head, North Carolina. Most of the data were collected in the surf zone. Wave heights were reported but the method of measurement was not mentioned. Since both Watts and Fairchild's data were collected adjacent to piers, questions have been raised as to the effects due to the presence of the structures.

Fukushima and Mizoguchi (1958), Hom-ma and Horikawa (1965) and Tanaka (1975) tried suspended samplers made of bamboo poles to measure the vertical distribution of suspended sediment along the Japanese coast. Kana (1978, 1980), using a water sampler device similar to the bamboo sampler, manually collected over 1500 suspended sediment samples in the surf zone near Price Inlet, South Carolina and at an experimental pier site in North Carolina. His data should be considered quasi-instantaneous. The wave information was obtained by visual observations with the aid of a marked pole. Brenninkmeyer (1974) used an optical device termed almometer to measure the sediment concentration across the surf zone on the beach at Point Mugu, California. His data were instantaneous and continuous but their absolute

values were not reliable because of the uncertainty in calibration. Morris (1977) measured suspended sediments at Torrey Pines beach, California using a pump sampler along with an optical sensor. The data reported by these investigators were either in tabulated form or on log papers to fit a power or an exponential law of distribution.

More recently, Nielson and Green (1981) measured suspended sediment along the Australian coast using a sediment sampler operating on hydrostatic pressure difference instead of pumping. A more serious attempt was made by them to investigate into the mechanics of sediment suspension in light of these field data.

This chapter reports the results of field measurements conducted along the Island of Sylt, Germany. Based upon the results and those of others, a new approach is proposed here to explain the mechanics of sediment suspension and to develop predictive capabilities. To augment the field data, laboratory experiments were also conducted to further test the proposed method of computation.

### 3.2 Field Experiment

The field experiments described herein were part of a larger scale, multipurpose exercise. The site location and area hydrograph are shown in Fig. 3.1. The site is exposed to the North Sea and is characterised by the existence of an underwater transverse ridge running parallel to the shore approximately 500 m from the shoreline. The sea bottom for the general area is mainly sand with size distributions varying from fine to coarse. At the test site, the material is medium sand as will be shown later.

The beach slope varies from 1:100 under normal wave conditions to as steep as 1:50 during storm periods. The tide is mainly semidiurnal with a normal range of about 2 m. Consequently, the beach front is constantly assaulted by various wave conditions during one tidal cycle. In the vicinity and including the test area, the beach is highly erosional.

The first set of data were collected during and right after a storm on September 3-7, 1978. The sustained wind reached more than 25 m/sec during the height of the storm and the sea was fully risen. The second set of data were taken on September 26 and 27, 1979 when a moderate storm of lesser strength (sustained

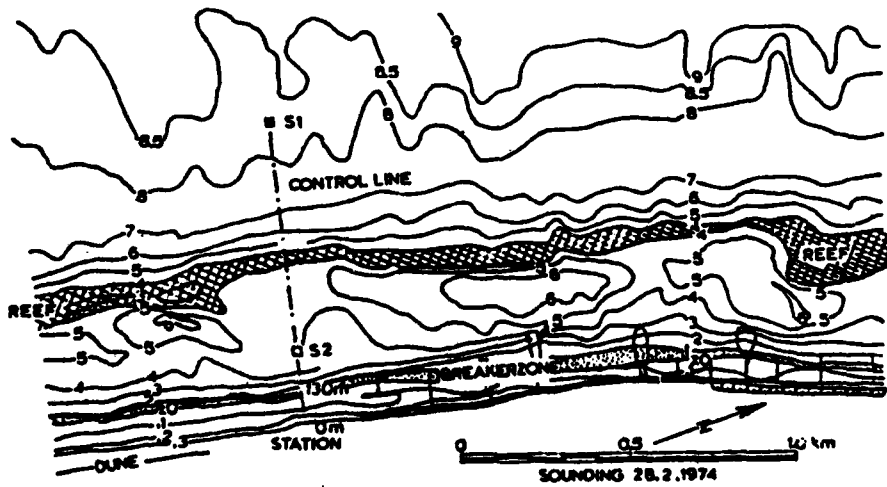
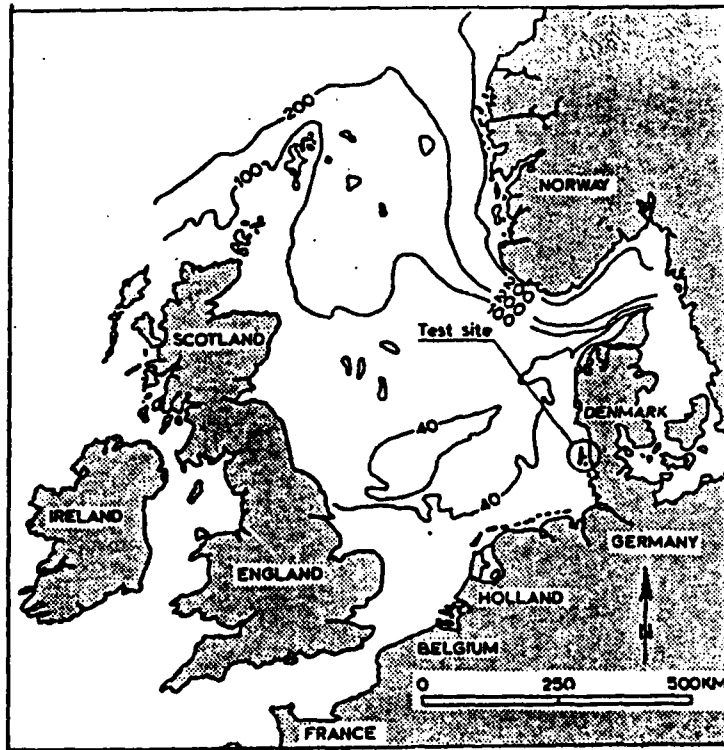


Fig.3.1 Site location and area hydrograph.

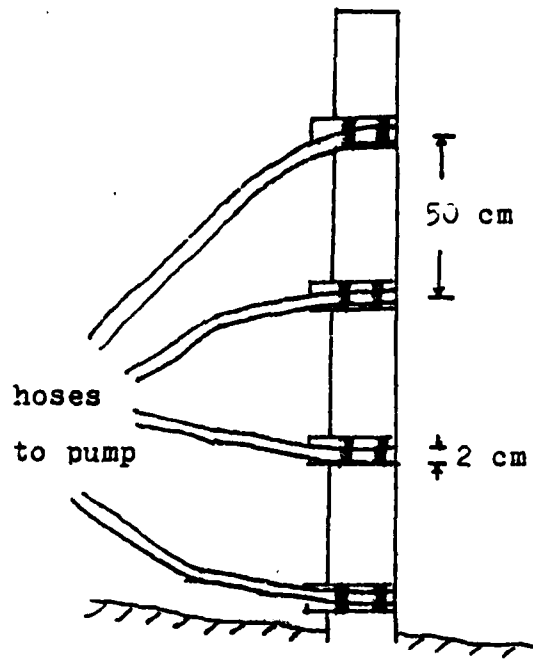


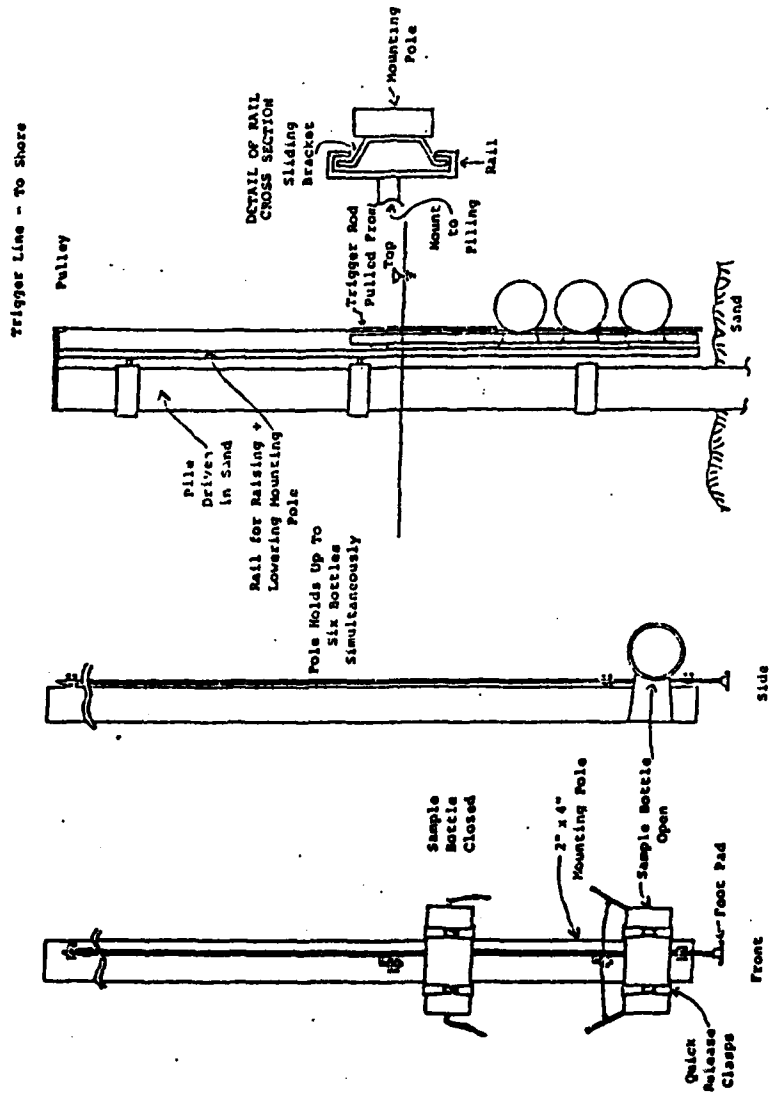
Fig. 3.2 Suspended sediment pump sampler

wind speed approximately 11.5 m/sec) hit the area.

In both experiments, continuous samples were taken by a pump sampler designed in accordance with the specifications recommended by Watts (1953). It has four intake nozzles, mounted on a vertical rack at intervals of 50 cm. The sampler was supported by a vertical staff set in the surf zone. To minimize the effect of the supporting structure, the sampler set was set apart from the supporting staff with a horizontal clearance of 1 m. The assembly is shown schematically in Fig. 3.2. The nozzle opening was 2 cm and the pumping rate was approximately 8.5 liters per minute. samples were collected at a constant volume of 36 liters per sample (4 to 5 minute sampling time) and were taken at one hour intervals for approximately half a tidal cycle (6 hours). During the second experiment, the bottom nozzle was often clogged with sand and these samples were discarded. In the second experiment, in addition to the continuous sampling, instantaneous samples were taken by a bottle sampling device modified from the one first used by Kana (1976). It consisted of a 2 m long mounting pole, support brackets and four 2 liter bottles closed off by hinged doors. The whole assembly was mounted on a pole

with sliding tracks (Fig. 3.3) and the doors could be triggered to close remotely to enable instantaneous sampling. Sample collectors were mounted at 30, 70, 110 and 150 cm above the bottom. The complete assembly was tested out satisfactorily on September 26, 1979, one day ahead of the scheduled actual experiment. Unfortunately, an overnight storm broke the mounting pole. The original plan had to be abandoned. Instead, the instantaneous sampling had to be carried out by manually carrying the sampler into the surf zone and triggering the device at the desired instance. Because of the high surf condition, this manual operation was difficult to carry out; the sampling location and timing could not be controlled as accurately as from a stationary station. Despite this setback, a total of sixteen runs were made at time synchronized with continuous samplings.

Surface waves and currents were measured at locations shown in Fig. 3.4. The deep water gages W1 and W2 were bottom mounted echo transreceivers. These echo sounders were capable of measuring water surface variations to  $\pm 0.5$  cm for water depths up to 90 m. The shallow water gages were staff mounted pressure transducers of type MDS76 as manufactured by H. Maihak



HAND HELD SEDIMENT SAMPLER  
SIDE VIEW SAMPLING STATION  
Figure 3.3 Suspended Sediment Sampler

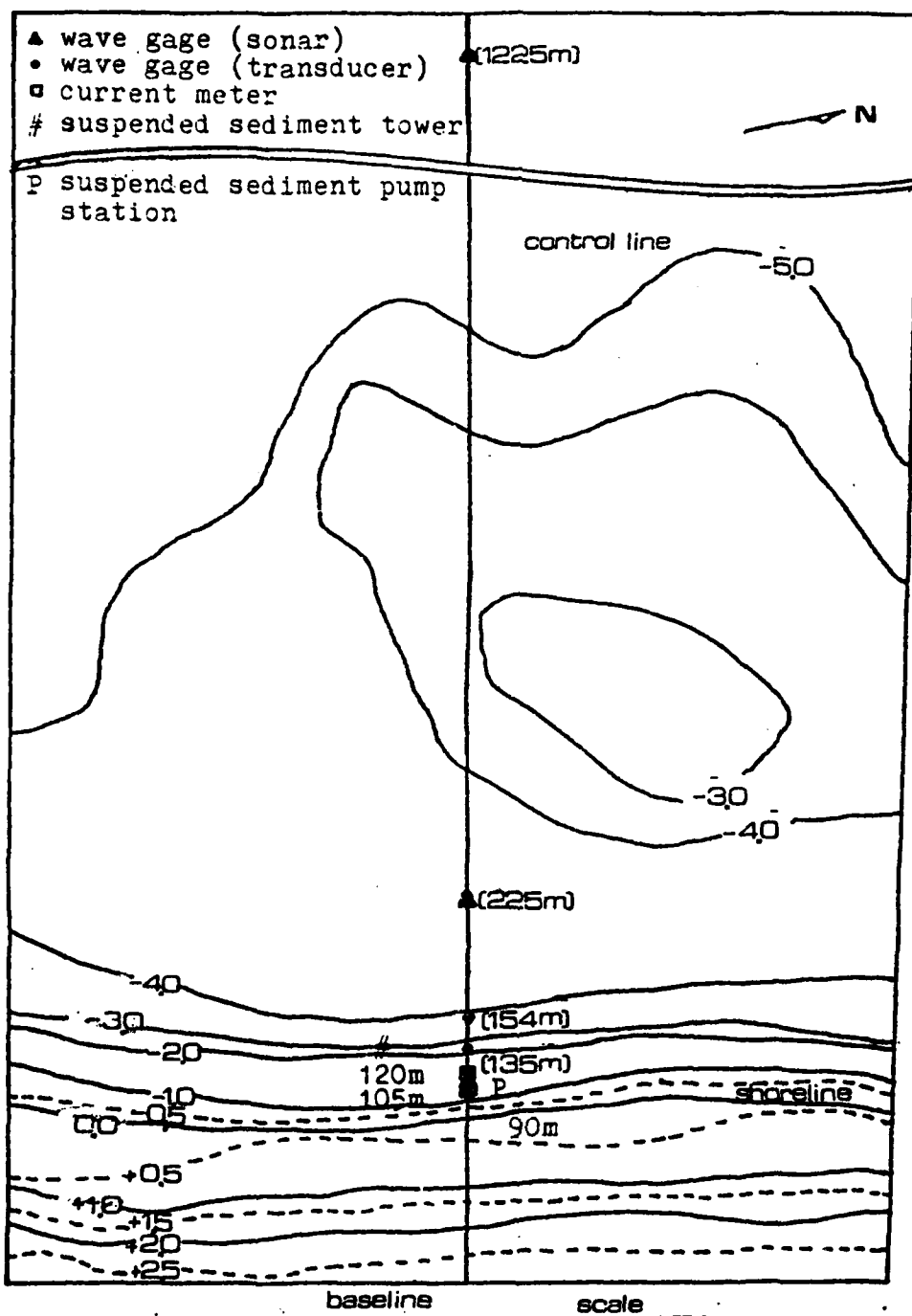


Fig. 3.4 Instrument arrangement at test site

AG, Hamburg with a pressure range of 0-1 kg/cm . The current meters were electromagnetic two-component type manufactured by COMEX. During the experiment, beach sand samples were also collected and beach profiles were surveyed at low tide.

suspended sediment data collected during the storm period on September 3, 1978 are presented in Table 3.1; the field conditions during the same period are summarized in Table 3.2. Fig. 3.5 displays the vertical concentration distribution for the September 3 data.

The beach profile surveyed at low tide together with the beach sand grain size distributions at various stations are shown in Fig. 3.6. As can be seen here, the beach material was medium to coarse sand and became coarser further offshore. At St. 50, the median grain size was about 0.38 mm which gradually increased to 0.65 mm at the offshore bar. An anomaly was observed in that the material was finer at St. 120 than at St. 110 which was shoreward of St. 120.

The suspended sediment data collected by continuous sampler during September 26 and 27, 1979 are given in Table 3.3. Table 3.4 summarizes the results of

Table 3.1 Suspended sediment pump data  
(September 3, 1978)

No.	C1* (mg/l)	C2* (mg/l)	C3* (mg/l)	C4* (mg/l)
1	68	102	163	9
2	109	185	168	186
3	---	157	255	346
4	209	194	291	543
5	254	173	269	386
6	174	141	165	160
7	152	187	190	223

\* Elevations of concentration measurements were:  
C1: 160 cm, C2: 110 cm, C3: 60 cm, C4: 10 cm  
from sea bed.

Table 3.2 Field condition (September 3, 1978)

No.	Tide (m)	h* (m)	H (m)
1	0.45	1.50	0.66
2	0.82	1.90	0.98
3	1.15	2.20	0.95
4	1.20	2.30	0.93
5	1.10	2.20	0.93
6	1.00	2.10	0.87
7	0.90	2.00	0.69

\* estimate at St. 110 based on measurement at low tide.

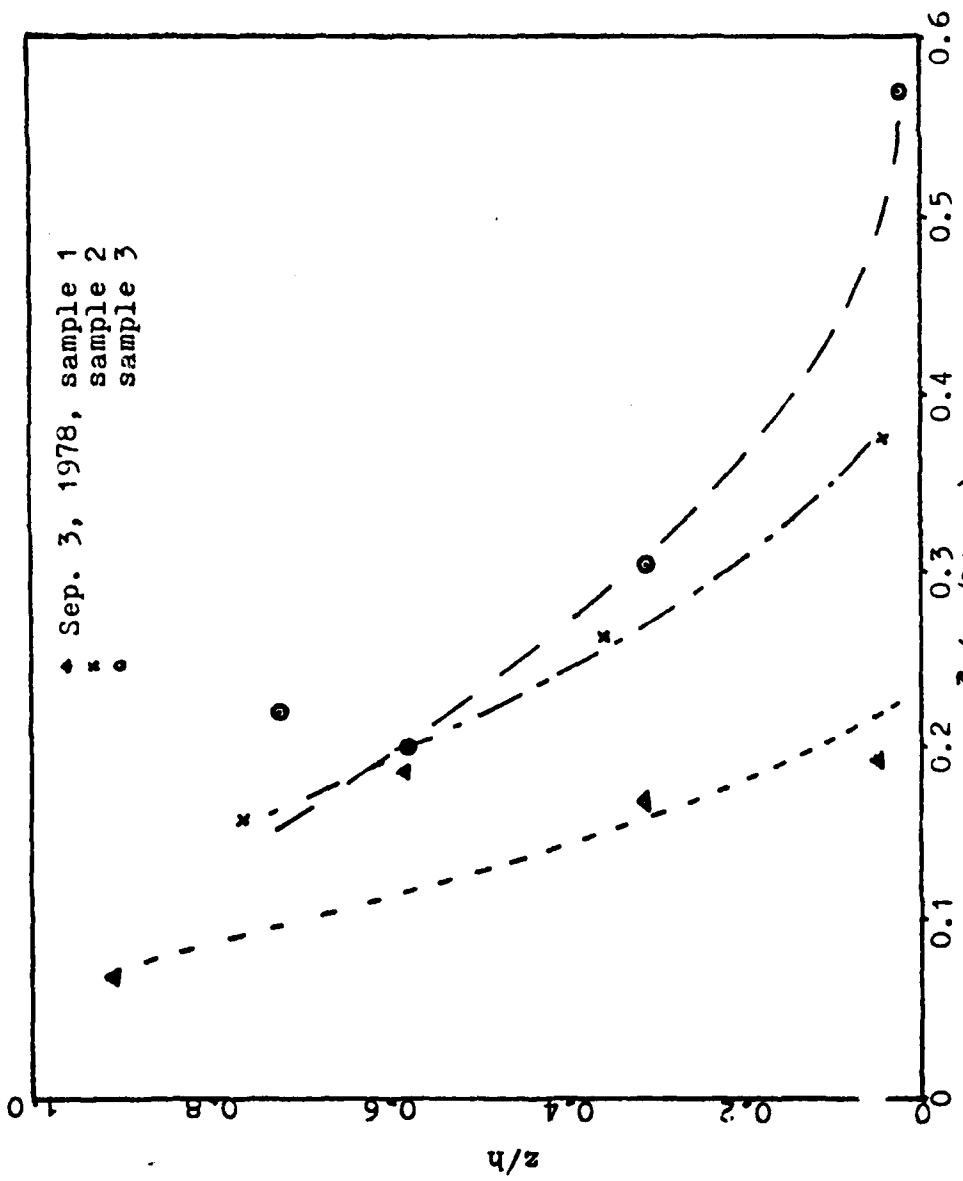
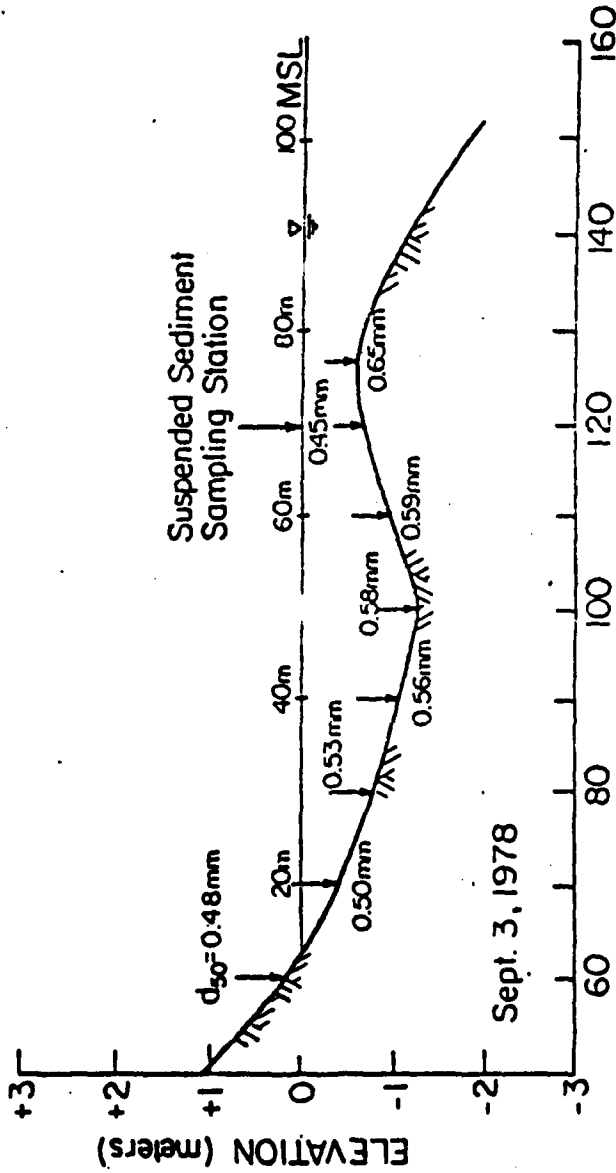


Fig. 3.5 Concentration profiles of September 3, 1978 experiment



STATION NO. (meters from Baseline)  
Fig. 3.6 Beach profile and sediment size distribution  
(September 3, 1978)

Table 3.3 Suspended sediment pump data  
(September 26-27, 1979)

CASE	C1*	C2*	C3*
	(mg/l)	(mg/l)	(mg/l)
N126	558	273	3940
N226	550	288	1029
N327	747	971	841
N427	697	826	500
N527	415	735	571
N627	553	644	332

\* Elevations of measurements:  
C1: 70 cm, C2: 120 cm, C3: 170 cm  
from sea bed.

Table 3.4 Suspend sediment bottle data  
(September 26-27, 1979)

CASE	LOCATION (M)	C1* (mg/l)	C2* (mg/l)	C3* (mg/l)
1	120	941	225	
2	120	479	270	280
3	105	240	74	96
4	120	530	200	
5	105	390	263	
6	105	117		
7	90	189	126	93
8	90	221	102	
9	90	293	70	
10	90	64		
11	90	766	134	149
12	90	641	86	33
13	90	127	348	
14	90	240		
15	90	449	73	65
16	90	561	161	

\* Elevations: C1: 30 cm, C2: 70 cm, C3: 120 cm  
from sea bed.

Table 3.5 Field conditions (September 26-27, 1979)

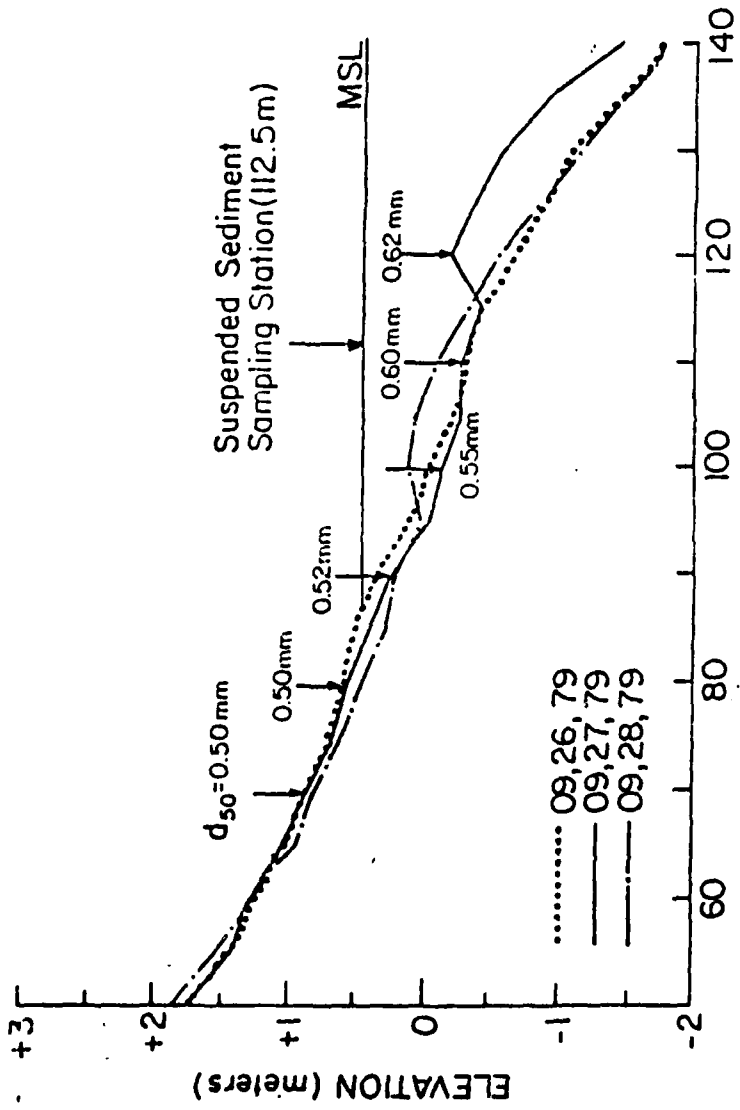
Case	Tide (m)	h (m)	H (m)	T (s)
N126	.90	.85	.85	6.0
N226	1.06	.85	.80	6.0
N327	.91	.80	.95	5.9
N427	.99	.80	.94	6.2
N527	.95	.80	.96	6.3
N627	.89	.80	.98	6.0
1	.46	.65		
2	.48	.65		
3	.77	.75		
4	.77	.65		
5	.80	.75		
6	.81	.75		
7	.93	.30		
8	.96	.30		
9	.97	.30		
10	.97	.30		
11	.96	.30		
12	.94	.30		
13	.91	.30		
14	.91	.30		
15	.89	.30		
16	.88	.30		

the instantaneous suspended sediment samples from September 27. The field conditions during the same period are given in Table 3.5. The beach profile at low tide together with the beach sand grain size distributions are shown in Fig. 3.7.

Grain size distributions were obtained by sieve analysis and by fall velocity analysis. The results from both methods are comparable. The fall velocity analysis used for this task is connected to a mini-computer which performs structured statistical analysis and plots size distribution. Detailed data tabulation and presentation can be found in Wang et al. (1980). Those data revealed several aspects:

A. On the average, the grain size of the suspended sediment is much smaller than the bottom sand. For example, the data of September 3, 1978 shows that the mean median grain size for all the suspended samples is 0.2 mm as compared to that of 0.45 mm for the bottom material. For the September 27, 1979 data, the corresponding values are 0.2 mm and 0.6 mm, respectively.

B. The suspended sediment grain size distribution is much



STATION NO. (meters from Baseline)

Fig.3.7 Beach profiles and sediment size distribution (September 26-28, 1979)

Small vertical text on the right margin, possibly a page number or reference code.

more uniform than the available bottom sand as can be seen from the values of their standard deviation.

C. In the water column, the sand sizes decrease with the elevation.

### 3.3 Laboratory Experiment

The experiment was conducted in the same steel wave flume described in Chapter 2. Sand beach was placed at the glass section. The mean diameter of the sands was 0.31 mm with fall velocity variance of 0.36. The quantity of sand was large enough, no overtopping or exposure of the tank bottom ever occurred. Two capacitance type wave probes were used for wave measurements. One located at the breaking point and the other at a constant depth section 5 m from the generator. The constant depth probe was installed on a moving cart to facilitate reflection measurements. The response time for the probes was about 0.03 seconds.

Horizontal and vertical particle velocities at the breaking were measured using a Marsh-McBirney electromagnetic current meter, model 523M with 0.1 second time constant. The sensing volume was a sphere of 1.5"

diameter (three times of the sensor diameter); data so collected were thus an average over this distance. The sediment concentration was measured by an Iowa Sediment Concentration Measurement System (ISCMS) designed at the University of Iowa. the major problem of this instrument is the intermittent signal output as widely discussed in the literature (Nakato et al., 1977; Glover, 1977; Locher et al., 1976). The sensing volume is about 1 mm sphere and the frequency response is 1 KHz.

The data were fed into an on-line Digital MINC11 minicomputer through A/D converter. The sampling rate and the sample size were fixed at 64 Hz and 64 seconds, respectively. Wave record at constant depth was registered by a HP 7402A chart recorder. A Tektronix Oscilloscope with model 3A74 4-trace amplifier was used for monitoring the A/D data collection.

At the beginning of the experiment, a constant slope sand beach was constructed and this beach was then subject to wave action for 10 to 12 hours until a quasi-equilibrium condition was reached. At the breaking point, simultaneous data of surface elevation, horizontal and vertical velocities and concentrations were then taken. The measurements of the last three quantities

started from the lowest elevation which was just above the ripple crest, then progressing upward at 0.5 cm interval for the first 3 levels, and 1 to 2 cm intervals afterward depending on the local water depth. A total of 5 to 9 elevations for each case were taken. Table 3.6 summarizes the test conditions of the experiments.

#### 3.4 On the Theory of Vertical Concentration Distribution

Of great interest to sediment transport is the vertical distribution of suspended sediment in the water column. The problem of sediment suspension in oscillatory flow is an unsettled issue. A general examination on the mechanics of sediment suspension in a wave field is given first before the analysis of the actual field and experimental data.

At present, sediment suspension in a fluid media is treated as a diffusion-dispersion process, and the governing equation takes the following form:

$$\partial C / \partial t + \nabla \cdot (C \vec{v}_s) = \nabla \cdot (\nu \nabla C) \quad (3-1)$$

where  $C$  is the volumetric or weighted sediment concentration;  $\vec{v}_s$  is the particle velocity vector,  $\nu$  is

Table 3.6 Wave conditions of sediment experiment

CASE	T (s)	H <sub>c</sub> (cm)	h <sub>c</sub> (cm)	H <sub>b</sub> (cm)	h <sub>b</sub> (cm)	kh	R+10 <sup>4</sup> ξ (%)	Ur	η <sub>r</sub> (cm)	λ <sub>r</sub> (cm)
A-04	2.05	6.0	35.0	12.5	12.5	.37	6 121	1.53	2.0	15.0
A-05	2.69	8.3	34.5	13.7	17.0	.31	21 93	1.91	4.0	15.0
A-06	2.10	7.7	36.8	12.0	15.8	.38	10 114	1.28	1.0	10.0
B-06	1.79	5.2	36.8	10.8	13.8	.43	26 136	1.08	2.0	10.0
A-07	1.59	6.3	36.8	11.0	13.8	.49	10 161	0.88	2.0	8.0
B-07	1.43	6.3	36.8	10.0	15.0	.57	12 157	0.52	2.0	8.5
A-08	1.23	8.4	36.8	10.0	17.0	.73	5 203	0.33	1.5	7.0
B-08	1.08	11.1	36.8	11.0	21.5	.99	? 247	0.16	1.0	6.0
C-08	1.08	11.1	36.8	10.2	9.0	.59	? 344	1.06	7.0	50.0
A-09	2.21	5.1	35.7	10.0	16.5	.38	9 88	1.02	1.0	10.0
A-10	3.74	9.0	34.0	17.0	19.0	.24	20 66	3.13	1.0	10.0
B-10	3.07	10.9	34.5	16.5	18.5	.29	6 78	2.11	1.0	10.0
A-11	3.44	6.5	34.0	14.0	18.0	.25	? 66	2.64	2.0	15.0

(Table 3.6 continued, elevations)

case	z1	z2	z3	z4	z5	z6	z7	z8	z9
A-04	-.97	-.94	-.87	-.86	-.81	-.41			
A-05	-.96	-.93	-.94	-.92	-.80	-.62	-.35		
A-06	-.95	-.92	-.85	-.79	-.69	-.29			
B-06	-.96	-.93	-.89	-.78	-.67	-.33			
A-07	-.96	-.93	-.91	-.82	-.71	-.29			
B-07	-.97	-.93	-.93	-.83	-.73	-.60	-.47	-.33	
A-08	-.91	-.94	-.88	-.82	-.74	-.62	-.50	-.25	-.37
B-08	-.95	-.93	-.88	-.79	-.65	-.47	-.23		
C-08	-.94	-.89	-.83	-.72	-.67				
A-09	-.97	-.94	-.88	-.76	-.64	-.49			
A-10	-.97	-.95	-.89	-.79	-.69	-.53	-.38	-.27	
B-10	-.95	-.95	-.89	-.84	-.82	-.65	-.49	-.32	
A-11	-.99	-.95	-.92	-.81	-.64	-.42			

+ reflection coefficient from constant depth measurement

? not measured

the molecular diffusion coefficient. For an oscillatory flow field, the concentration and velocity can both be divided into three components:

$$C = \bar{C} + C_w + C' \quad (3-2)$$

and

$$\vec{v}_z = \bar{\vec{v}} + \vec{v}_w + \vec{v}' \quad (3-3)$$

Here  $\bar{C}$  and  $\bar{\vec{v}}$  are the mean values,  $C_w$  and  $\vec{v}_w$  are the oscillatory components, and  $C'$ ,  $\vec{v}'$  are the turbulent fluctuations. Substituting Eqs. (3.2) and (3.3) into Eq. (3.1), and taking time average yields

$$\nabla \cdot (\overline{C\vec{v}} + \overline{C_w \vec{v}_w} + \overline{C' \vec{v}'} ) = \nabla \cdot (\nu \nabla C) \quad (3-4)$$

If the molecular diffusion is small and the gradients in the horizontal plane are much smaller than those in the vertical direction, Eq. (3-4) becomes

$$\frac{d}{dz} (\overline{Cv} + \overline{C_w v_w} + \overline{C' v'}) = 0 \quad (3-5)$$

here  $z$  is the vertical axis, with positive pointing upward,  $\bar{v}$ ,  $v_w$  and  $v'$  are the vertical components of  $\vec{v}$ ,  $\vec{v}_w$  and  $\vec{v}'$ , respectively. Since there is no net flux across the free surface, Eq. (3-5) when integrated once becomes

$$\overline{Cv} + \overline{C_w v_w} + \overline{C'v'} = 0 \quad (3-6)$$

Here the mean velocity,  $\bar{v}$ , is usually negative and is the mean settling velocity of sediment in calm water. In the usual context of turbulent diffusion processes, the last term in Eq. (3-6) is assumed to be

$$\overline{C'v'} = -\varepsilon \frac{d\bar{C}}{dz} \quad (3-7)$$

where  $\varepsilon$  is the turbulent diffusion coefficient. Eq. (3-7) now becomes

$$\overline{Cv} + \overline{C_w v_w} - \varepsilon \frac{d\bar{C}}{dz} = 0 \quad (3-8)$$

If we let  $w_0$  be the magnitude of particle fall velocity in calm water, Eq. (3-8) becomes

$$-Cw_0 + \overline{C_w v_w} - \varepsilon \frac{d\bar{C}}{dz} = 0 \quad (3-9)$$

The first and last terms in Eq. (3-9) constitute the conventional one-dimensional turbulent diffusion equation; the middle term represents the concentration being convected by the oscillatory velocity component in the vertical direction. If the terms of  $\overline{C_w v_w}$  and  $\epsilon$  are known or given, Eq. (3-9) can then be used to solve the vertical sediment distribution. Unfortunately, none of these terms are known in oscillatory flow field; various assumptions have to be made to arrive at distribution laws that are to be verified by experiments. A number of cases that have been proposed by various investigators are examined here.

Up-to-date research efforts have been mainly on determining  $\epsilon$  in wave field neglecting the contribution due to  $\overline{C_w v_w}$  (at least not explicitly treated as a special term). Then, depending upon the assumptions made on  $\epsilon$ , various distribution functions can be obtained. Most investigators, for instance, treated both  $w_0$  and  $\epsilon$  as constants which results in an exponential distribution. Laboratory experiments, notably Bhattacharya (1971), seemed to suggest a power law distribution which implies that  $\epsilon$  varies linearly with the vertical coordinate  $z$ . Hom-ma and Horikawa (1963), following von Karman's mixing

length hypothesis, derived an expression for  $\bar{C}$  to vary as  $\sinh^3 kz / \sinh^3 kh$  which is approximately  $z^3$  in shallow water; the resulting distribution then becomes a log-exponential curve of the form  $\ln \bar{C} = \bar{C}_0 z^k$ . Other suggestions were also made by different investigators (Dally, 1980; Yang, 1981; Nielson, 1981, for instance) to arrive at different distributions. Table 3.7 gives a summary of various formulas on sediment vertical distributions as being proposed.

All the formulas given in Table 3.7 will yield distribution functions that are monotonically decreasing with elevation, i.e., sediment concentration decreases monotonically from the bottom to the surface. A number of experimental results, including some cases reported here, revealed such not to be the case. The concentration can actually be higher at surface layer than mid-depth. There are three possible causes for such anomaly:

1. Oscillatory velocity field resulting in a reduced effective fall velocity for sediment particles (Fig. 3.8a),

Table 3.7 Summary of  $\epsilon$  and C profiles

$\epsilon$	$C^*(z) = C(z)/C_0$	Sources
constant	$\exp[w(z-z_0)/\epsilon]$	
$Kz$ (+)	$(z/z_0)^{**}(-w/K)$	
$Ku^*$	$\exp[(-Kw \exp[(z-z_0)/u^*h])]$	Dally, 1980
$Kv_w 1$	$[\tanh \frac{kz}{2} / \tanh \frac{kz_0}{2}]$	Wang and Liang, 1975
$K \int \frac{\partial^2 u}{\partial z^2}$	$\exp[-\frac{z}{f} (\frac{w}{C}) (\frac{1}{H})^2 (\frac{h}{z}) f(z) \sinh^2 kh]$	Hom-ma and
	$f(z) = \frac{1}{2zh} \left\{ \left( \frac{\cosh kh(z-z_0)}{\cosh^2 k(z-z_0)} - \frac{\cosh kz}{\sinh^2 kz} \right) + \ln \left[ \tanh \frac{k(z-z_0)}{2} / \tanh \frac{kz}{2} \right] \right\}$	Horikawa, 1962
$\epsilon_b + \epsilon_3(z/h)^2$	$\exp \left[ \frac{-w h}{\sqrt{\epsilon_b \epsilon_3}} \tan^{-1} \frac{z}{z_b} \frac{z}{h} \right]$	Nielsen and Green, 1981
$Ku L$	$\exp \left[ \frac{2w \sinh kh}{3a \sigma} (\tan^{-1} e^{kz} - \tan^{-1} e^{kz_0}) \right]$	Wang, 1981

+ K: a constant

u, v : horizontal and vertical particle velocities, respectively

$u^*$ : frictional velocity ( $=\sqrt{\tau/\rho}$ )

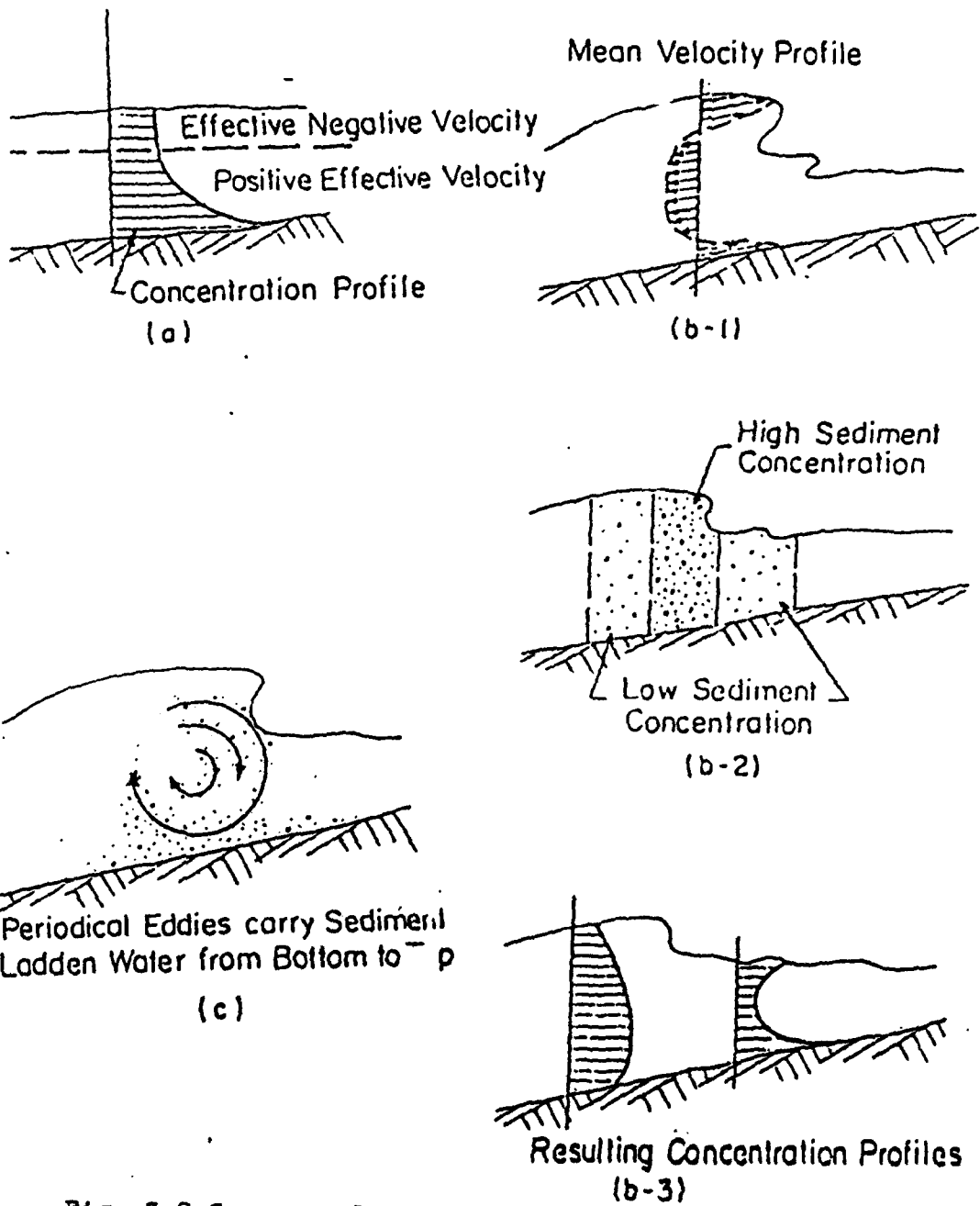


Fig. 3.8 Conceptual sketch of mechanisms that generate high concentration at higher elevation

2. Large horizontal sediment concentration gradient coupled with favorable mean flow profile such as illustrated in Fig. 3.8b,

3. The existence of stationary eddies or circulations in the surf zone to transport high sediment concentration water to the surface such as illustrated in Fig. 3.8c.

Certainly the combination of these causes could also yield higher sediment concentration at the surface layer. In this section, the effect of  $\bar{C}_w$  on the vertical concentration distribution is pursued further.

Settling velocity of sediment particles in oscillatory flow field has been found to be smaller than that in calm water by a number of investigators. Ho (1964) showed that under large acceleration, fall velocity can be reduced by as much as 70 percent. Murray's result (1970) showed that under a normal turbulent river condition, 40 percent reduction in fall velocity is possible. Wang, S.-Y. (1981) and Lee (1981) conducted experiments on particle fall velocity in wave field. Their results yielded large reduction in fall velocity near the surface; this reduction diminishes exponentially as particles settled further downward.

Wang, S.-Y. (1981) introduced a so-called effective fall velocity concept and was able to produce vertical concentration profile that has a minimum at mid-depth. Nielsen (1979) also discussed the fall velocity reduction in a fluctuating flow field but did not pursue further in his analysis. If  $\overline{C_w v_w}$  term represents a perturbation on  $C_w$  and the presence of nonuniform vertical velocity field is to cause reduction in particle fall velocity, we assume the following relationship:

$$-\overline{C_w} + \overline{C_w v_w} = -\overline{C_w} \quad (3-10)$$

where  $w$  is the effective fall velocity defined as

$$w = w_0 - R W \quad (3-11)$$

where  $R$  is a fall velocity reduction coefficient and  $W$  is the amplitude of the nonuniform vertical flow velocity. In a wave field, we have  $W = v_w$ , =amplitude of  $v_w$ .

Substituting Eq. (3-10) into Eq. (3-9), we have

$$-\overline{C_w} - \xi \frac{d\overline{C}}{dz} = 0 \quad (3-12)$$

This equation has the same form as the conventional vertical diffusion equation except that  $w$  is no longer a constant but varies with  $v_w$ . Integrating this equation yields the following concentration relationship:

$$C(z) = C_0 \text{Exp}\left[-\int_{z_0}^z \frac{1}{\epsilon} (w_0 - RW) dz\right] \quad (3-13)$$

where  $C_0$  is the sediment concentration at reference level  $z_0$ . For convenience, the overbar is dropped from this point on. The integration can be carried out if  $w_0$ ,  $R$  and  $\epsilon$  are given. Furthermore if both  $C_0$  and  $z_0$  can be determined,  $C(z)$  is then quantitatively solved. The problems of selecting  $\epsilon$ ,  $R$  and  $z_0$  are dealt with in the following sections.

### 3.5 Diffusion Coefficient Selection

As indicated in Table 3.7, there are a great number of different assumptions on  $\epsilon$ . After examining all possibilities, the author concluded that a modified hypothesis of Wang and Liang (1975) appears to be most plausible. Wang and Liang's original assumption is that the diffusion coefficient,  $\epsilon$ , is proportional to a length scale,  $l$ , which they treated as constant, and a velocity

scale,  $v$ , which they assumed to be proportional to the vertical component of the wave motion. Here, the modified assumption uses the same velocity scale but the length scale is no longer treated to be constant but proportional to the vertical excursion of the water particle motion, i.e.,

$$\epsilon = \kappa l v = \kappa v_w(z) \zeta(z) \quad (3-14)$$

where  $\zeta(z)$  is the amplitude of the vertical excursion of the water particle and  $\kappa$  is a constant of proportionality. For linear wave field, we have

$$\epsilon = \kappa H^2 \sigma \sinh^2 kz / (2 \sinh^2 kh) \quad (3-15)$$

In the breaking zone the eddy size is likely to be governed by the local wave height or local water depth, therefore, the suitable representation for at breaking zone or area of strong agitation is

$$\epsilon = \kappa H^2 \sigma \sinh kz / (2 \sinh kh) \quad (3-16a)$$

or

$$\varepsilon = K_H H \sigma \sinh kz / (2 \sinh kh) \quad (3-16b)$$

In the following paragraphs, the concentration profiles under strong agitation (breaking and surf zone) and normal agitation will be developed in parallel using Eqs. (3-15) and (3-16a).

Eq. (3-13) can now be integrated to yield the concentration profiles:

$$C/C_0 = \left( \frac{\tanh \frac{kz}{2}}{\tanh \frac{kz_0}{2}} \right)^{\frac{R \sinh kh}{K_H R}} \text{Exp} \left[ \frac{2W_0 \sinh^2 kh}{K_H^2 \sigma k} (\text{cth } kz - \text{cth } kz_0) \right] \quad (3-17a)$$

for nonbreaking, and

$$C/C_0 = \text{Exp} [R (z - z_0) / K_H] \left( \frac{\tanh \frac{kz}{2}}{\tanh \frac{kz_0}{2}} \right)^{-\frac{2W_0 \sinh kh}{K_H^2 \sigma k}} \quad (3-17b)$$

for breaking (and surf zone).

This solution is similar to Wang and Liang's except that the first part on the right hand side which is due to the modification of the effective fall velocity. For shallow water, Eq. (3-17b) reduces to:

$$C/C_0 = \text{Exp} [R (z - z_0) / K_H] \left( \frac{z}{z_0} \right)^{-\frac{2W_0 h}{K_H \sigma}} \quad (3-18)$$

In the above integration,  $w_0$  is assumed to be a constant, which holds only for uniform sediment size. In nature, beach sands are nonuniform. Consequently,  $w_0$  cannot be treated as a constant. Nielsen (1979) considered this problem by assuming that the fraction of suspension of each sand component,  $C_i$  with corresponding fall velocity  $w_i$ , is proportional to the percentage of the component in the bed material, and each component follows the same dispersion law, i.e.,

$$C_i(z, w_i) = C_{o,i}(w_i) \text{Exp} \left[ -\int_{z_0}^z \frac{1}{\bar{w}_0} (w_i - kW) dz \right] \quad (3-19)$$

where  $C_{o,i}(w_i)$  is the fraction of the  $i$ th sand component at reference level  $z_0$ . Introducing the following dimensionless parameters,

$$w' = w_i / \bar{w}_0 \quad (3-20)$$

and

$$C_{o,i}'(w') = C_{o,i}(w') / C_o \quad (3-21)$$

where  $C_o$  is the total sediment concentration at the reference level  $z_0$  and  $\bar{w}_0$  is the mean fall velocity. Let

$f(w')dw'$  represents the probability density function of  $C_{s,i}$ . Eq. (3-19) can then be integrated to obtain the concentration distribution as follows:

$$C/C_0 = \int_0^{\infty} f(w') \text{Exp}\left[-\int_{z_0}^z \frac{1}{\epsilon} (w_0 w' - RW) dz\right] dw' \quad (3-22)$$

If  $\epsilon$  and  $R$  are assumed to be independent of  $w'$ , we have

$$C/C_0 = \int_0^{\infty} f(w') \text{Exp}[-\alpha w' - \beta] dw' \quad (3-23)$$

where  $\alpha = \int_{z_0}^z \frac{1}{\epsilon} \bar{w}_0 dz$  and  $\beta = \int_{z_0}^z \frac{1}{\epsilon} RW dz$ . A number of investigators have suggested a  $\Gamma$ -distribution function for the sediment distribution, such that

$$f(w') = \frac{(1/V)^W}{\Gamma(1/V)} \text{Exp}[-w'/V] w'^V \quad \text{for } 0 < w' < \infty \quad (3-24)$$

with  $V$  = the variance of the distribution function.

Substituting Eqs. (3-24) and (3-16a) or (3-15) into Eq. (3-23), the explicit solutions are obtained for sediment with nonuniform size distribution:

$$C/C_0 = \left( \frac{\tanh \frac{kz}{2}}{\tanh \frac{kz_0}{2}} \right)^{\frac{R \sinh \frac{kz}{2}}{kH^2 \epsilon}} \left[ 1 - V \frac{2 \bar{w}_0 \sinh^2 \frac{kz}{2} (\coth k z - \coth k z_0)}{k H^2 \epsilon} \right]^{-1/V} \quad (3-25a)$$

AD-A119 906

DELAWARE UNIV. NEWARK DEPT OF CIVIL ENGINEERING

F/G 8/3

WAVE KINEMATICS AND SEDIMENT SUSPENSION AT WAVE BREAKING POINT. (U)

JUN 82 P A HWANG, H WANG

N00014-81-K-0297

UNCLASSIFIED

CE-82-27

NL

20-2

1-1982

END  
DATE  
FILMED  
11 82  
DTIC

for nonbreaking, and

$$C/C_0 = \text{Exp}[R (z-z_0)/k_1 H] \left[ 1 + \frac{2V \bar{w}_0 \sinh kh}{k_1 H^2 R H} \ln \frac{\tanh \frac{kz}{2}}{\tanh \frac{kz_0}{2}} \right]^{-1/V} \quad (3-25b)$$

for breaking. In shallow water, Eq. (3-25b) reduces to

$$C/C_0 = \text{Exp}[R (\frac{z-z_0}{h}) / (k_1 H/h)] \left[ 1 + \frac{2V}{k_1 H/h} (\frac{\bar{w}_0}{H\sigma}) \ln \frac{z}{z_0} \right]^{-1/V} \quad (3-26)$$

In Eq. (3-26), we identify the following dimensionless expression:

$$C/C_0 = f(z/h, z_0/h, H/h, \bar{w}_0/H\sigma, V) \quad (3-27)$$

Under breaking condition,  $H/h$  fluctuates in a narrow range, the dimensionless groups can be further reduced to

$$C/C_0 = f(z/h, z_0/h, \bar{w}_0/H\sigma, V) \quad (3-28)$$

Fig. 3.9 illustrate respectively, the effects of  $z_0/h$ ,  $\bar{w}_0/H\sigma$  and  $V$  on the vertical sediment distribution. It is clear that  $z_0$ , as a mathematical reference level, does not affect the concentration profile shapes. parameters

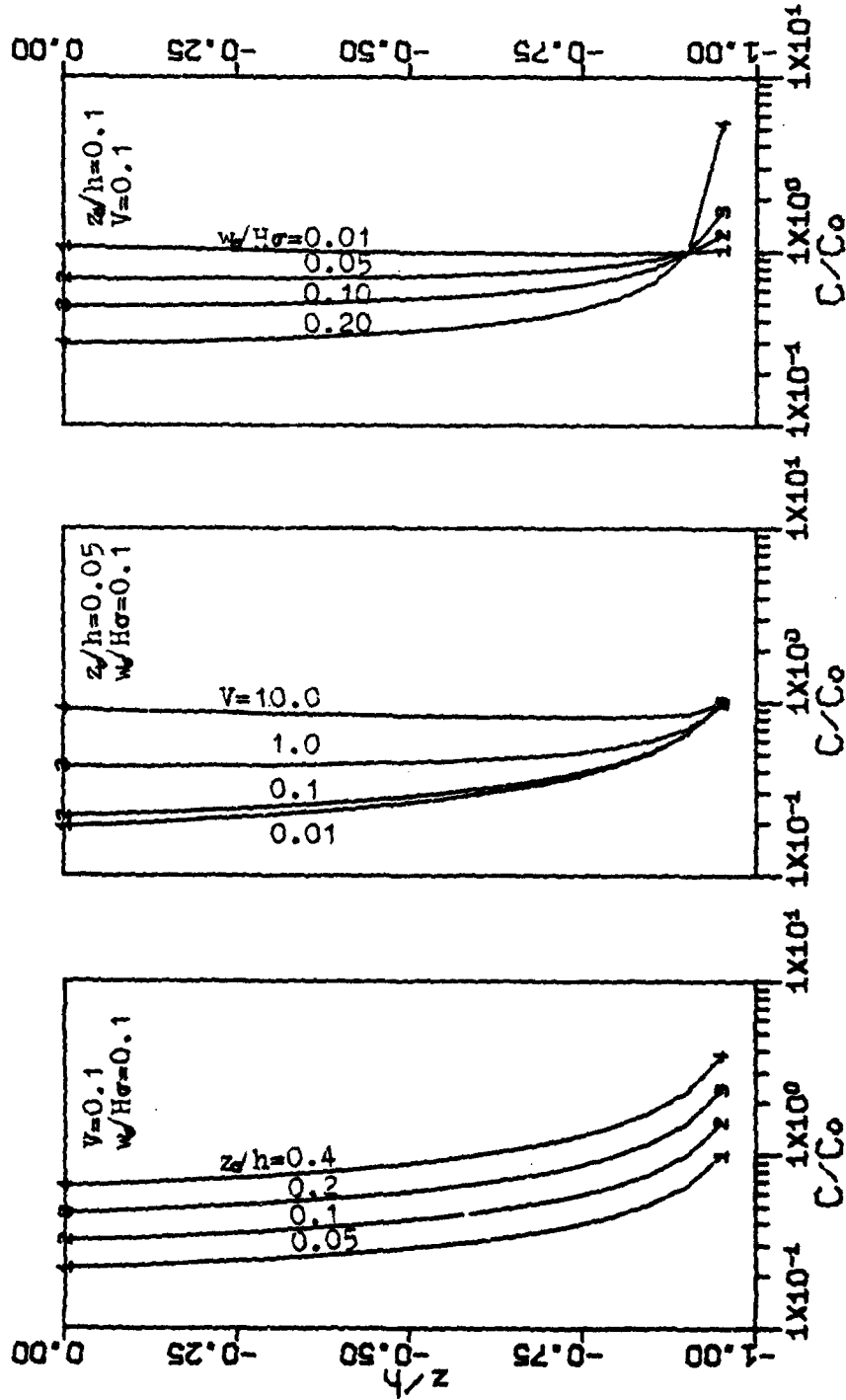


Fig. 3.9 Functional relationship of the concentration profiles with  $z/h$ ,  $V$  and  $w/H\sigma$

$\bar{w}_o/H\sigma$  denotes the agitation level; the higher agitation (lower  $\bar{w}_o/H\sigma$ ), the more uniform distribution.  $V$ , the sediment distribution variance, denotes the availability of the suspendable sediments; the poorer the sorting (larger variance), the more abundant the light material that could be carried to a higher elevation, therefore showed more uniform distribution beyond bedload level.

### 3.6 Fall Velocity Reduction

One of the important assumptions made in the derivation of the vertical sediment concentration profile is that the mean sediment particle fall velocity is reduced due to wave agitation. The magnitude of reduction is assumed to be proportional to the amplitude of the vertical water particle velocity, i.e.,

$$w/w_o = 1 - RW/w_o \quad (3-29)$$

The value of  $R$  must first be established. A simple analysis based upon consideration of change in drag force in oscillatory flow is presented here.

Under equilibrium condition, the force balance on a particle in calm water can be expressed as:

$$G = C_D A w_o^2 / 2 \quad (3-30)$$

where  $G$  is the gravitational force;  $C_D$  is the drag coefficient;  $A$  is the projected surface area and  $w_o$  is the fall velocity in calm water. In oscillatory flow, the above equation is modified as

$$\frac{1}{2\pi} \int_{-\pi}^{\pi} C_D' (w - W \sin t) |w - W \sin t| dt = G \quad (3-31)$$

where  $C_D'$  is the instantaneous drag coefficient;  $w$  is the fall velocity in oscillatory flow and  $W$  is the amplitude of vertical velocity component. Equating Eqs. (3-30) and (3-31) and solving the  $w/w_o$ , we obtain

$$w/w_o = \left[ \frac{C_D}{C_D'} - 0.5 (W/w_o)^2 \right]^{1/2} \quad (3-32)$$

for  $W/w < 1$ , and

$$w/w_o = \frac{2 C_D}{\pi C_D'} \left[ 1 + 0.5 (W/w)^2 \sin^{-1}(W/w) + 1.5 \sqrt{(W/w)^2 - 1} \right]^{-1/2} \quad (3-33)$$

for  $W/w > 1$ .

Thus, the reduction in fall velocity in oscillatory flow is a function of  $C_D/\overline{C}_D$  and  $W/w_0$ . Fig. 3.10 plots this functional relationship with various  $C_D/\overline{C}_D$  ratios together with the available laboratory data. The data showed a large scatter. It is difficult to claim any of these curves is the correct one. On the other hand, it is evident that the fall velocity reduction in oscillatory flow is quite significant, particularly when  $W/w_0$  becomes large. Consequently, in a high agitation field, the reduction in fall velocity is expected to be larger than most of the data presented. For the data reported in the study, the values of  $W/w_0$  were in the order of 15 for the laboratory conditions and even larger (of the order of 30-40) for field conditions. To simplify our computations, we treated  $R$  as a constant and set it to be equal to 0.07 for  $W/w_0 < 14.3$  by data fitting. For extremely high agitation, the sediment particle becomes passive and will be treated as neutral buoyant beyond  $W/w_0 > 14.3$ . This resulted in a straight line relationship between  $w/w_0$  and  $W/w_0$  such as shown in Fig. 3.10. If this cut-off velocity of  $W/w_0 = 14.3$  is not made, negative fall velocity occurs, which results in the inversion of the concentration profiles beyond this critical velocity (see Fig. 3.15, Test 12 and 13). The

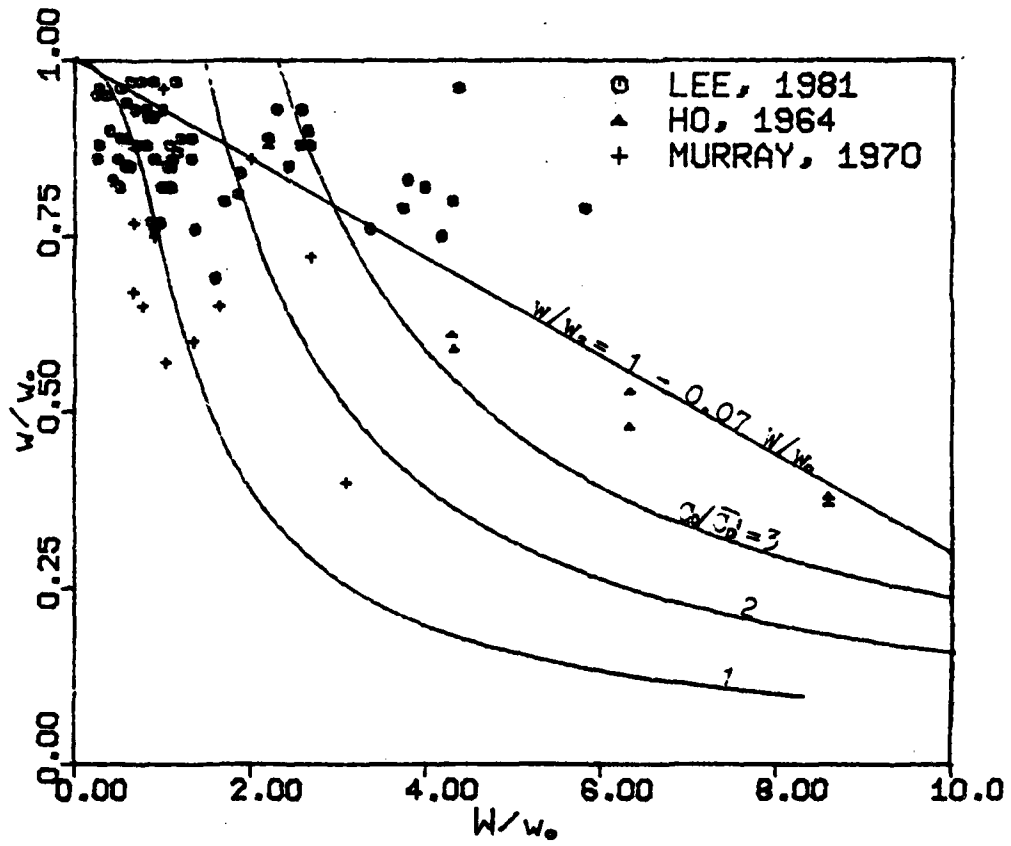


Fig. 3.10 Fall velocity reduction in an oscillatory flow field

concept of negative fall velocity needs more careful examination, however.

### 3.7 Determination of Reference Level $z_0$

The vertical sediment concentration profile discussed above is based upon diffusion consideration and is, therefore, only valid for suspended load in the region above the bed load layer. The magnitude of the suspended sediment concentration (Fig. 3.9) depends upon the value  $z_0$  and the corresponding concentration  $C_0$ . Mathematically,  $z_0$  can be chosen arbitrarily in the suspended sediment region as long as  $C_0$  can be determined. Physically, this implies  $z_0$  should be chosen at the boundary where  $C_0$  can be given as a boundary value or determined by considerations other than suspended load equation. In river flow, Einstein (1950) suggested  $z_0$  be chosen at the water edge of bed load layer. For sand bed, he suggested  $z_0 = 2d$ , with  $d$  = diameter of the sand particle. This criterion runs into difficulty for fine sand or silt material; it also becomes impractical for rough or rippled bed. Nielsen (1979), Nielsen and Green (1981) among others chose the ripple crest level for reference which may be inside the bedload layer.

Besides, measurement of concentration at that level was generally scarce and had to be extrapolated, subject to personal interpretation and large error due to the scarce measurements at the vicinity. In this study, the author chose the reference level at the boundary layer elevation using equations of Jonssen and Carlsen (1976):

$$\delta/\xi_b = 0.072(k_r/\xi_b)^{1/4} \quad (3-34)$$

here  $\xi_b$  is the amplitude of the horizontal particle excursion at bottom and  $k_r$  is the Nikuradse roughness taken as an arbitrary number as 120 d followed Nielsen and Green. For rippled bed, the following modified equation for  $k_r$  was suggested by them:

$$k_r = 120 d + 1.27 \eta_r \quad (3-35)$$

with  $\eta_r$  = ripple height.

Based upon this reference level, the reference concentration data obtained by various investigators are plotted against Shields parameter in Fig. 3.11. The Shields parameter is defined as

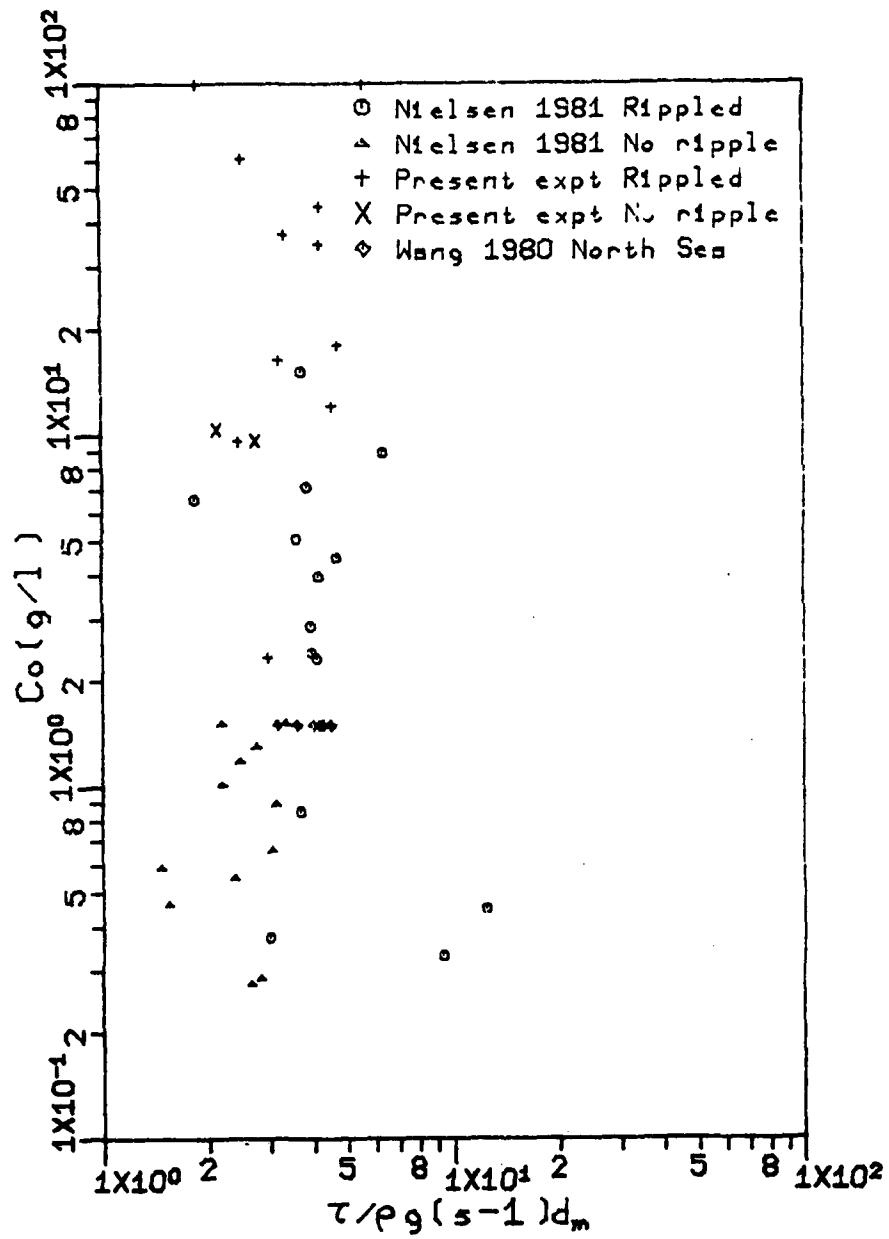


Fig. 3.11 Reference concentration at boundary layer level as a function of Shields parameter

$$\tilde{\psi} = \tau / \rho g d (s-1) \quad (3-36)$$

where

$$\tau = \frac{1}{2} f_w u_b^2 / 2 \quad (3-37)$$

$$f_w = \text{Exp}[5.213(k_r/\xi_b)^{0.194} - 5.997] \text{ for } \xi_b/k_r > 1.7$$

$$= 0.28 \quad \text{for } \xi_b/k_r < 1.7 \quad (3-38)$$

by Jonsson (1966),  $u_b$  is the horizontal particle velocity of wave motion at bottom. The data shown here are rather scattered; thus quantitative dependency on  $\tilde{\psi}$  is not clear. Note that the scatter of  $C_s - \tilde{\psi}$  relationship did not improve when only the surface drag were considered for the Shields parameter calculation, for example, see Nielsen, 1979 and Nielsen and Green, 1981.

### 3.8 Field and Laboratory Data Presentation

The analysis presented in the previous section presumes that when the fluid is in a state of high agitation such that the flow is fully turbulent, the characteristic eddy scale is proportional to the wave

height; while in a less agitating state, the eddy size is proportional to the amplitude of vertical particle motion. This study emphasizes the former condition, field data collected in the surf zone and laboratory data collected at wave breaking point and surf zone were used. The conditions under which these data were obtained have been described in the previous sections. In addition, a few sets of data from Nielsen and Green were also included.

Thirteen sets of laboratory data are given in Fig. 3.12, together with the theoretical curves in accordance with Eq. (3.17b). The value is data fitted; two values of 0.4 and 0.25 are given to show the range of variations. The correlation coefficient of the theoretical values and the measured quantities is used as a measure of the goodness of fit. The correlation coefficient is defined as

$$Y = \text{Cov}(C_T, C_M) / \sqrt{\text{Var}(C_T) \cdot \text{Var}(C_M)} \quad (3-39)$$

where  $\text{Cov}(C_T, C_M)$  is the covariance of functions  $C_T$  and  $C_M$ , and  $\text{Var}(q)$  is the variance of function  $q$ .  $C_T$  is the theoretical results and  $C_M$  is from measurement.

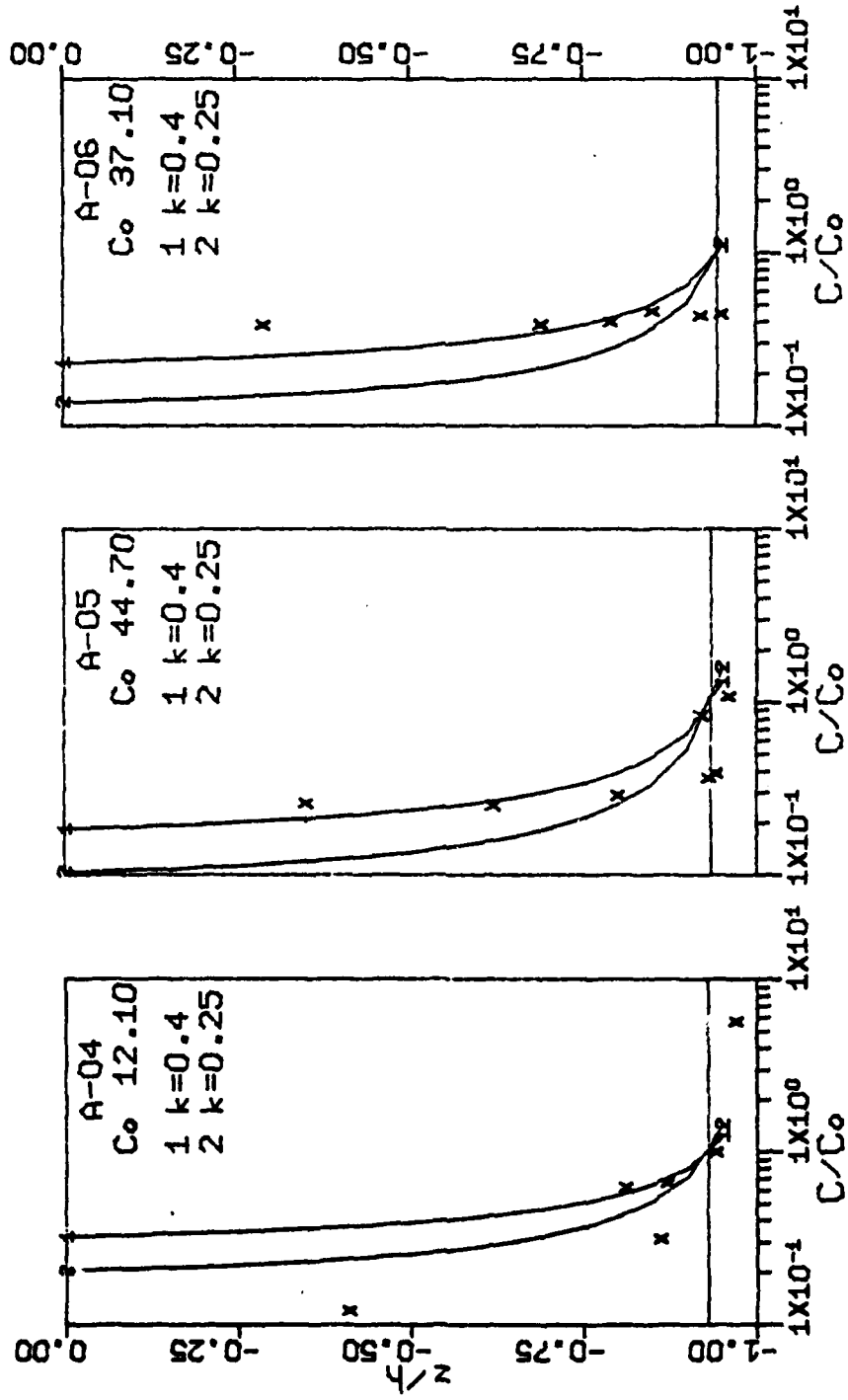


Fig. 3.12 Comparison of the suspension model with the present laboratory data

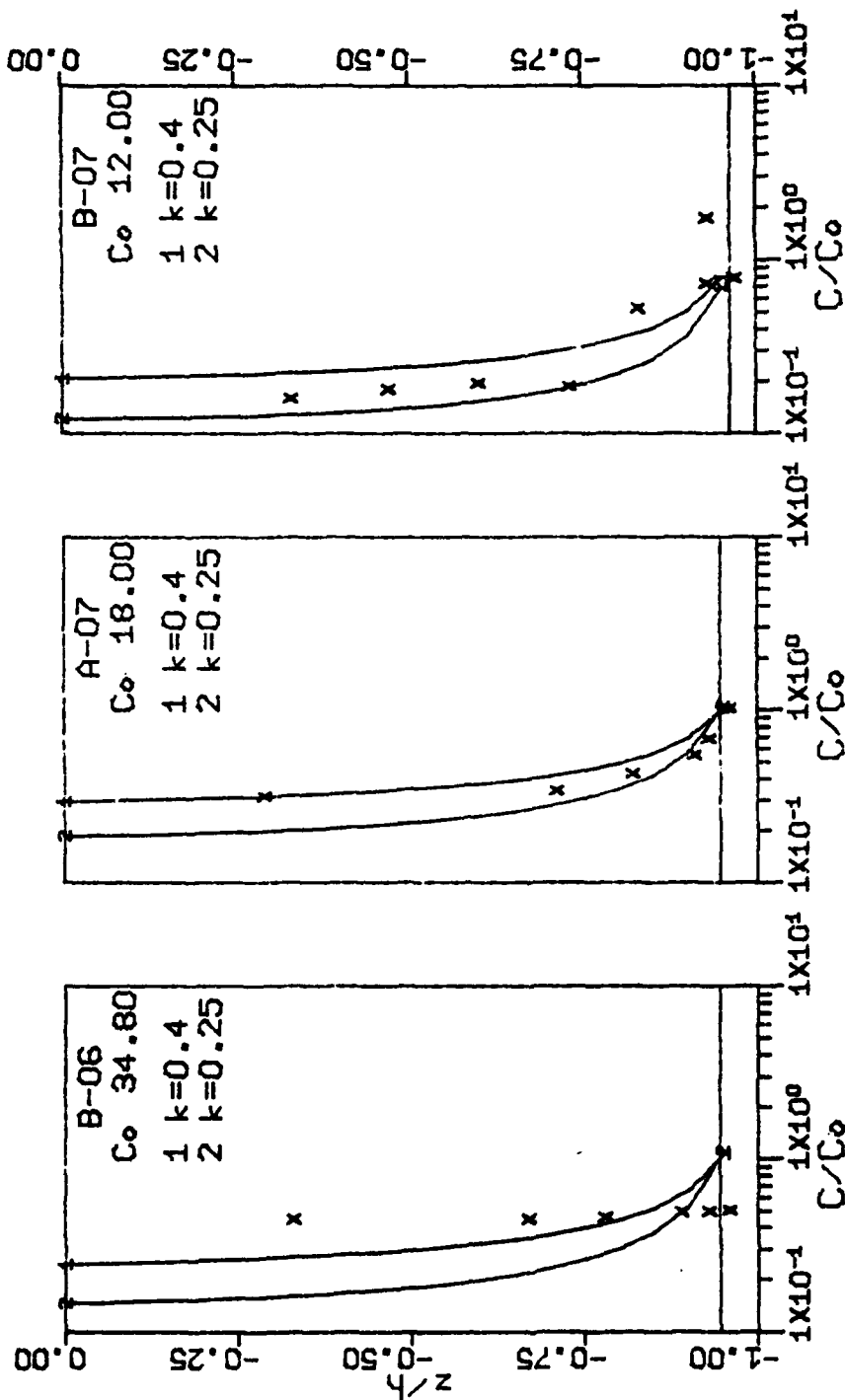


Fig. 3.12 (continued)

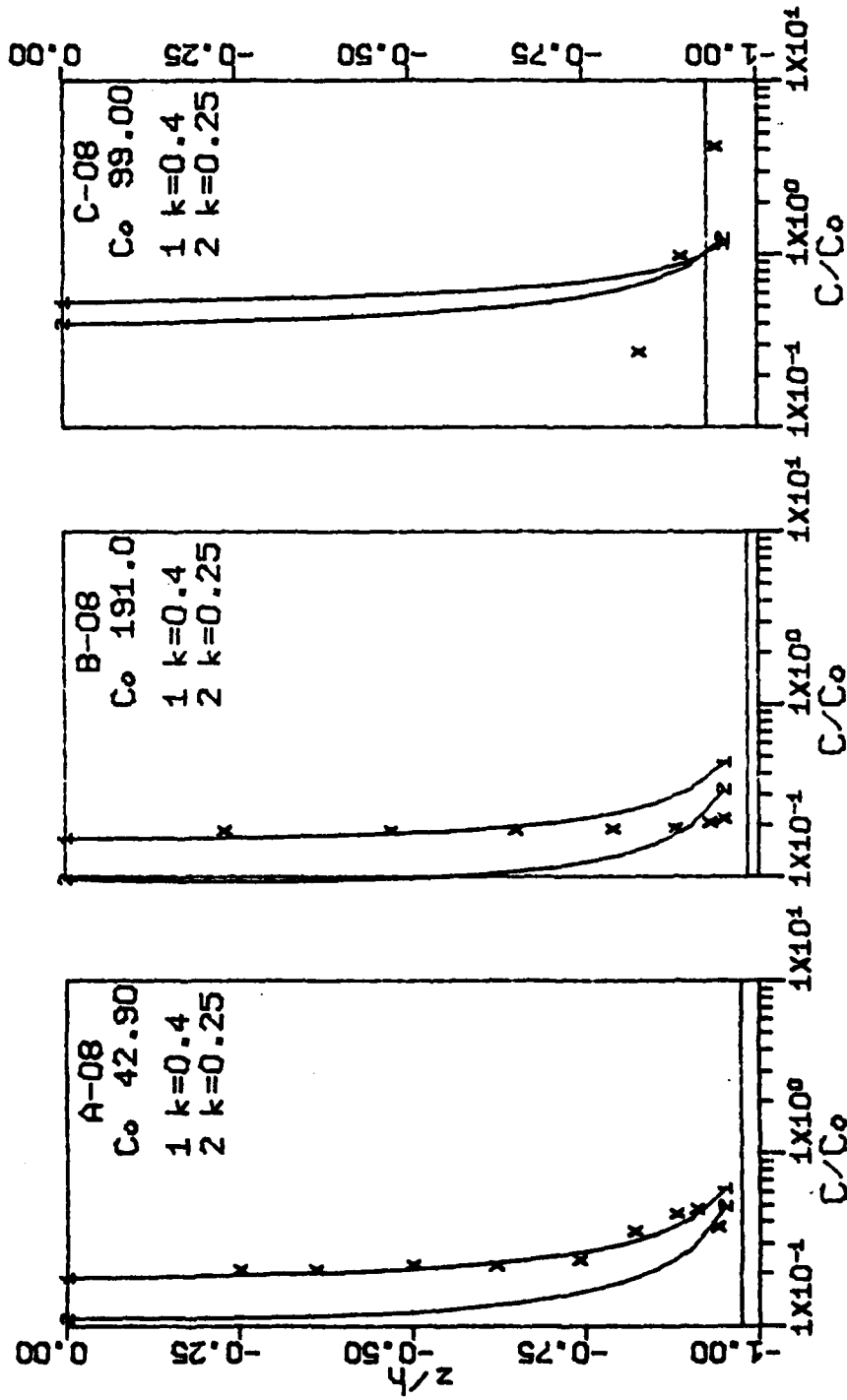


FIG. 3.12 (continued)

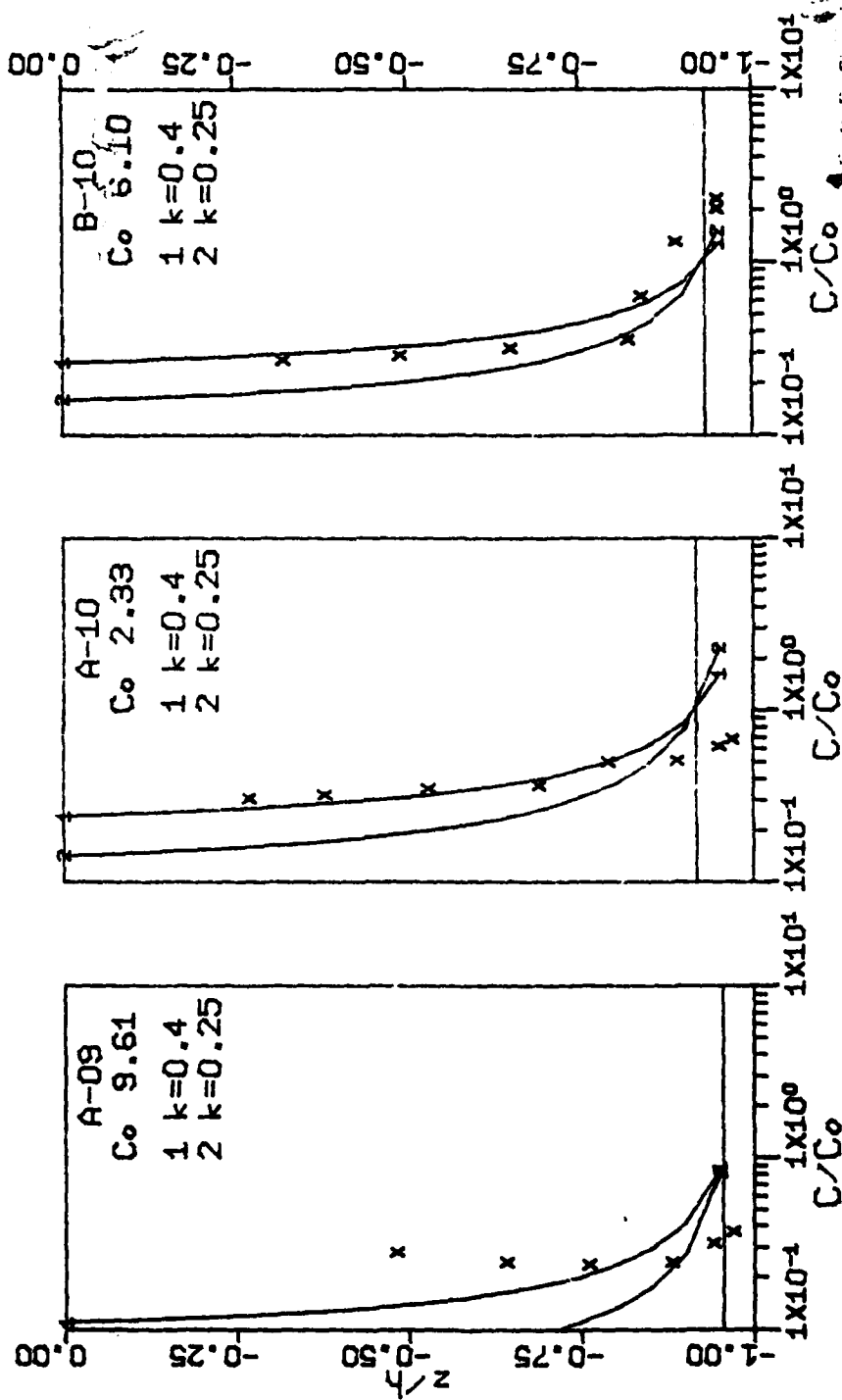


Fig. 3.12 (continued)

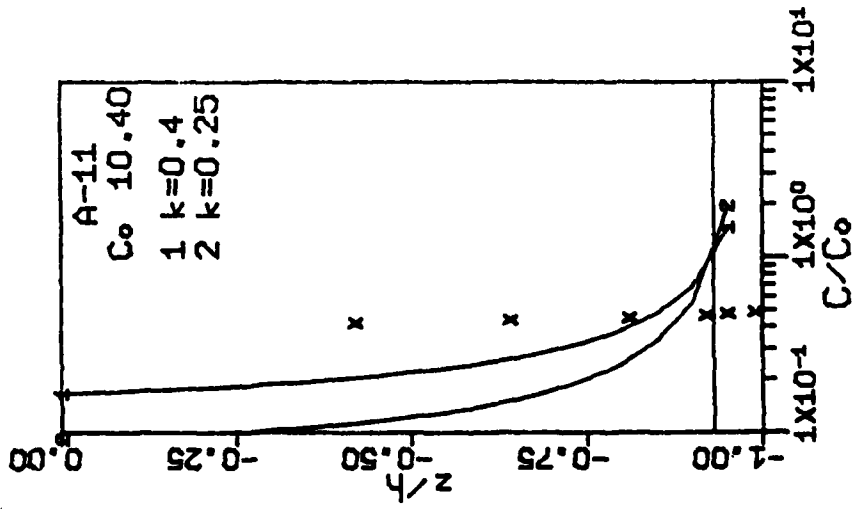


FIG. 3.12 (continued)

Fig. 3.13 shows the distribution of the goodness of fit. It is seen that 10 out of 13 cases show .80 or higher correlation. Fig. 3.14 presents the results of the North Sea data. Since no measurements at close to the bottom was made, reference concentration evaluation is difficult. An uniform 1.5 gram/liter is assigned arbitrarily to facilitate computation. Although quantitative conclusion is difficult to draw with only three data points in each profile, the trend does show the high agitation, large sand variance type distribution (Fig. 3.9b, c) as characterized at the measuring site.

A total of 21 sets of data from Nielsen and Green were computed. The correlation distribution is also shown in Fig. 3.13. 17 sets of them are above 0.8. Fig. 3.15 shows some of the typical results.

In the last section, Eq. (3-17a) is suggested for the concentration computation for weak agitation conditions. Although thorough testing was not done, a brief computation of the ratio between nonbreaking and breaking concentration under similar wave condition is compared to the measurements of Nielsen 1979, Fig. 6.25; reproduced as Fig. 3.16 here). Since wave condition was not complete in the original report, the following

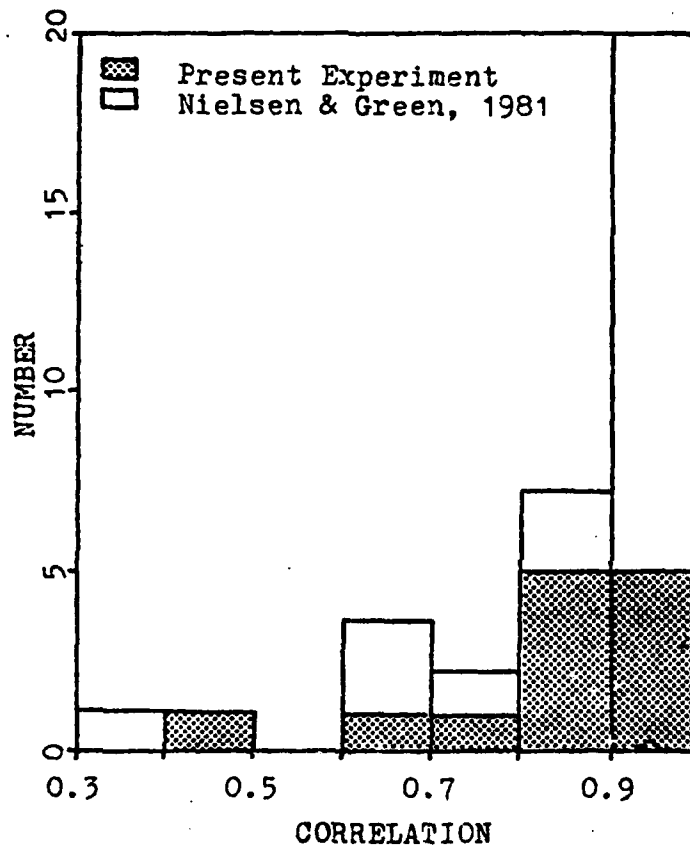


Fig. 3.13 Goodness of fit of the experimental data with the theoretical results

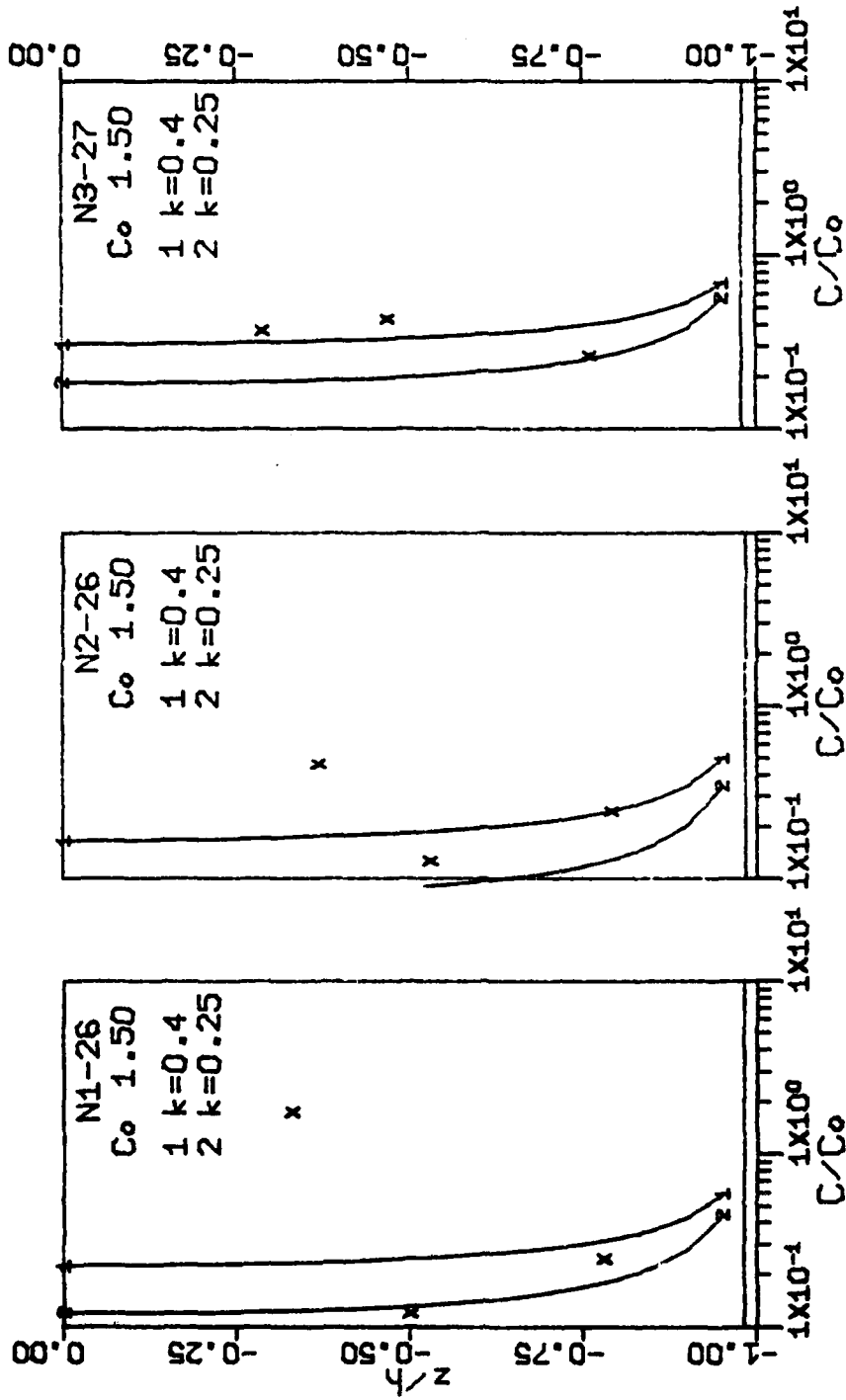


Fig. 3.14 Comparison of the suspension model with North Sea data

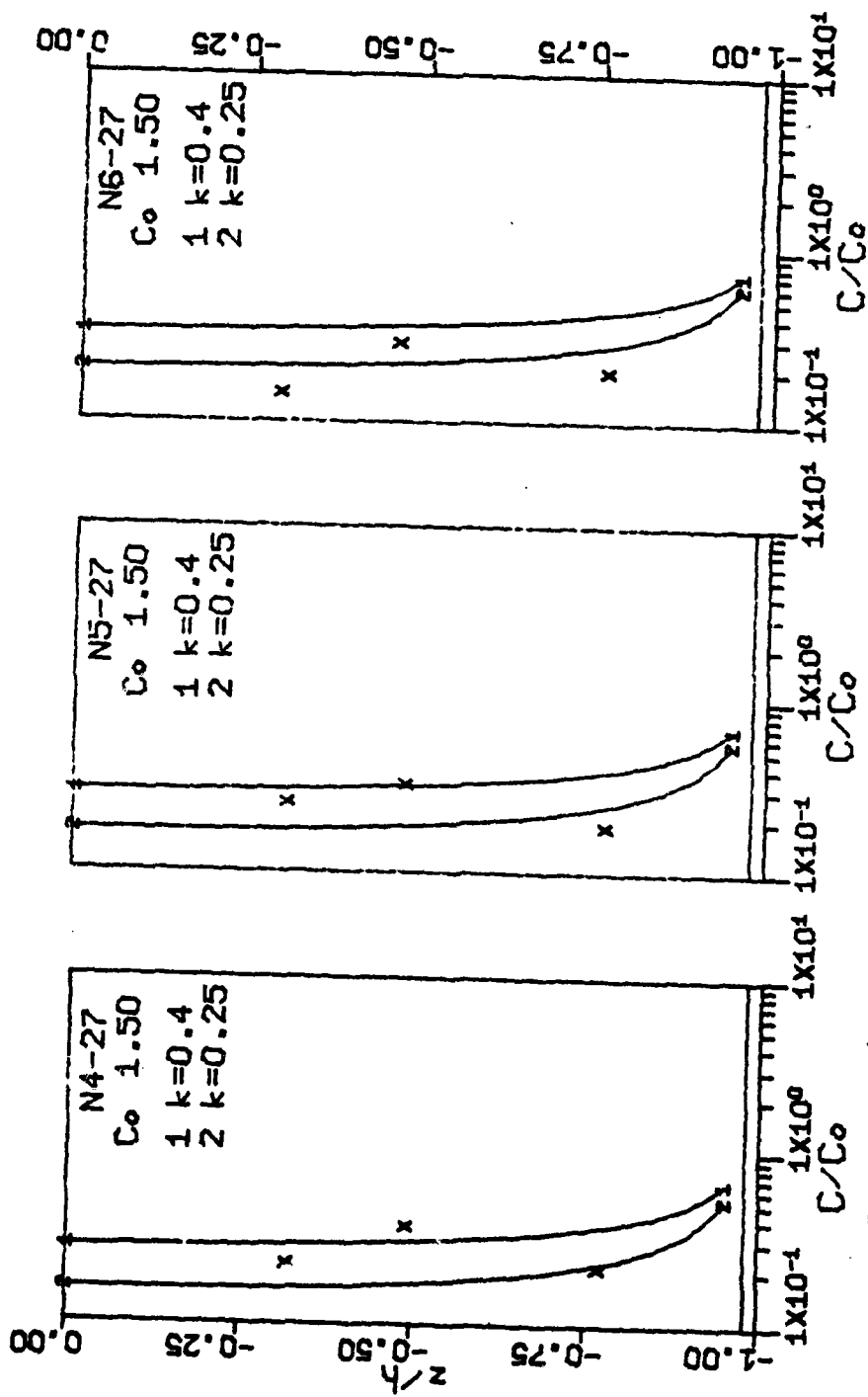


FIG. 3.14 (continued)

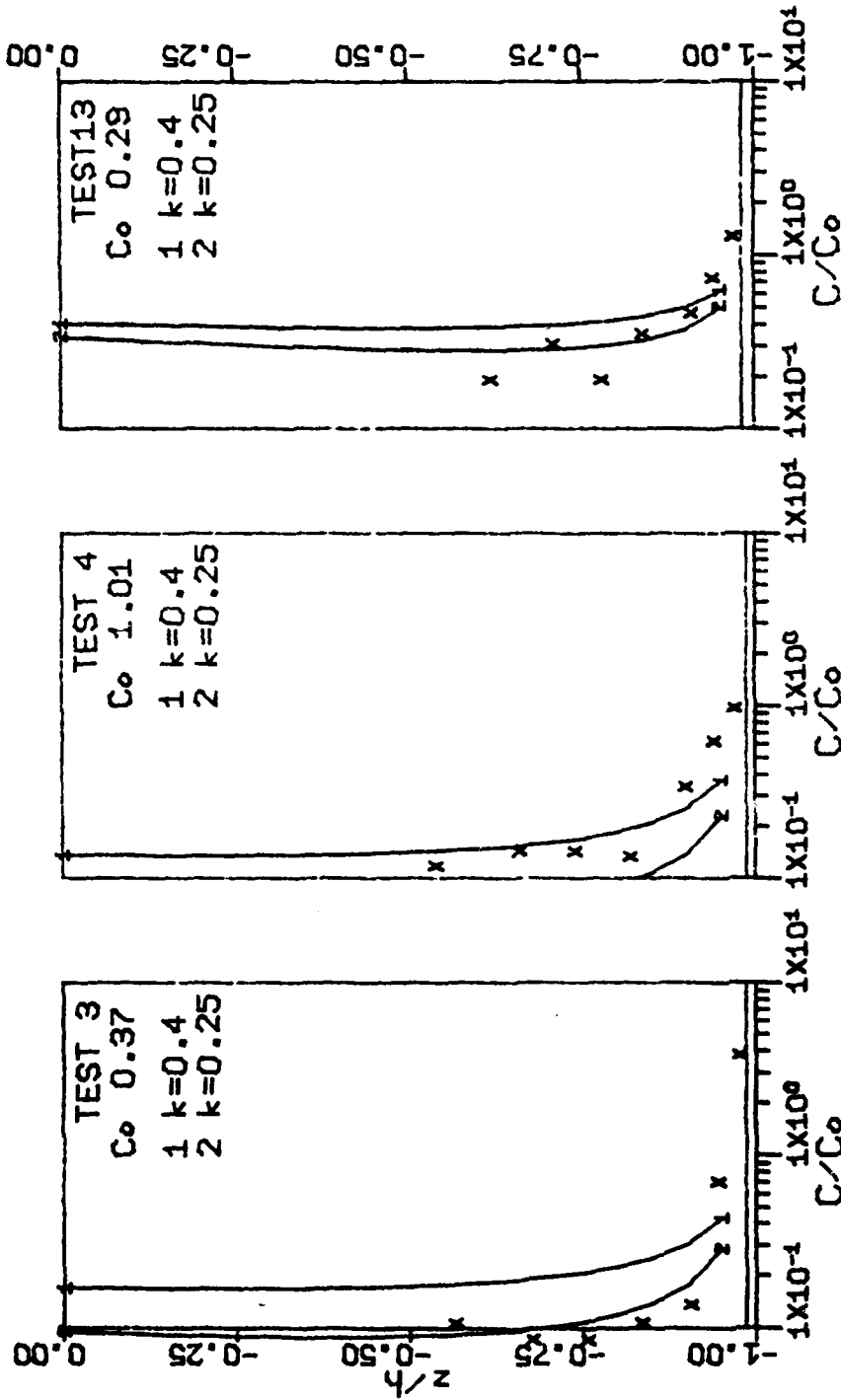


Fig. 3.15 Comparison of the suspension model with data from Nielsen & Green (1981)

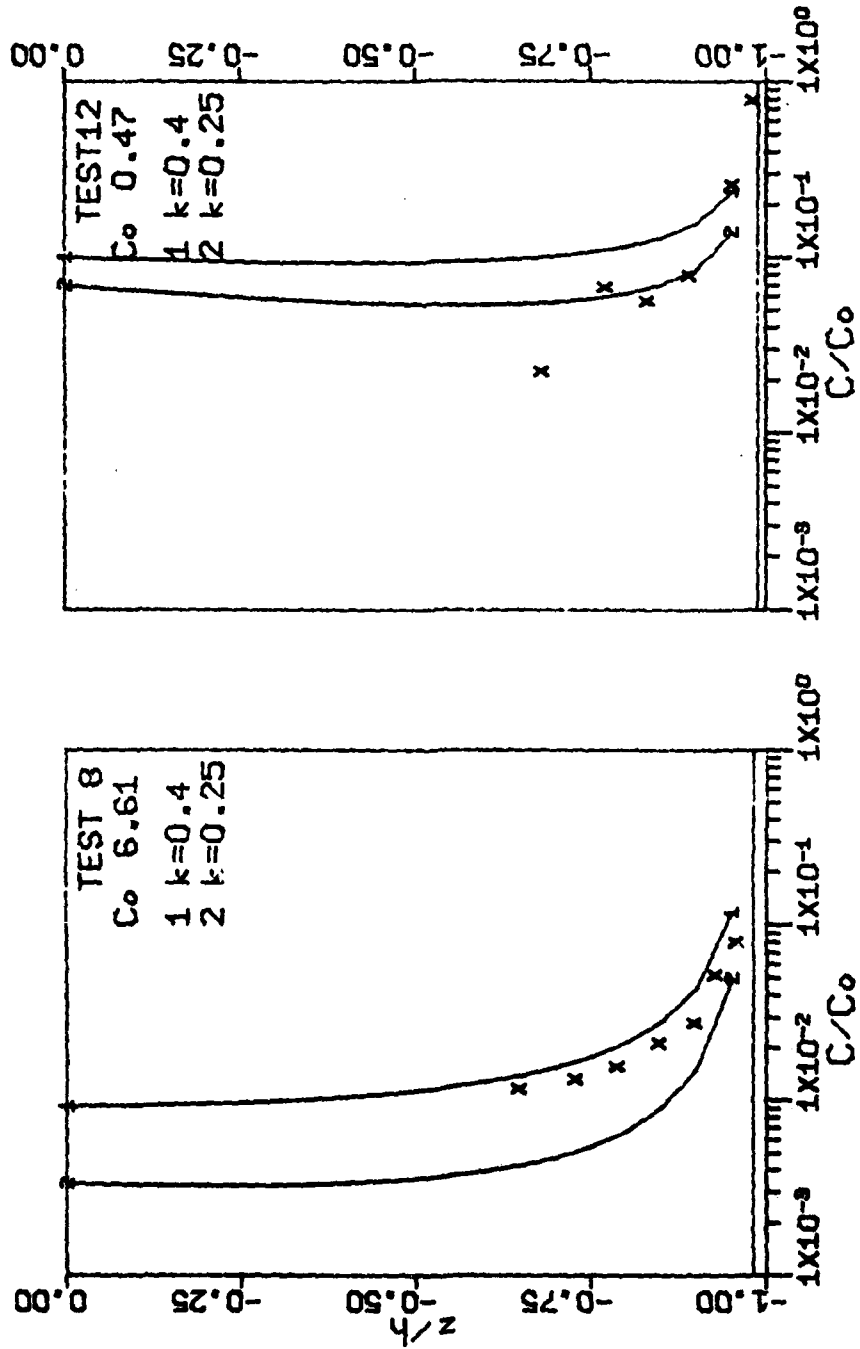


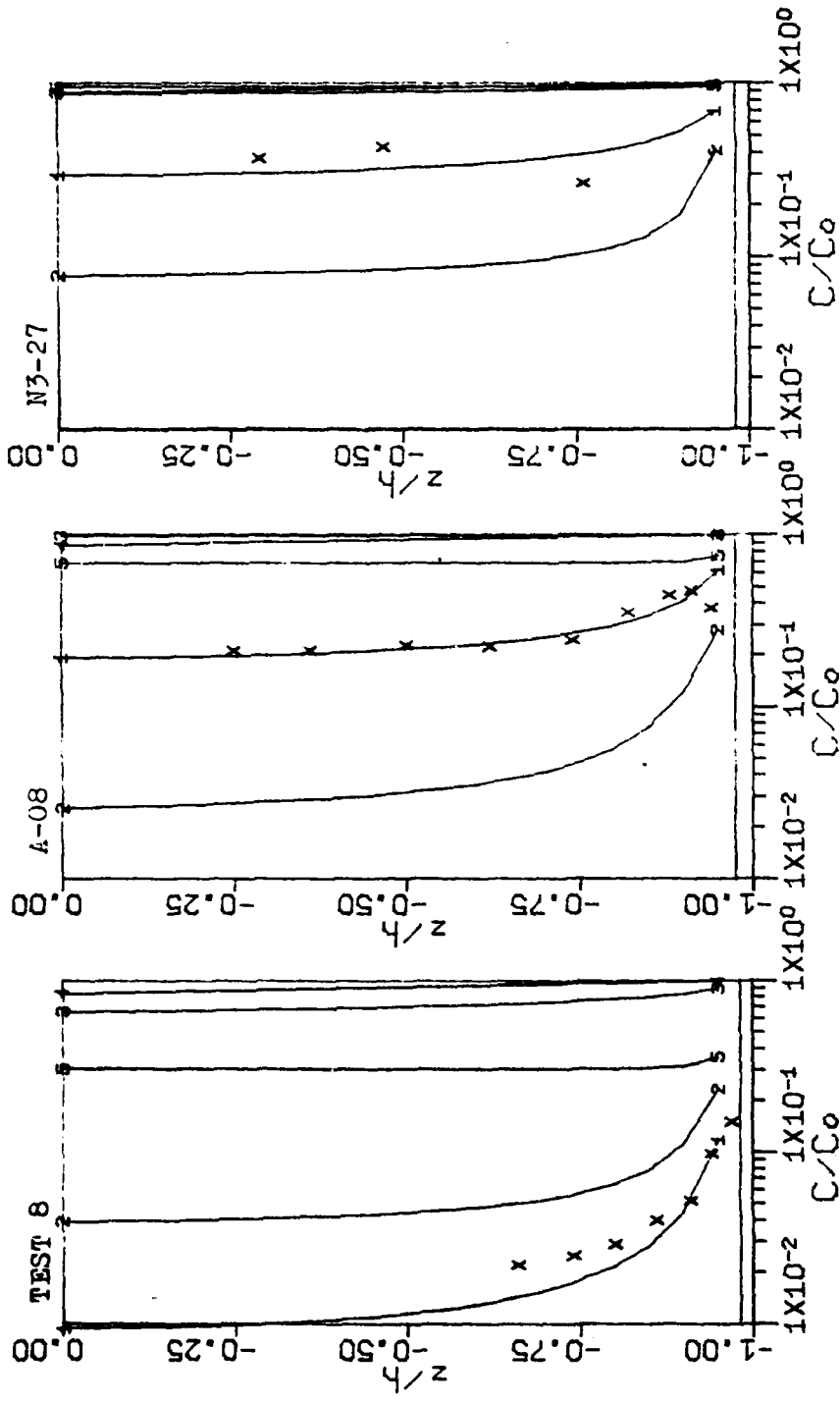
Fig. 3.15 (continued)



approximation is used:  $kh=0.3$ ,  $\bar{w}_o/H\sigma=0.1$ ,  $H/h=0.5$ ,  $kH=0.02$ ,  $z_o/h=0.025$ ,  $v=0.3$ . The result shows a ratio of 1/100 at mid-depth which is very close to what was measured.

Fig. 3.17 shows the comparison of the present model with the models developed by Nielsen and Green, Wang and Liang, Hom-ma and Horikawa, and Dally. It can be seen that for the high agitation cases, only the Nielsen and Green model is comparable with the present results. Their model, however, introduced a lot of data fitted coefficients with large uncertainties while the present model used least number of data fitted coefficients.

As a concluding remark to this chapter, sediment suspension under wave agitation can be properly modelled as diffusion processes. The turbulent viscosity is closely related to the wave properties and degree of agitation. The suitable velocity scale is the vertical water particle velocity, the length scale is the wave height, or water depth for shallow case; under strong agitation, the length scale is uniform over the whole depth, while at weaker disturbances, the scale decays with water depth, therefore, the amplitude of the



1 Present model 2 Nielsen & Green 3 Wang & Liang  
 4 Dally 5 Homma & Horikawa

Fig. 3.17 Comparison of different sediment suspension models with experimental data

vertical excursion is more appropriate. Sediment grading as well as strength of agitation affects the concentration profiles, the stronger agitation and the poorer the sorting, the more uniform distribution over the depth occurs. The reference level, however, only affects the absolute values and any level that will give accurate measurement is appropriate. The effective fall velocity under oscillatory flow modifies the distribution and needs to be properly considered. The present linear model is only a first order approximation, further studies are desired for a better understanding of this problem. The relationship of the reference concentration to the flow and sediment properties is still uncertain and need more detailed investigation.

## CHAPTER 4 WAVE AND VELOCITY SPECTRA

### 4.1 Introduction

In this study, all the waves were monochromatically generated. At breaking, however, the spectra of these waves are broadened by nonlinear interaction. The spectra do not show a fixed slopes which is typical for waves in finite water depth. Huang et al. (1981) developed a spectral model for general sea state in deep water. The spectral slope is a function of  $\bar{\eta}^2/L$ , which is determined by two "internal" parameters, the primary peak frequency (which gives  $L_0$ , the primary wave length) and the variance which are routinely recorded in the experiments. Extension of this model to the finite depth water is discussed. The controlling parameter becomes Ursell number,  $Ur' = H/k^3 h^3$ , which includes the depth as expected. This model compares reasonably well with the experiment data in the energy containing frequency band. At higher frequencies, the deviation becomes generally large. An alternative of

using the stream function theory to simulate the spectrum shows far better agreement for the full frequency range. The stream function theory also shows good agreement with the horizontal and vertical velocity spectra.

#### 4.2 A Brief Summary of the Wallops Spectral Model

Detailed exposition of the Wallops spectral model can be found in Huang et al. (1981). For the sake of completeness, a short description will be given as follows.

The form of the Wallops spectrum is based on a narrowband Fourier expansion of the surface wave form

$$\eta = \sum_n a_n \cos X_n \quad (4-1)$$

with  $X$  is the phase function, and  $a_n$  is the amplitude of each Fourier component. The simplest form of this expansion for deep water waves is the Stokes wave,

$$\eta = a \cos X + 1/2 a^3 k_0 \cos 2X \quad (4-2)$$

where  $a$  is the amplitude of the fundamental wave and  $k_0$  is the wave number. Based on extensive observations in

the laboratory, Huang et al. found that the slope of the high frequency side of the spectrum,  $m$ , can be determined by the relative magnitudes and positions of the primary and the second harmonic components. Consequently,

$$m = \log(a_1^2/a_2^2)/\log(2 \sigma_0/\sigma_0) = 2 \log(\sqrt{2} \pi g)/\log 2 \quad (4-3)$$

With the high frequency part determined, the whole spectrum for deep water waves can be expressed in a similar way as the generalization of Pierson and Moskowitz (1964) applied to Phillips' saturation range spectrum,

$$S_s(\sigma) = \frac{\beta g^2}{\sigma_0^5} \left(\frac{\sigma_0}{\sigma}\right)^m \exp\left\{-\frac{m}{4} \left(\frac{\sigma_0}{\sigma}\right)^4\right\} \quad (4-4)$$

where  $S_s$  denotes the wave surface spectrum and

$$\beta = \frac{(2\pi g)^2 m^{\frac{m-1}{4}}}{4^{\frac{m-5}{4}}} \frac{1}{\Gamma\left(\frac{m-1}{4}\right)} \quad (4-5)$$

in which  $\Gamma(\cdot)$  is the gamma function. The Wallops spectrum approaches Pierson-Moskowitz spectrum at saturation stage or  $m \rightarrow 5$ . It also eliminates the need of empirical coefficients, all the parameters are internally determined, and the spectrum correctly represents the

total energy content through the definition of  $\beta$ . More detailed discussion of this model can be found in the original paper (Huang et al., 1981).

#### 4.3 Wallops Spectrum in Finite Depth Water

Waves in water of finite depth behave quite differently from the deep water ones. As the depth of the water becomes shallower, the effect of the bottom will be felt by the waves. This will produce important changes in the wave profile, phase velocity and dispersion relationship. This section discusses the modification of the Wallops spectrum using the finite depth Stokes theory, cnoidal theory, solitary theory and stream function theory. While the former three theories predict reasonable agreement near the main peaks for a limited  $kh$  range, the stream function theory shows much better agreement over the whole frequency range and the range of relative water depth of this experiment ( $kh=0.2$  to  $1.0$ ). The derivation of each case follows.

#### Finite Depth Stokes Waves

A profile of the Stokes wave in intermediate water can be found in Stokes (1880), Bowden (1958), De (1955) and Wehausen and Laitone (1960). All the profiles are essentially equivalent. Let's use the expression by Stokes and Bowden,

$$\eta = a \cos X + a^2 k \coth kh \left(1 + \frac{3}{2 \sinh^2 kh}\right) \cos 2x \quad (4-6)$$

Then following the same approach as outlined in the previous section, we can write the slope of the high frequency range of the spectrum as

$$m = 2 \log \left[ 2\pi \xi \coth kh \left(1 + \frac{3}{2 \sinh^2 kh}\right) \right] / \log 2 \quad (4-7)$$

and

$$\beta = \frac{(2\pi \xi)^2 m^{\frac{m-1}{2}} \tanh^2 kh}{4 \frac{m-5}{2}} \frac{1}{\Gamma\left(\frac{m-1}{2}\right)} \quad (4-8)$$

Comparing the expressions of Eqs. (4-7) and (4-8) with (4-3) and (4-5) the difference is obvious. In water of finite depth, we need two parameters  $\xi$  and  $kh$ , to define  $m$  and  $\beta$ . The values of  $m$  and  $\beta$  as functions of  $\xi$  and  $kh$  are shown in Figures 4.1 and 4.2. As  $kh$  increases, the influence of depth decreases. By the time  $kh$  reaches 3,

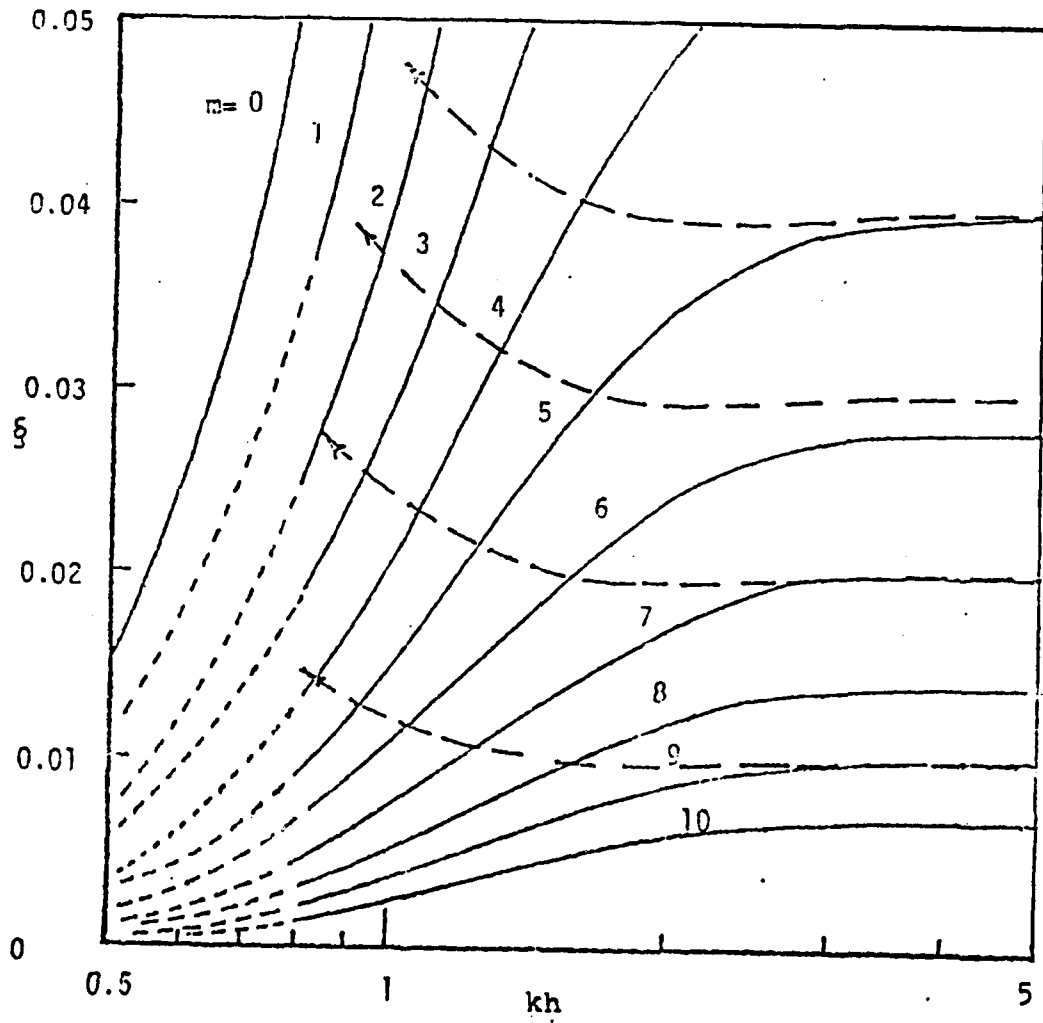


Fig. 4.1 Variation of  $m$  and  $\beta$  based on Stokes finite depth wave theory

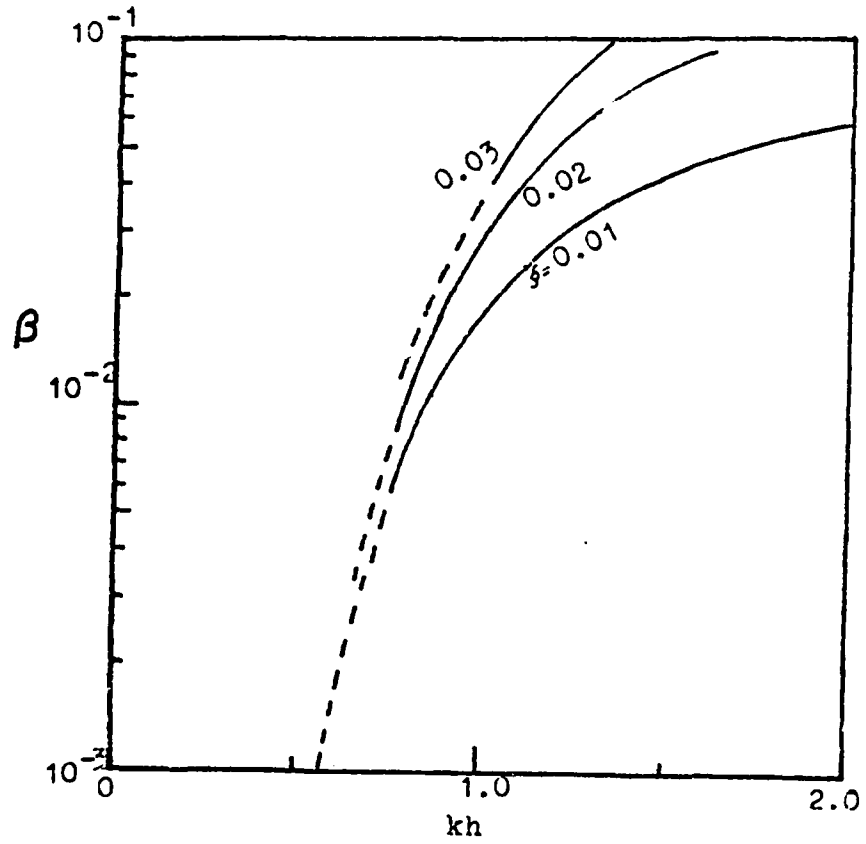


Fig. 4.2 Variation of  $\beta$  as a function of  $kh$  and  $\zeta$

both  $m$  and  $\beta$  essentially assume their deep water values as given in Huang et al. (1981).

Note that as wave travels from deep water to intermediate depth, evolution occurs. The dotted lines on Fig. 4.1 shows the change of  $\xi$  based on the energy flux conservation,

$$c_g E = \text{constant} \quad (4-9)$$

and

$$\xi = \tilde{\xi} / [\tanh^3 kh (1 + 2kh/\sinh 2kh)]^{1/2} \quad (4-10)$$

where  $\tilde{\xi}$  denotes the deep water value of  $\xi$ , and  $c_g$  is the group velocity.

According to Stokes expansion, the slope can become 0 or even negative, indicating that the amplitude of the second harmonic is higher than the primary, and the Stokes expansion becomes invalid. In fact, long before  $m$  reaches zero, the approximation of the Stokes expansion would deteriorate beyond acceptable limits. The gradual breakdown of the Stokes expansion in shallow water is also reflected in the  $\beta$  values shown in Fig.

4.2. Since  $\beta$  is derived from the condition of correct total energy content, a finite integrated value of the whole spectrum is necessary. As the  $m$  value decreases below 1, however, the Gamma-function in the  $\beta$  expression has logarithmic singularities. Consequently, the lower bound for the applicability of the Wallops spectrum will have to be  $m > 1$ . An alternative approach to avoid the singularities is to define a multi-slope spectral model with a matching frequency at a few times of the primary frequency. The determination of this matching frequency need more comparison of experimental data. In any case, as  $kh$  decreases to about unity, we need to use other wave models for modification.

#### Cnoidal and Solitary Waves

As the waves propagate into shallower water ( $kh < 1$ ) the Stokes expansions eventually break down. This can be seen in the growth of the harmonic component relative to the primary waves as shown by Flick et al. (1981). In shallow water, the cnoidal wave offers a much more satisfactory representation of the waves. The cnoidal wave model was developed by Korteweg and DeVries (1895). At the limits, the cnoidal wave approaches the

solitary wave for  $kh \ll 1$ , and sinusoidal wave for  $kh \gg 1$ , which is not exactly (but very close to) the Stokes wave.

The surface elevation of the water according to the cnoidal wave is

$$\eta = H \left\{ \frac{\eta_{\min}}{H} + \text{cn}^2[\Theta(\mu), \mu] \right\} \quad (4-11)$$

where  $H$  is the trough-to-crest height,  $\eta_{\min}$  is the depth of the water measured to the trough, and  $\text{cn}[\Theta(\mu), \mu]$  is the Jacobian elliptic function with the phase function,

$$\Theta(\mu) = [K(\mu)/\mu]k(x-ct) \quad (4-12)$$

and the cnoidal parameter  $\mu$ ,

$$\mu [K(\mu)]^2 = (3\pi^2/4) (H/k^2 h^3) \quad (4-13)$$

The water depth to the trough,  $\eta_{\min}$  is

$$\frac{\eta_{\min}}{H} = [1 - E(\mu)/K(\mu)]/\mu - 1 \quad (4-14)$$

where  $E(\mu)$  and  $K(\mu)$  are the complete elliptic integrals of the first and second kind respectively.

For the limiting case of  $\mu \rightarrow 1$ ,  $K(\mu) \rightarrow \infty$ , then

$$\text{cn}^2[\theta(\mu), \mu] = \text{sech}^2[(3H/4h^3)^{1/2} (x-ct)] \quad (4-15)$$

and  $\eta_{\min} \rightarrow h$ , so that the surface profile becomes

$$\eta = h + H \text{sech}^2 [(3H/4h^3)^{1/2} (x-ct)] \quad (4-16)$$

which is the solitary wave solution. The limiting processes adopted here is very critical near the point  $\mu=1$ . For example, if  $\mu=0.9999$ ,  $K(\mu) \approx 6.0$ . Therefore, for practical application, a wave number can be introduced to make the wave profile of finite wave length. Eq. (4-15) becomes

$$\eta = h + H \text{sech}^2 [(3H/4k^2h^3)^{1/2} k(x-ct)] \quad (4-17)$$

Both cnoidal and solitary wave profiles are controlled by a single parameter, the Ursell number, i.e.,

$$\text{Ur}' = H/(k^2h^3) \quad (4-18)$$

The Fourier expansions of the profiles are

$$a_n/H = \left(\frac{8}{3Ur'}\right) n q^n / (1 - q^{2n}) \quad (4-19)$$

for the cnoidal wave as given by Cayley (1895); and

$$a_n/H = \left(\frac{4n}{3Ur'}\right) / \sinh[n\pi / (3Ur')^{1/2}] \quad (4-20)$$

for the solitary waves as given by Gradshteyn and Ryzhik (1980). The quantity  $q$  in Eq. (4-19) is defined as

$$q = \exp[-\pi K(1-\mu)/K(\mu)] \quad (4-21)$$

With these equations, we can proceed to develop the Wallops spectral model in shallow water using either cnoidal or solitary wave as the basic components that make up the wave field.

For solitary wave case, the slope of the high frequency range of the spectrum is

$$m_3 = 2 \log(a_1/a_2) / \log 2 = 2 \log \cosh M / \log 2 \quad (4-22)$$

with

$$M = \pi / (3Ur')^{1/2} \quad (4-23)$$

For the cnoidal wave, the spectral slope is

$$m_c = 2 \log[(1+q^2)/2q] / \log 2 \quad (4-24)$$

For both these cases, the  $\beta$  coefficient is given by the general expression

$$\beta = \frac{(2\pi\xi)^2}{4 \frac{m-5}{2}} \frac{m \frac{m-1}{2}}{\Gamma(\frac{m-1}{2})} \frac{c^4 k^2}{g^2} \quad (4-25)$$

where  $c$  is the phase velocity and  $m$  is the spectral slope for each case. For most studies, the phase velocity of the Stokes wave,

$$c^2 = (g/k) \tanh kh \quad (4-26)$$

will give a highly accurate answer as pointed out by Bona et al. (1981). With this expression, the parameter given in Eq. (4-5) could be used for both the cnoidal and the solitary waves provided the proper  $m$  values as given in (4-22) and (4-24) were used.

For practical applications, it is more convenient to use the RMS variance as the wave height scale (especially for field data). The new Ursell number

becomes

$$Ur = \bar{\eta}^2 / (k^2 h^3) = Ur' \bar{\eta}'^2 / H \quad (4-27)$$

where  $\bar{\eta}'^2$  is the RMS elevation with respect to the mean water level. For a sinusoidal wave train, the mean is zero, hence

$$\bar{\eta}'^2 = H / (2\sqrt{2}) \quad (4-28)$$

For the solitary waves, the mean water level is

$$\eta' = h + \frac{H}{\pi(\frac{3}{4}Ur')^2} \tanh [\pi(3Ur'/4)] \quad (4-29)$$

and

$$\begin{aligned} \frac{\bar{\eta}'^2}{H} &= [(\bar{\eta} - \eta')^2]^{1/2} \\ &= \left\{ \frac{\tanh Q}{8} \left( 1 - \frac{1}{3} \tanh^2 Q - \frac{\tanh Q}{Q} \right) \right\}^{1/2} \quad (4-30) \end{aligned}$$

where  $Q = \pi(3Ur'/4)^{1/2}$ , and  $\eta'$  = mean elevation.

The value of (4-30) is given in Fig. 4.3. The special significance of this quantity is that it represents the

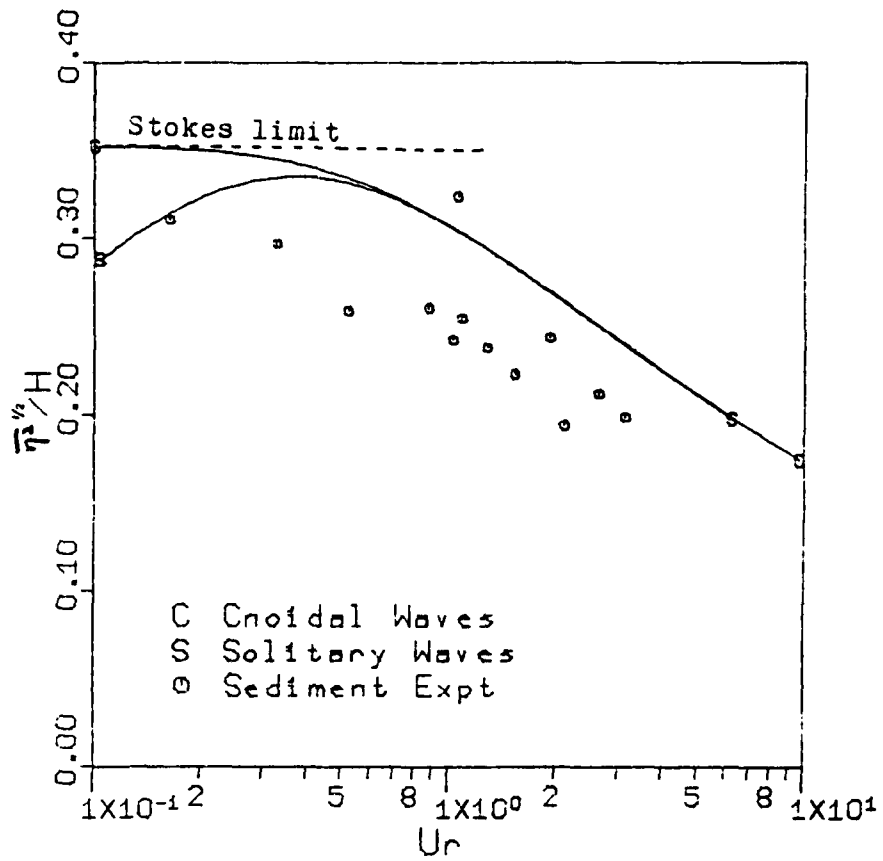


Fig. 4.3 RMS variance of cnoidal and solitary waves vs.  $U_r$

ratio of  $Ur'/Ur$ , Eq. (4-27). Since most data are expressed in terms of  $Ur$ , Eq. (4-30) provided the link between observations and the model results. The corresponding values for the cnoidal waves are

$$\eta' = H \{ 1 - [1 - E(u)/K(u)]/u \} \quad (4-31)$$

and

$$\frac{\bar{\eta}^{1/2}}{H} = \left\{ \frac{1}{3u} \left[ (1-u) - (2-4u)\eta' \right] - \eta'^2 \right\} \quad (4-32)$$

The value of Eq. (4-32) is plotted on Fig. 4.3 also.

#### Stream Function Wave Theory

Stream function wave theory developed by Dean (1965) was based on nonlinear least square fitting of the governing equation and the boundary conditions of a wave field. The solution is in the form of

$$\psi(x, z) = zL/T + \sum_{n=1}^{NM} X(n) \sinh\left[\frac{2\pi n}{L}(h+z)\right] \cos\left(\frac{2\pi n}{L}x\right) \quad (4-33)$$

and

$$\eta = T \psi_n / L - T/L \sum_{n=1}^{\infty} X(n) \sinh\left[\frac{2\pi n}{L}(h+\eta)\right] \cos\left(\frac{2\pi n}{L}x\right)$$

(4-34)

The solution of Eqs. (4-33) and (4-34) satisfy the governing Laplace equation and bottom and free surface kinematic conditions.  $L$  and  $X(n)$  are numerically calculated to best fit the dynamic free surface condition. The detailed treatment is presented in Dean (1965, 1974). Using the procedure, by specifying the wave period, water depth and wave height, the surface elevation can be obtained. Applying Fourier decomposition, the spectrum of each wave can be obtained, which will be termed "stream function spectrum". The corresponding Wollops  $m$  and  $n$  can be calculated from the first and second harmonic values and the variance of the elevation record. For practical applications, computation on a high speed digital computer is necessary.

#### 4.4 Velocity Spectra

For engineering applications such as wave force analysis for marine structures, sediment transport mechanisms and nearshore circulation, the ability of correctly predict the velocity field is important. The velocity field under a nonlinear wave field is a complex one. This section only presents the horizontal and vertical velocity spectra measured in the sediment experiment. Comparison of the measurement with the linear transformation from wave spectra and the stream function velocity spectra are discussed.

Based on the linear wave theory, the velocity spectral transformation can be expressed as,

$$S_u(\sigma) = [\sigma \cosh k(h+z) / \sinh kh]^2 S_e(\sigma) \quad (4-35)$$

and

$$S_w(\sigma) = [\sigma \sinh k(h+z) / \sinh kh]^2 S_e(\sigma) \quad (4-36)$$

where  $S_u$ ,  $S_w$  and  $S_e$  are the spectra of the horizontal velocity, the vertical velocity and the wave surface elevation, respectively. On the other hand, the velocities based on stream function wave theory can be

written as

$$u = - \sum_{n=1}^{N} X(n) (2\pi n/L) \cosh[\frac{2\pi}{L} n(h+z)] \cos(\frac{2\pi n}{L} x) \quad (4-37)$$

and

$$w = \sum_{n=1}^{N} X(n) (2\pi n/L) \sinh[\frac{2\pi}{L} n(h+z)] \sin(\frac{2\pi n}{L} x) \quad (438)$$

The  $u$  and  $w$  profiles can then be processed by Fourier decomposition to create the velocity spectra. The comparison with experimental data is shown in next section.

#### 4.5 Comparison with Observations

Having constructed the spectral models for intermediate and shallow water waves, they are tested against the observations. As a first step, the values of the spectral slope in the high frequency range is plotted as a function of  $Ur$  in Fig. 4.4. Since the Stokes wave depends on  $\xi$  and  $kh$  in a mutually unrelated way, the slope value should be represented by a family of curves each for a specific  $\xi$  value. For the present experiment data,  $\xi$  varies from 0.005 to 0.025, the corresponding

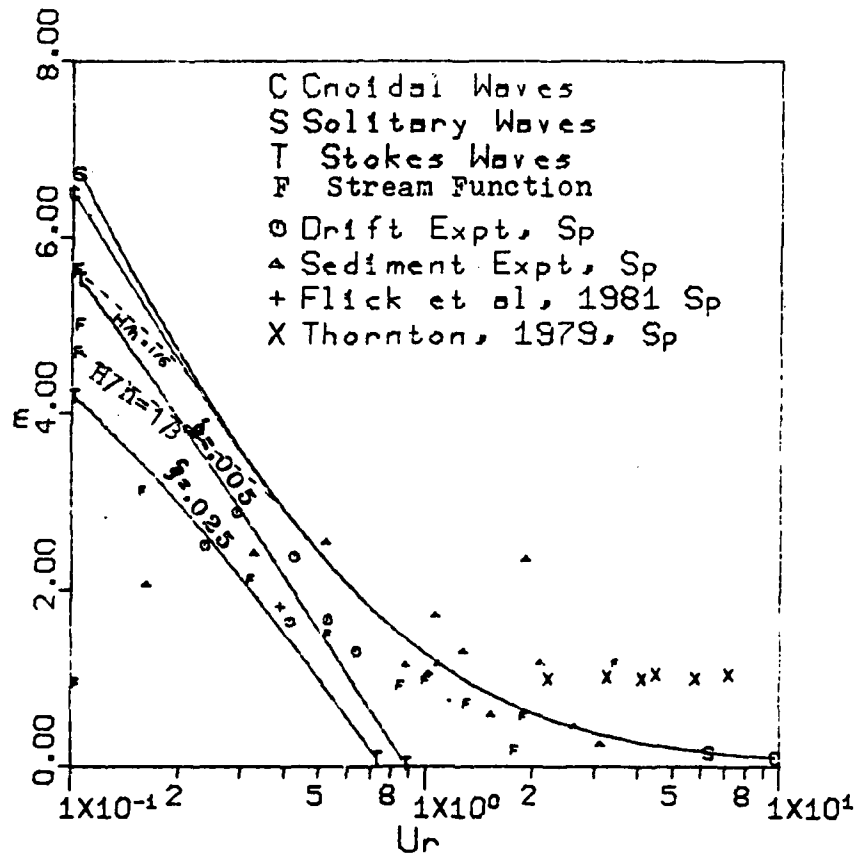


Fig. 4.4 Spectral slopes as a function of  $U_r$  (spilling breakers)

Stokes curves are shown. The numerical results of the stream function calculation also show nonunique relation on  $Ur$ . Since wave length is a variable to be determined in the stream function calculation, the family of curves are plotted with different  $H/h$  ratios. The numerical procedure also applied to each individual cases of the sediment experiment (Chapter 3) and plotted with symbol "F". Wave data from the drift experiment (Chapter 2), Flick et al.'s shoaling experiment (1981) and Thornton's field experiment (1979) were also analyzed. Thornton's data is in spectral form; the spectral slopes near the energy containing part are used. It is seen that for  $Ur > 0.3$ , cnoidal and solitary results are nearly identical and show reasonable agreement with the data for  $Ur > 1$ . As  $Ur$  decreases (deeper water), they started deviating from the experimental results. In this intermediate depth range, Stokes result shows better agreement. Only stream function shows good agreement for the whole  $Ur$  range tested.

The full spectra of surface elevation for the sediment experiment are shown in the top plots of Fig. 4.5. For clarity, only the Wallops spectra based on cnoidal theory and stream function curves are plotted

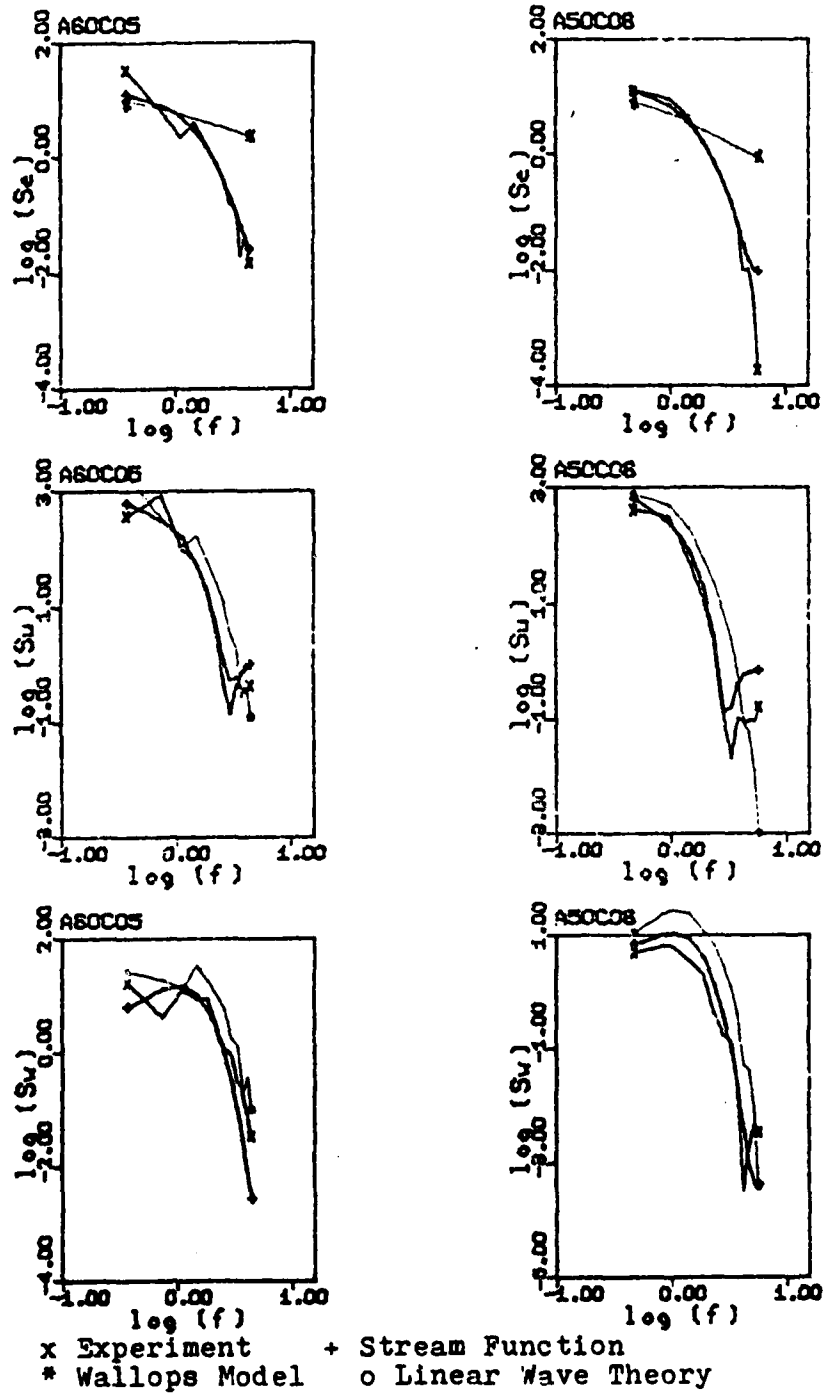


Fig. 4.5 Comparison of  $\eta$ ,  $u$  and  $w$  spectra with various theories

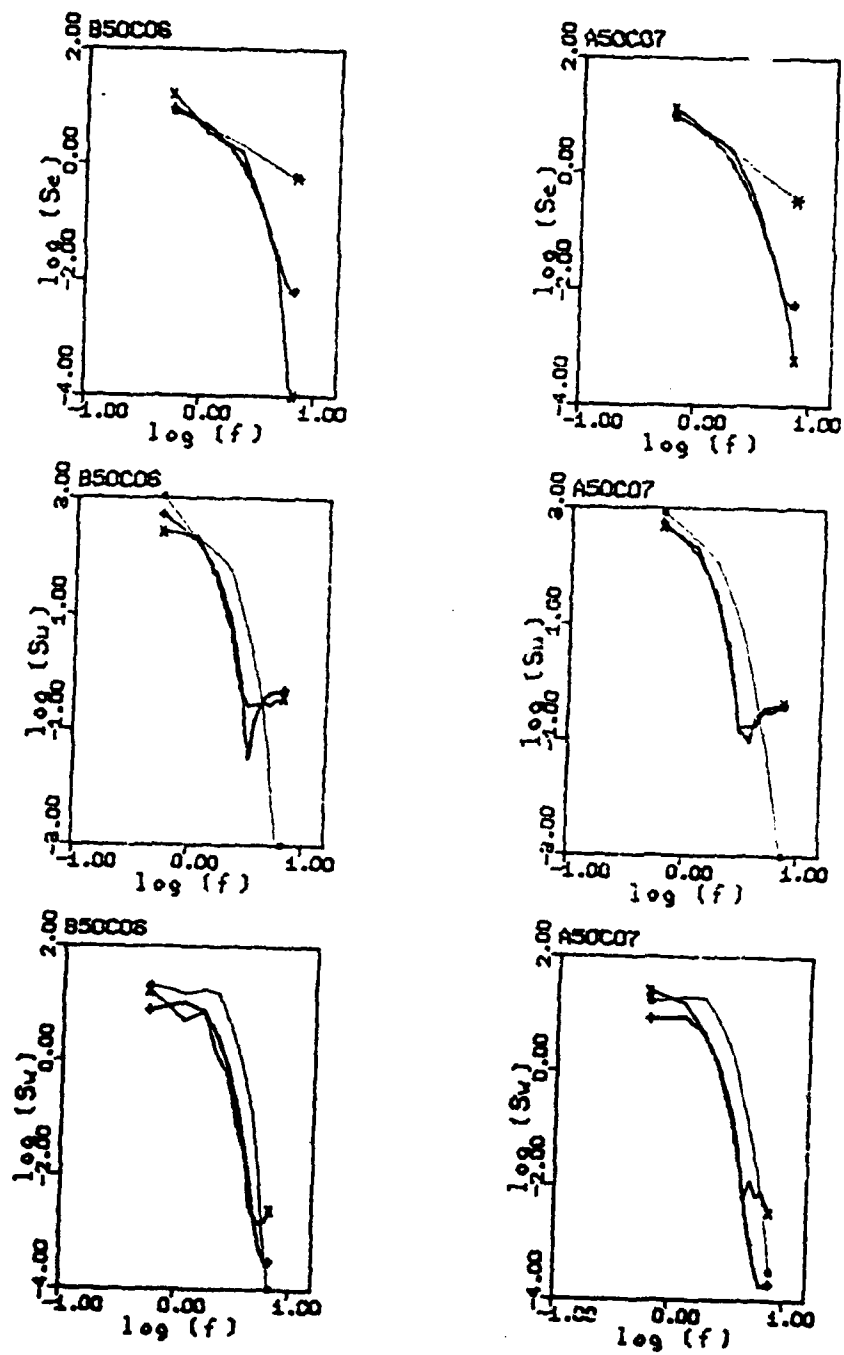


Fig. 4.5 (continued)

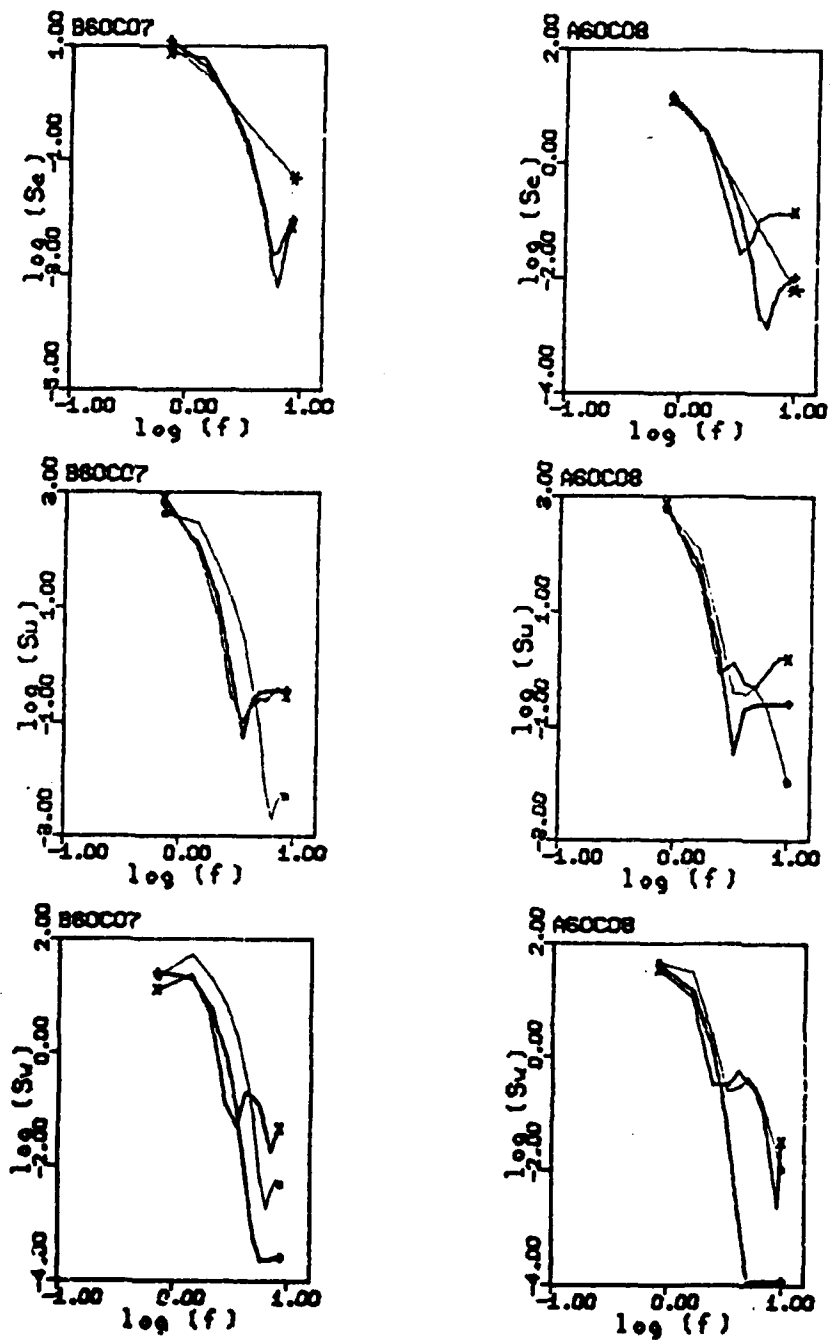


Fig. 4.5 (continued)

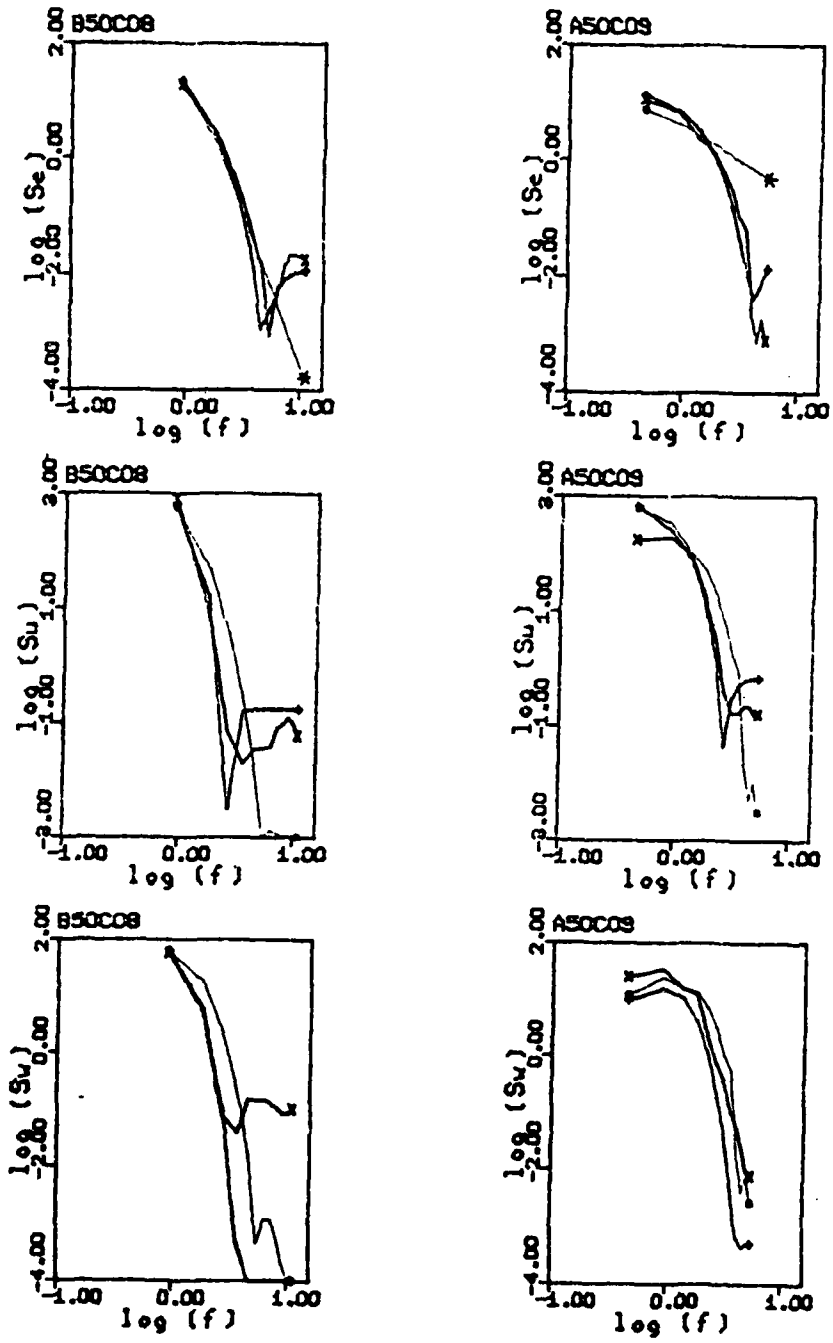


Fig. 4.5 (continued)

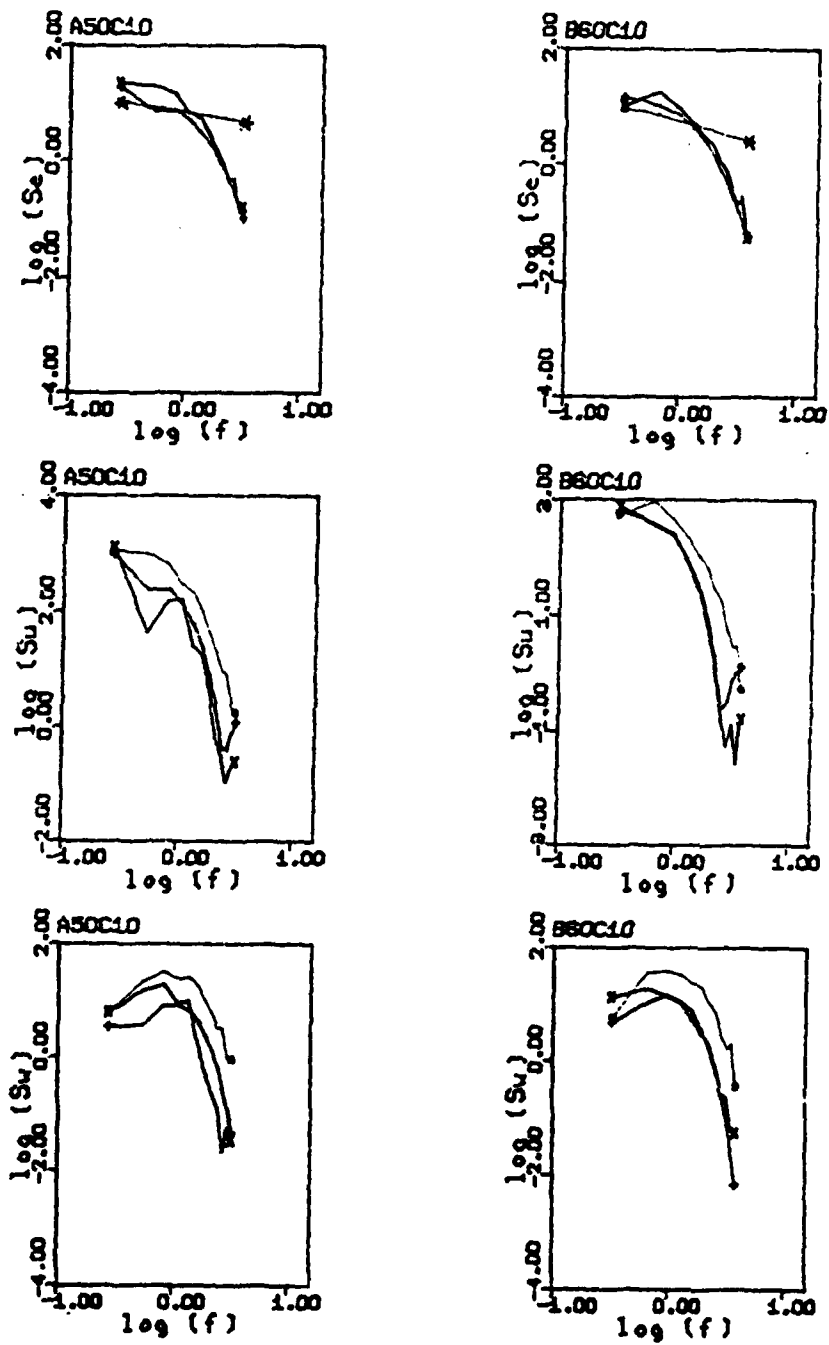


Fig. 4.5 (continued)

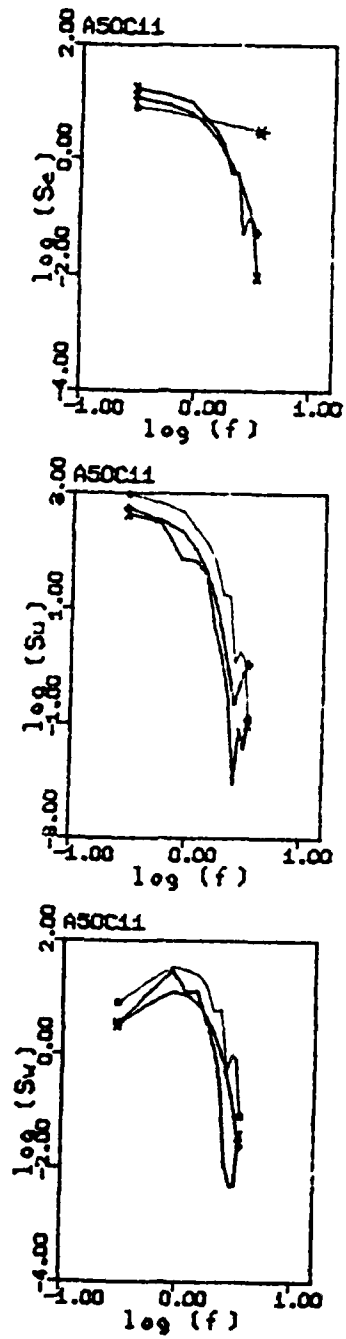


Fig. 4.5 (continued)

along with the experimental results. In these plots, only the spectral peak values are shown. The agreement over the higher energy components is generally good for the Wallops model, but for the full range of frequency, direct calculation of the stream function wave form shows far better agreement. It is noted that the spectra based on the cnoidal and solitary theories will predict a much steeper spectrum beyond the second or the third harmonic as implied in Fig. 4.6. The figure compares the theoretical amplitude harmonics with those of the measured wave profiles. It is obvious that after the second harmonic, the theories underestimate the harmonics and therefore, the spectral components. The middle plots in Fig. 4.5 are the horizontal velocity spectra at the elevation of  $z/h = -0.6$  to  $-0.7$ . Better representation of the stream function calculation over the linear transformation is obvious. The bottom plots are the vertical velocity spectra at the same depth. Stream function calculation, again, shows very good agreement.

Fig. 4.7 plots the variance ratios of the wave and velocity spectra based on the stream function calculations and the linear transformation. For the wave spectra (plot a), the mean value of the ratios of the

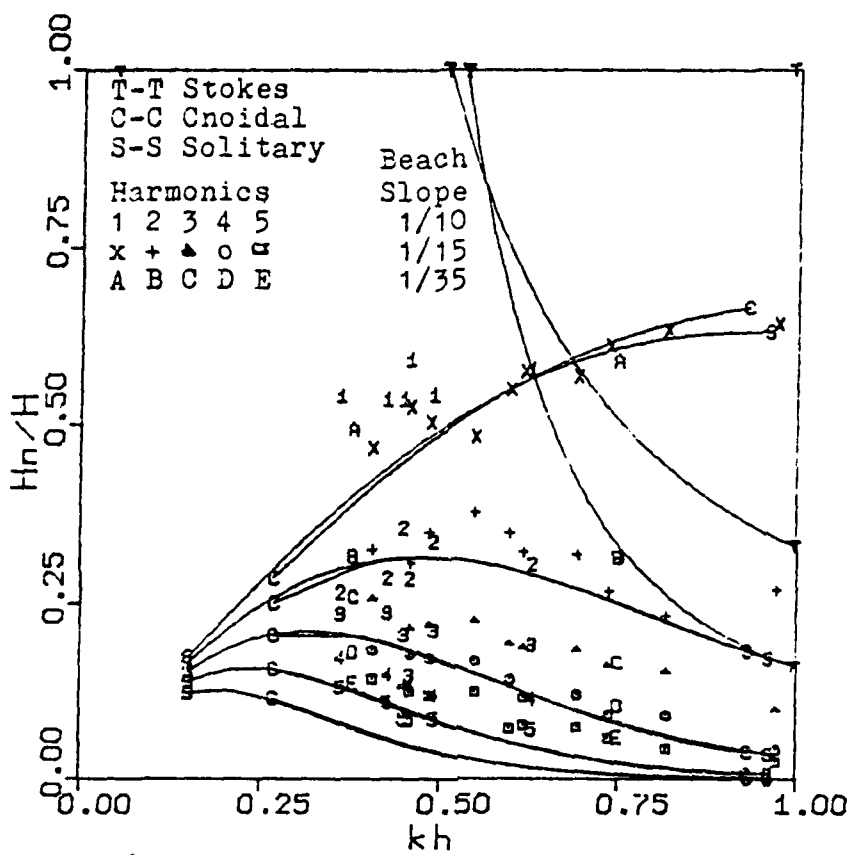


Fig. 4.6 Harmonic amplitudes Vs. kh

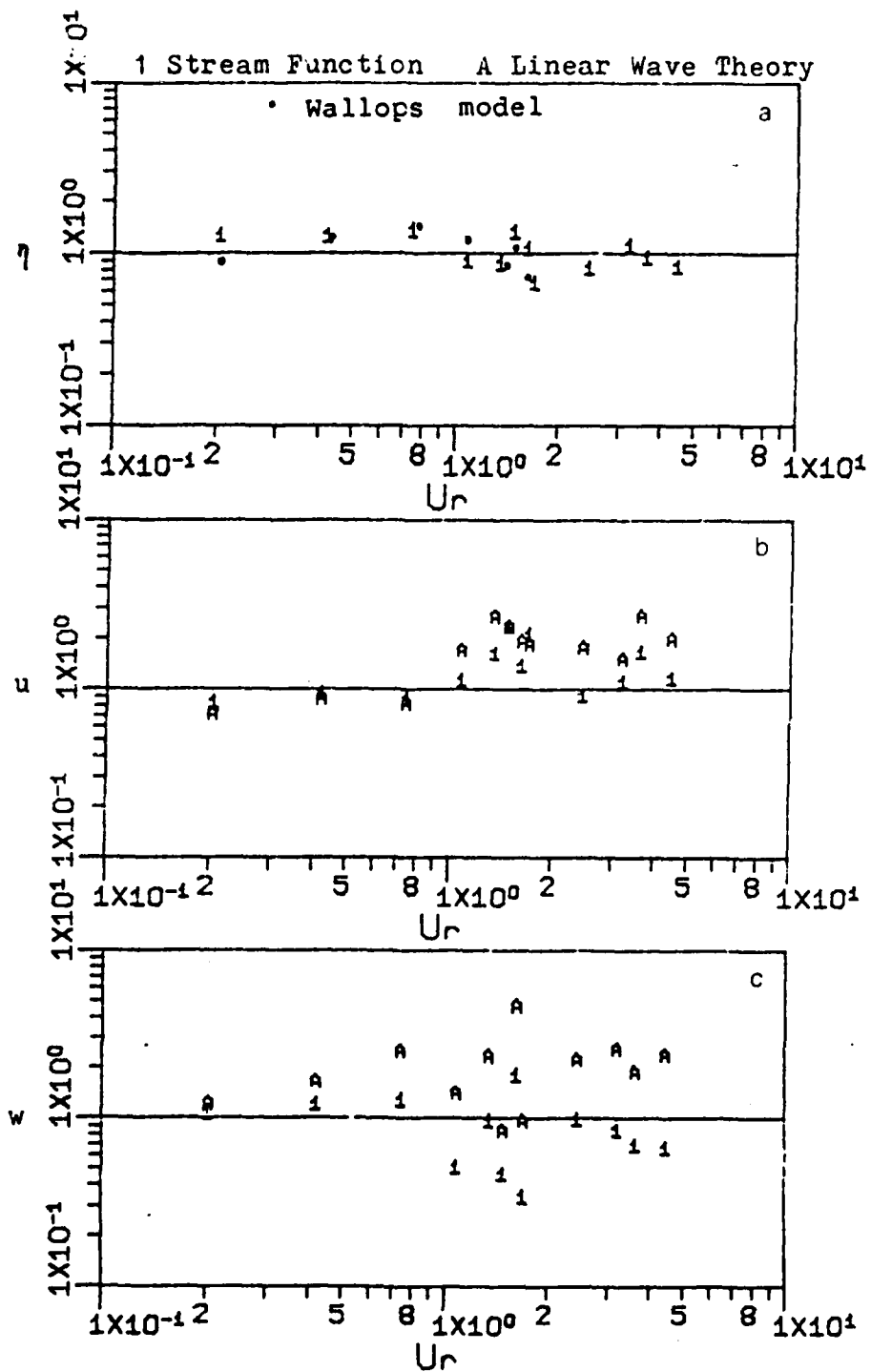


Fig. 4.7 Comparison of linear and stream function wave theories: total variance

stream function calculated variances to those of the measurements is 0.95 with standard deviation of 0.37. The variance of the Wallops model for  $m > 1$  are also plotted on the same figure. The ratio mean and deviation are 0.92 and 0.46, respectively. The Wallops spectral model seems to represent the total energy adequately. Similar plots for the horizontal and the vertical velocity spectra are given in Fig. 4.7 b and c, respectively.

For the horizontal velocity spectral variance (plot b), linear transformation performed reasonably well in deeper water ( $Ur < 1$ ) but has a tendency of over-prediction as water becomes shallower. The stream function calculation remains good and stable for the range tested. There are some cases with Ursell number between 1.3 to 2.0 show large deviation. Although the definite reasons are uncertain, one possible explanation is the reflection effects. If the measuring location happens to be at a quasi-antinodal point, the horizontal velocity will decrease due to the standing wave contribution at the antinode (thus a higher theory to measurement ratio). This is partially revealed by the  $\eta$  and  $w$  variance ratios, most of which are less than unity

in that  $Ur$  range. More extensive studies are necessary to clarify this point. The ratio mean and deviation are 1.12 and 0.51 for stream function theory, and 1.53 and 0.78 for linear transformation.

Comparison of the vertical velocity variance ratios (plot c) is similar to the horizontal one except that the vertical ratios are more scattered. Since the magnitude of the vertical velocity is smaller than that of the horizontal velocity, any factors contributed to the deviation such as turbulence or the instrument noise will show a more prominent effect on the vertical velocity. The ratio mean and deviation are 0.84 and 0.48 for the stream function calculations, and 1.91 and 1.20 for linear transformation.

In summary, the Wallops spectral model can be modified for finite depth application. The model will give accurate energy content and good agreement in the vicinity of the primary peaks where energy are concentrated. The applicability of Stokes' modification is about  $kh > 0.75$ . For shallower water cases, the cnoidal or solitary theory is more appropriate. For  $m < 1$ , the Wallops model predicted an infinite energy content. Truncated spectrum or multi-slope model need to be

considered.

An alternative to the spectral model is to calculate the spectra from the wave profiles generated by the stream function wave theory. From the test cases presented, it is found that the wave and velocity spectra of the stream function generated waves show excellent agreement with the measurements.

## CHAPTER 5 CONCLUSION AND RECOMMENDATIONS

Flow properties including both mean and instantaneous velocities as well as sediment suspension processes at the breaking zone were studied in the laboratory. Analysis were performed in the characteristics of the mean drift velocity and the spectral presentations of the fluctuating components of water surface elevation and flow velocities. The mechanics of sediment suspension under the influence of wave motion is critically examined.

Drift velocity profile at breaking point shows an onshore motion near the surface and close to the bottom. In the middle colume, the flow is always offshore. The magnitude of the current is more uniform than those occur under nonbreaking waves. The shapes of the profiles under plunging and speilling waves are similar. Comparison of the vertically averaged return flow velocity with four drift velocity theories was conducted.

Reasonable agreement was obtained.

Nonlinear effect of breaking caused harmonic generation of the monochromatic incident waves. The wave form was analyzed by spectral analysis. Comparison with the nonlinear stream function wave theory shows good agreement both in terms of the individual spectrum and the total variance calculation. The difference is generally under 15 percent. The Wallops spectral model modified for finite water application was proposed. The model gives correct variance estimate and emphasizes the simulation of the higher energy containing harmonics. The instantaneous velocity measurement was compared with the stream function wave theory, the difference is generally under 20 percent.

The sediment suspension can be represented by a turbulent diffusion model. The diffusivity is related to the wave parameters, with wave height as the length scale and the vertical velocity as the velocity scale for high agitation condition. For low agitation, the local vertical excursion amplitude is the proper length scale. Fall velocity reduction in an oscillating flow field and the bottom sediment grading effects were also included in the model. The model gives good agreement both in the

concentration profile and the magnitude.

For future studies of this problem, the author suggests the following directions,

1. Instrumentation: The instruments for sediment concentration measurement and velocity measurement should be improved. The frequency response should be in the same range for all the devices. The sensing volume of the velocity meter need to be kept small to increase the depth resolution. To reduce the intermittency of the concentration data, larger sensing volume to enhance chance of particles passing through is necessary. The tradeoff of the signal quality and the frequency response need careful studies.

2. Tracing of neutrally buoyant particles to obtain Lagrangian drift is subjected to the processor's judgement and introduces error. Other procedure to reduce human interpretation is desired for a more accurate measurement.

4. Different concepts on suspension mechanisms that emphasize the vortex trapping has been offered recently

(Nielsen, 1981; Tooby et al, 1977). Longuet-Higgins (1980) offered a numerical model of vortex formation and shedding. It is always useful to have a different perspective to one problem. The result may enhance our knowledge

5. Wave theories considering the slope effects had not been included in this preliminary study. For a more refined model, the slope effects need to be included.

REFERENCES:

Abramowitz, M. and I. A. Stegun, 1965, Handbook of Mathematical Functions with Formulas, Graphs and Mathematical Tables, Dover.

Bashikirov, G. S., 1961, Coastal Dynamics, Moscow Press (in Russian).

Battjes, J. A., 1974, Surf similarity, Proc. Coast. Eng. Conf., Chap. 26.

Bhattacharya, P., 1971, Sediment suspension in shoaling waves, Ph.D. dissertation, The University of Iowa, Hydraulic Engineering.

Bijker, E. W., J. P. Th. Kalkwijk and T. Pieter, 1974, Mass transport in gravity waves on a sloping bottom, Proc. Coast. Eng. Conf., Chap. 25.

Bona, J. L., W. G. Pritchard, and L. R. Scott, 1981, An evaluation of a model equation for water waves, Phil. Trans. Roy. Soc., A 302, 457-510.

Bowden, K. F., 1948, some observation of wave and other fluctuations in a tidal current, Proc. Roy. Soc., A192, 403-425.

Cayley, A. 1895, An Elementary Treatise on Elliptic Functions, George Bell and Sons, London.

Dally, W. R., 1980, A Numerical Model for Beach Profile Evolution, Master's Thesis, Dept. of Civil Engineering, University of Delaware.

Dalrymple, R. A., 1976, Wave-induced mass transport in water waves, J. WW, ASCE, 102(WW2), 255-264.

Dalrymple, R. A., 1974, A finite amplitude wave on a linear shear current, J. Geoph. Res., 79(30), 4498-4504.

Dalrymple, R. A., 1973, Water wave models and wave

forces with shear currents, Coastal and Oceanographic Engineering Lab, Tech. Rep. no. 20, University of Florida, Gainesville, Florida.

De, S. C., 1955, Contributions to the theory of Stokes waves, Proc. Camb. Phil. Soc., 51, 713-736.

Dean, R. G., 1974, Evaluation and development of water wave theories for engineering application, CERC Special Rep. no. 1.

Dean, R. G., 1965, Stream function representation of nonlinear ocean waves, J. Geoph. Res., 70(18), 4561-4572.

Einstein, H. A., 1950, The bed-load function for sediment transportation in open channel flows, Dept. of Agriculture, Tech. Bull. No. 20.

Fairchild, J. C., 1973, Longshore transport of suspended sediment, CERC Reprint No. 14-73.

Flick, R. E., R. T. Guza and D. L. Inman, 1981, Elevation and velocity measurements of laboratory shoaling waves, J. Geoph. Res., 86(C5), 4149-4160.

Galvin, C. J., 1968, Breaker type classification on three lab beaches, J. Geoph. Res., 73(12), 3651-3659.

Glover, J. R., 1977, An improved Iowa Sediment Concentration Analyzer, IIHR Rep. no. 209, Iowa Institute of Hydraulic Research, University of Iowa, Iowa City, Iowa.

Gradshteyn, I. S. and I. M. Ryzhik, 1980, Table of Integrals, Series and Products, Academic Press.

Graf, W. H., 1971, Hydraulics of Sediment Transport, McGraw-Hill Book Co.

Guza, R. T. and A. J. Bowen, 1976, Resonant interactions for waves breaking on a beach, Proc. Coast. Eng. Conf., Chap. 32.

Hattori, M., 1969, The mechanics of suspended sediments due to standing waves, Coastal Engineering in Japan, 12, 69-81.

Ho, H. W., 1964, Fall velocity of a sphere in a field of oscillating fluid, Ph.D. dissertation, State University of Iowa, Hydraulic Engineering.

Hom-ma, M. and K. Horikawa, 1962, Suspended sediment due to wave action, Proc. 8th Conf. on Coast. Eng., 168-193.

Hom-ma, M., K. Horikawa and R. Kajima, 1965, A study of suspended sediment due to wave action, Coast. Eng. in Japan, 8.

Horikawa, K., 1978, Coastal Engineering, An Introduction to Ocean Engineering, Univ. of Tokyo Press.

Horikawa, K. and A. Watanabe, 1968, Laboratory study on oscillating boundary layer flow, Proc. of 10th Cong. of IAHR, London.

Horikawa, K. and A. Watanabe, 1970, Turbulence and sediment concentration due to waves, Coastal Eng. in Japan, 13, 15-24.

Huang, N. E., S. R. Long, C.-C. Tung, Y. Yuen and L. F. Bliven, 1981, A unified two-parameter wave spectral model for a general sea state, J. Fluid Mech., 112, 203-224.

Huang, N. E., 1970, Mass transport induced by wave motion, J. Marine Res., 28(1), 35-50.

Jonsson, I. G., 1966, Wave boundary layer and friction factors, Proc. 10th Conf. of Coast. Eng., Ch. 10.

Jonsson, I. G. and N. A. Carlson, 1976, Experimental and theoretical investigation in an oscillating (rough) turbulent boundary layer, J. Hyd. Res., 14(1), 45-60.

Kajiura, K., 1968, A model of bottom boundary layer in water waves, Bull. Earthquake Res. Inst., U. Tokyo, 46, 75-123.

Kana, T. W. and L. G. Ward, 1980, Nearshore suspended sediment load during storm and post-storm conditions, Proc. 17th Conf. of Coast. Eng., 1158-1174.

Kana, T. W., 1978, Surf zone measurements of suspended

sediment, Proc. 16th Coast. Eng. Conf., 1725-43.

Kana, T. W., 1976, A new apparatus for collecting simultaneous water samples in the surf zone, J. Sedimentary Petrology, 46(4), 1031-34.

Kennedy, J. F. and F. A. Locher, 1972, Sediment suspension by water waves, in Waves on Beach and Resulting Sediment Transport, ed. R. E. Meyer, Academic Press.

Kitaigorodskii, S. A., V. P. Krasitskii and M. M. Zaslavskii, 1975, On Phillips theory of equilibrium range in the spectra of wind-generated waves, J. Phys. Oceano., 5, 410-420.

Lee, R. S., 1981, Fall velocity of sediment particles under wave action, Master's Thesis, Tien-Jin University (in Chinese).

Locher, F. A., J. R. Glover and T. Nakato, 1974, Investigation of the operating characteristics of the Iowa Sediment Concentration Measurement System, IIHR Rep. no. 170, University of Iowa.

Longuet-Higgins, M. S., 1981, Oscillating flow over steep sand ripples, J. Fluid Mech., 107, 1-35.

Longuet-Higgins, M. S., 1980, The unsolved problems of breaking waves, Proc. 18th Coast. Eng. Conf., 1-28.

Longuet-Higgins, M. S., 1976, Recent development in the studies of breaking waves, Proc. 15th Coast. Eng. Conf., 441-460.

Longuet-Higgins, M. S., 1953, Mass transport in water waves, Phil. Tran. Roy. Soc. Lond., A245, 535-581.

Mei, C. C., P. L.-F. Liu and T. G. Carter, 1972, Mass transport in water waves, Rep. no. 146, Dept. of Civil Engineering, MIT.

Murray, S. P., 1970, Settling velocity and vertical diffusion of particles in turbulent water, J. Geop. Res., 75(9), 1647-1654.

Nakato, T., F. A. Locher, J. R. Glover and J. F.

Kennedy, 1977, Wave entrainment of sediment from ripple beds, ASCE, 103(WW1), 83-100.

Nielsen, P., 1979, Some basic concepts of wave sediment transport, Ser. Pap. No. 20, Tech. Univ. of Denmark.

Nielsen, P. and M. O. Green, 1981, Suspended sediment under waves, (sub. to ASCE (WV)).

Phillips, O. M., 1958, The equilibrium range in the spectrum of wind-generated waves, J. Fluid Mech., 4, 426-434.

Pierson, W. J. and L. Moskowitz, 1964, A proposed spectral form for fully developed wind sea based on the similarity theory of S. A. Kitaigorodskii, J. Geophys. Res., 69, 5181-5190.

Raudkivi, A. J., 1976, Loose Boundary Hydraulics, 2nd ed., Pergamon Press.

Russel, R. C. H. and J. D. C. Osorio, 1958, An experimental investigation of drift profile in a closed channel, Proc. Coast. Eng. Conf., Chap. 10.

Schlichting, H., 1968, Boundary Layer Theories, 6th. ed., McGraw-Hill Book Co.

Shinohara, K. Y., Y. Tsubaki, Y. Yoshtaka and G. Agimori, 1958, Sand transport along a model sandy beach by wave action, Coast. Eng. in Japan, 1, 111-130.

Stokes, G. G., 1847, On the theory of oscillatory waves, Trans. Camb. Phil. Soc., 8, 197-220.

Stokes, G. G., 1880, Supplement to a paper on the theory of oscillatory waves, Math. and Phys. Papers, 1, 314-326.

Sunamura, T., D. Yang and H. Wang, 1980, Laboratory drift-velocity distribution at wave breaking point with some implications to sediment transport processes, Ocean Eng. Tech. Rep. no. 22, Dept. of Civil Eng., University of Delaware.

Svendsen, I. A., 1974, Cnoidal waves over a gently sloping bottom, Ser, pap. no. 6, Inst. of Hydrod. and

Hydau. Eng., Tech. Univ. of Dnmark.

Svendsen, I. A. and I. G. Jonsson, 1976, Hydrodynamics of Coastal Regions, Tech. University of Denmark, Lyngby, Denmark.

Tanaka, N., 1975, Vertical distribution of suspended sand concentration in the surf zone, 22nd Proc. Nat. Conf. Coastal Eng., pp. 319-324 (in Japanese).

Thornton, F. B., 1979, Energetics of breaking waves within the surf zone, J. Geoph. Res., 84(C8), 4931-4938.

Thornton, F. B., 1977, Rederivation of the saturation range in the frequency spectrum of wind generated gravity waves, J. Phys. Oceano., 7(1), 137-140.

Tooby, P. F., G. L. Wick and J. D. Issacs, 1977, The motion of a small sphere in a rotating velocity field: a possible mechanism for suspending particles in turbulence, J. Geophys. Res., 82(15), 2096-2100.

Wang, H., H. D. Hans and Y.-H. Chen, 1980, Nearshore data from North Sea during MARSEN I, September-December, 1979, Ocean Eng. Rep. no. 24, Civil Eng. Dept., U. of Delaware.

Wang, H. and S. S. Liang, 1975, Mechanics of suspended sediment in random waves, J. Geoph. Res., 80(24), 3488-3494.

Wang, H., T. Sunamura and P. A. Hwang, 1982, Drift-velocity at the wave breaking point, Coast Engineering, 6(2).

Wang, H. and W.-C. Yang, 1981, Wave spectral transformation measurements at Sylt, North Sea, Coastal Engineering, 5, 1-34.

Wang, H. and W.-C. Yang, 1980, A similarity model in the surf zone, Proc. 18th Coast. Eng. Conf.

Wang, S.-Y., 1981, Law of distribution of sediment concentration along the water depth under wave action, unpublished notes.

Watts, G.M., 1953, Development and field tests of a sampler for suspended sediment in wave action, BEB Tech. Memo. 34.

Wehausen, J. V. and E. V. Laiton, 1960, Surface Waves, Handbuch der Physik, 4, 446-758, Springer.

Wiegel, R. L., 1964, Oceanographic Engineering, Prntice-Hall Inc.

Yalin, M. S., 1976, Mechanics of Sediment Transport, 2nd. ed., Pergamon Press.

Yang, W.-C., 1981, Surf zone properties and on/offshore sediment transport, Ph. D. Dissertation, Dept. of Civil Eng., University of Delaware.

Appendix Lagrangian Mass Transport by Stream  
Wave Theory

Dalrymple (1976) employed a Eulerian reference frame to evaluate wave mass transport using Dean's stream function wave theory (Dean, 1965, 1974). He also extended the theory to include the cases with the linear shear current superimposed on the wave field (Dalrymple, 1973, 1974). In this appendix, a method of evaluating Lagrangian drift velocity by following particle motion along a streamline is developed. The drift velocity profiles are similar to those of Stokes (1847). The total mass transport is the same as evaluated by Eulerian method, which serves as a check in the validity of the numerical scheme.

Theory

The mass transport, M is defined as

$$M = \rho/T \int_0^T \int_{h_1}^{\eta} u(z, t) dz dt \quad (I-1)$$

or changing the order of integration

$$M = \rho \int_{-h}^{\eta} \left[ \frac{1}{T} \int_0^T u(z', t) dt \right] dz' \quad (I-2)$$

where  $u(z', t)$  is the Lagrangian velocity following a particle. The bracketed term in Eq. (I-2) is known as the mass transport velocity or drift velocity,  $U$ . Dean's stream function theory states that the stream function of a wave field can be expressed as

$$\psi(x, z) = zL/T + \sum_{n=1}^{NN} X(n) \sinh\left[\frac{2\pi n}{L}(h+z)\right] \cos\left(\frac{2\pi n}{L}x\right) \quad (I-3)$$

where coordinate system moves with wave celerity to render steadiness of the wave motion. The particle velocity in the wave field can be written as

$$u(x, z) = -\sum_{n=1}^{NN} \frac{2\pi n}{L} X(n) \cosh\left[\frac{2\pi n}{L}(h+z)\right] \cos\left(\frac{2\pi n}{L}x\right) \quad (I-4)$$

The elevation  $z'$  of a particular streamline,  $\psi'$ , can be obtained by iteration from the following expression

$$z'(x) = T\psi'/L - T/L \sum_{n=1}^{NN} X(n) \sinh\left[\frac{2\pi n}{L}(h+z')\right] \cos\left(\frac{2\pi n}{L}x\right) \quad (I-5)$$

Using Eq. (I-4) to evaluate  $M$ , a transformation of

variable from  $t$  to  $x$  is necessary,

$$M = \frac{\rho}{T} \int_h^{\bar{\eta}} \int_0^T u(t, z') dt dz' = \frac{\rho}{L} \int_h^{\bar{\eta}} \int_0^L u(x, z') \frac{\partial(x, z')}{\partial(x, z)} dx dz' \quad (I-6)$$

The Jacobian  $J = \frac{\partial(x, z')}{\partial(x, z)}$  in Eq. (I-6) is  $J = \partial t / \partial x$ . In stream function theory, the coordinate system is moving with wave celerity,  $C$ . That is, at any wave phase  $\theta = x - Ct = \text{constant}$ . Therefore,  $J = 1/C$ . Eq. (I-6) becomes

$$M = \frac{\rho}{L} \int_h^{\bar{\eta}} \int_0^L u(x, z') / C dx dz' \quad (I-7)$$

Using this equation, however, we have to calculate  $u$  above water surface for the upper layers. This is physically wrong especially for nonlinear waves which have long troughs below mean water level. In the following paragraph, a different approach to evaluate  $M$  is presented. The mass transport velocity is calculated by following a streamline, therefore, particles always stay in the fluid region.

By using Eq. (I-5) to obtain the elevation,  $z'$ , of a streamline, particle velocity along the streamline can be calculated by

$$u(x, z') = \sum_{n=1}^{NN} X(n) \cosh\left[\frac{2\pi n}{L}[h+z']\right] \cos\left(\frac{2\pi n}{L}x\right) \quad (I-8)$$

The wave length is then divided into  $N$  segments of  $\Delta x$  each. The small time interval,  $\Delta t$  that the particle will travel a distance  $\Delta x$  can be computed. The net particle displacement as well as the net velocity is obtained if the computation is carried out over one wave cycle, i.e.,

$$U(\bar{z}') = \frac{1}{\sum \Delta t_j} \sum u(x_i, z'_i) \Delta t_i \quad (I-9)$$

where  $\Delta t_i = \Delta x_i / u_i$ ,  $\bar{z}'$  denotes the mean elevation of the streamline followed.  $M$  is then calculated by streamline followed.  $M$  is then calculated by

$$M = \rho \sum_{j=1}^N [U(\bar{z}'_j) - U(\bar{z}'_{j+1})] (z'_j - z'_{j+1}) \quad (I-10)$$

### Mass Transport

To check the validity of the above numerical scheme, the mass transport computation using Eq. (I-10) is compared with Dalrymple's Eulerian computation. Column 6 and 7 of Table I.1 list the mass transport calculated by these two different methods (col. 6 - present; col. 7 - Dalrymple). The orders of wave theory

Table I.1  
Lagrangian vs. Eulerian Mass Transport  
by Stream Function Theory

CASE	1 H (m)	2 T (s)	3 h (m)	4 $a^2 \sigma k$ (m/s)	5 kh	6 $M/\rho_{Lag}$ (m/s)	7 $M/\rho_{Eul}$ (m/s)
A-1	10.24	10	30.48	1.492	1.246	16.63	16.54
C-1	5.32	10	30.48	0.203	1.369	2.47	2.47
C-2	6.10	10	30.48	0.261	1.363	3.22	3.21
C-3	9.10	10	30.48	0.574	1.332	7.01	7.00
C-4	10.63	10	30.48	0.765	1.313	9.25	9.23
C-5	16.14	10	30.48	1.656	1.233	17.78	17.63
C-6	21.29	10	30.48	-	-	-	28.59
B-1	1.92	10	3.05	0.058	0.306	0.414	0.412
D-1	0.60	10	3.05	0.006	0.346	0.071	0.070
D-2	0.91	10	3.05	0.014	0.336	0.145	0.144
D-3	1.91	10	3.05	0.024	0.327	0.222	0.221
D-4	1.52	10	3.05	0.038	0.317	0.315	0.313
D-5	1.77	10	3.05	0.050	0.310	0.381	0.378
D-6	2.38	10	3.05	0.087	0.297	0.478	0.460

calculation were 17 and 13 for  $h/gT=0.00311$  (cases A and C), and  $h/gT=0.0311$  (cases B and D), respectively. A wave length is divided into 72 equally spaced segments. As shown in the table, only negligible difference present.

The profiles of Lagrangian mass transport for a wide range of  $kh$  values are given in Fig. I.1. The profiles of Stokes theory are also given for comparison. For deepwater cases, both profiles resemble each other. When  $kh$  decrease, the difference between these two profiles becomes larger. The Stokes profile becomes more and more uniform over the depth. The stream function profile, on the other hand, shows a very strong forward drift near the free surface. Since both theories do not consider the boundary effects, no-slip condition at the bottom boundary is not satisfied. Table I.2 summarize the conditions and the results presented in Fig. I.1.

Table 1.2

Comparison between Mass Transport Computed by Stokes Theory  
and Stream Function Theory

CASE	1 H (m)	2 T (s)	3 h (m)	4 $a^2\sigma k$ (m/s)	5 kh	6 $\frac{M}{a^2\sigma k(\rho h)}$	7 $\frac{M}{a^2\sigma k(\rho h)}$
A-1	15.24	10	30.48	1.492	1.246	0.390	0.474
B-1	6.29	10	3.05	0.058	0.306	2.411	5.505
E-1	0.050	0.44	0.15	0.155	2.658	0.155	0.190
E-2	0.094	0.70	0.15	0.157	1.217	0.368	0.490
E-3	0.111	0.99	0.15	0.098	0.764	0.613	1.017
E-4	0.116	1.40	0.15	0.050	0.503	1.000	2.140
E-5	0.118	2.21	0.15	0.020	0.299	1.953	5.758
E-6	0.118	3.12	0.15	0.009	0.205	3.258	12.064
E-7	0.118	4.42	0.15	0.005	0.156	12.000	20.712

Column 6: Stream function theory

Column 7: Stokes theory

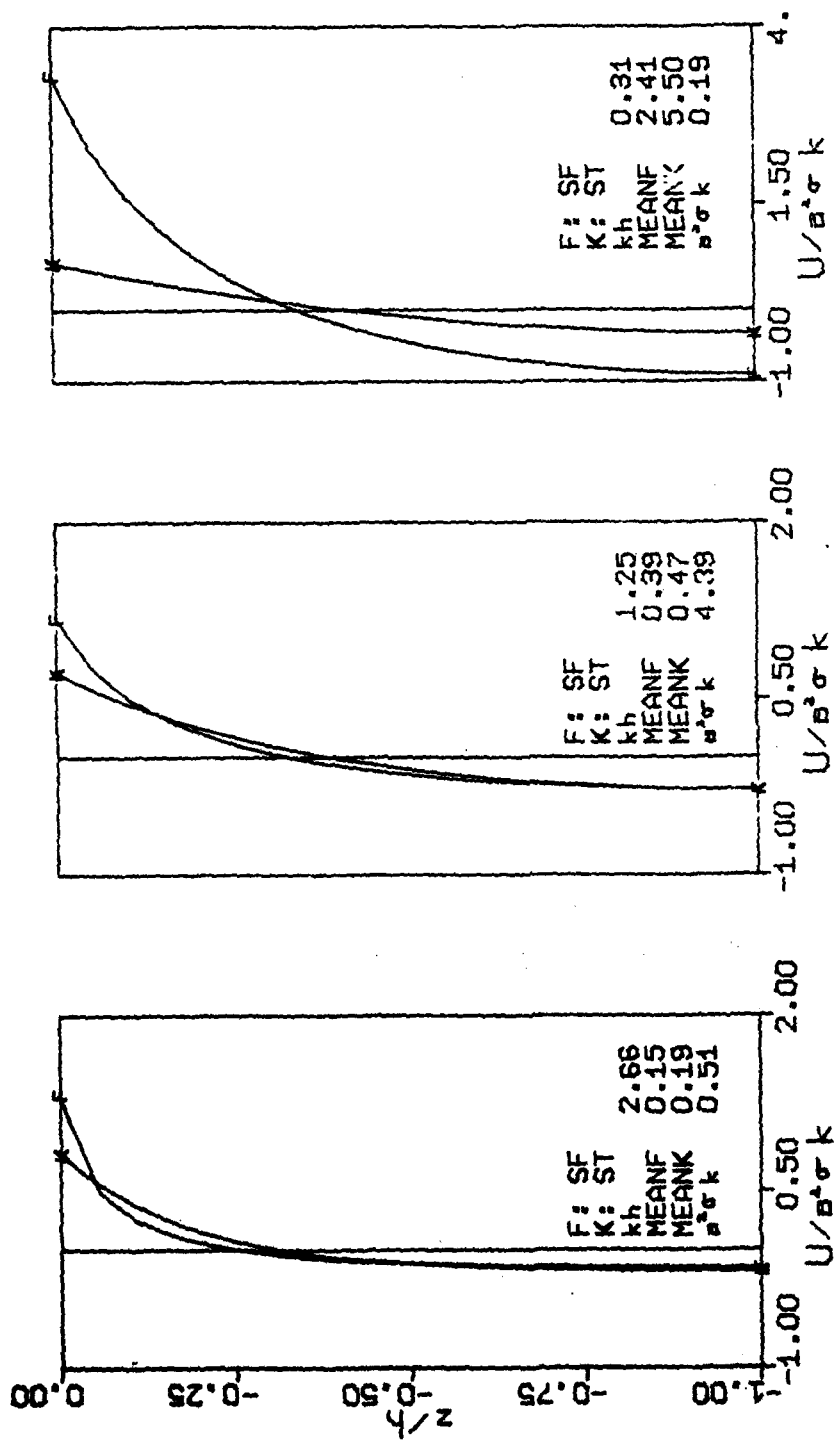


Fig. I.1 Comparison of stream function drift velocity with Stokes solution.

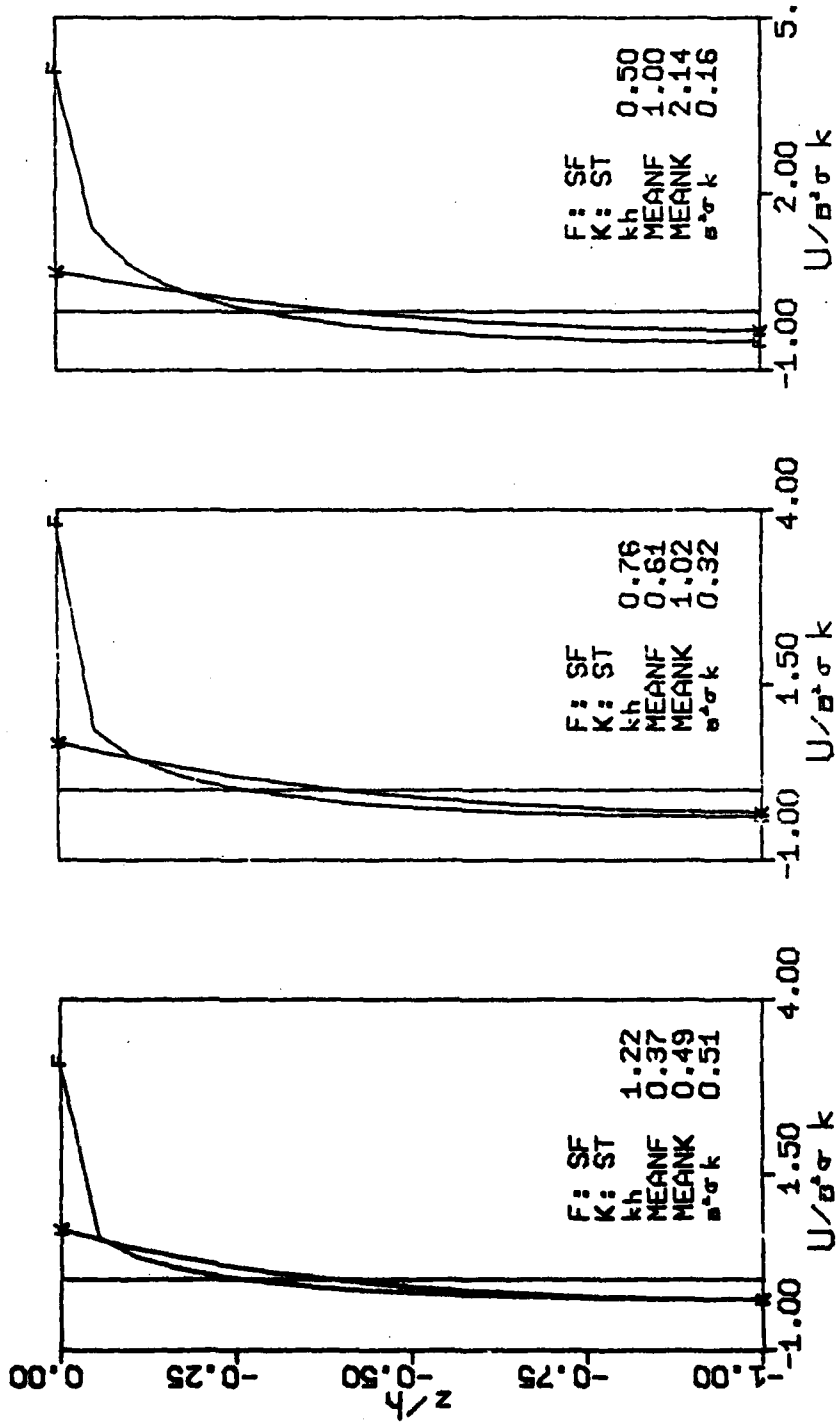


Fig. I.1 (continued)

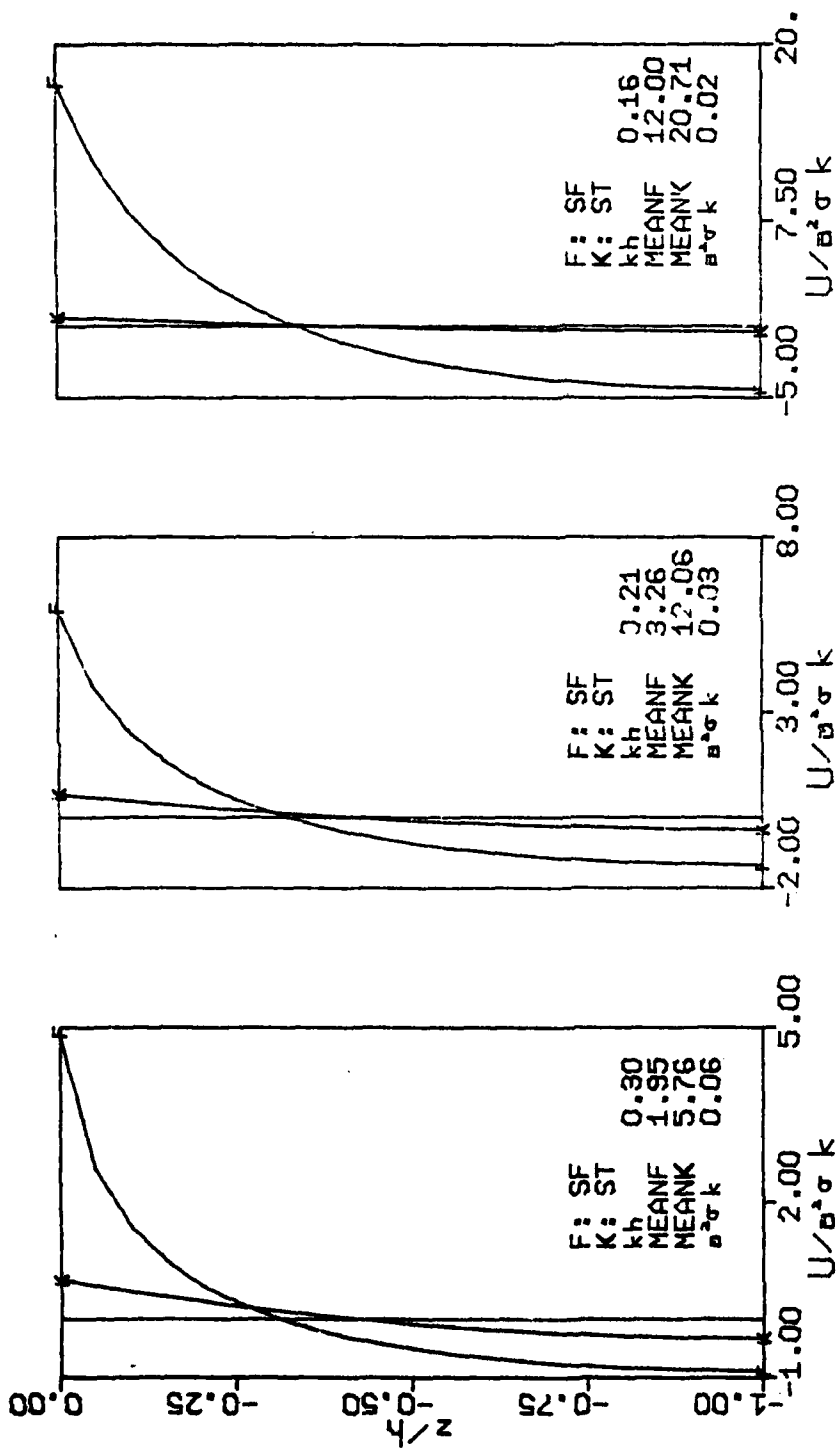


Fig. I.1 (continued)

Distribution

Office of Naval Research  
Coastal Science Program  
Code 42205  
Arlington, VA 22217

Defense Documentation Center  
Cameron Station  
Alexandria, VA 22314

Director, Naval Research Lab.  
ATTN: Technical Information Officer  
Washington, D. C. 20375

Director  
Office of Naval Research Branch Office  
1030 East Green Street  
Pasadena, CA 91101

Chief of Naval Research  
Code 100M  
Office of Naval Research  
Arlington, VA 22217

Office of Naval Research  
Operational Applications Division  
Code 200  
Arlington, VA 22217

Office of Naval Research  
Scientific Liaison Officer  
Scripps Institution of Oceanography  
La Jolla, CA 92093

Director Naval Research Laboratory  
ATTN: Library, Code 2628  
Washington, D. C. 20375

ONR Scientific Liaison Group  
American Embassy - Room A-407  
APO San Francisco, CA 96503

Commander  
Naval Oceanographic Office  
ATTN: Library, Code 1600  
Washington, D. C. 20374

Naval Oceanographic Office  
Code 3001  
Washington, D. C. 20374

Chief of Naval Operations  
OP 987P1  
Department of the Navy  
Washington, D. C. 20350

Oceanographer of the Navy  
Hoffman II Building  
200 Stovall Street  
Alexandria, VA 22322

Naval Academy Library  
U. S. Naval Academy  
Annapolis, MD 21402

Commanding Officer  
Naval Coastal Systems Laboratory  
Panama City, FL 32401

Director  
Coastal Engineering Research Center  
U. S. Army Corps of Engineers  
Kingman Building  
Fort Belvoir, VA 22060

Officer in Charge  
Environmental Research Productn Felty.  
Naval Postgraduate School  
Monterey, CA 93940

Director  
Amphibious Warfare Board  
U. S. Atlantic Fleet  
Naval Amphibious Base  
Norfolk, Little Creek, VA 23520

Commander, Amphibious Force  
U. S. Pacific Fleet  
Force Meteorologist  
Comphibpac Code 25 5  
San Diego, CA 93155

Librarian, Naval Intelligence  
Support Center  
4301 Suitland Road  
Washington, D. C. 20390

Commanding Officer  
Naval Civil Engineering Laboratory  
Port Hueneme, CA 93041

Chief, Wave Dynamics Division  
USAE-WES  
P. O. Box 631  
Vicksburg, MS 39180

Dr. Douglas I. Inman  
University of California A-009  
Shore Processes Laboratory  
La Jolla, CA 92093

Commandant  
U. S. Coast Guard  
ATTN: GECV/61  
Washington, D. C. 20591

Dr. Bruce Heyden  
Dept. of Environmental Sciences  
University of Virginia  
Charlottesville, VA 22903

Office of Research and Development  
%DS/62  
U. S. Coast Guard  
Washington, D. C. 20591

National Oceanographic Data  
Center %D764  
Environmental Data Services  
NOAA  
Washington, D. C. 20235

Prof. Dr. Fuehrboeter  
Lehrstuhl F. Hydromechanik U. Kuestenw  
Technische Hochschule Braunschweig  
Beethovenstrasse 51A  
D-3300 Braunschweig, West Germany

Prof. Dr. Walter Hansen  
Direktor D. Instituts F. Meereskunde  
Universitaet Hamburg  
Heimhuderstrasse 71  
D-2000 Hamburg 13, West Germany

Prof. Dr. Klaus Hasselmann  
Institut F. Geophysik  
Universitaet Hamburg  
Schleuterstrasse 22  
D-2000 Hamburg 13, West Germany

Coastal Studies Institute  
Louisiana State University  
Baton Rouge, LA 70803

Dr. Edward Thornton  
Department of Oceanography  
Naval Postgraduate School  
Monterey, CA 93940

REPORT DOCUMENTATION PAGE		READ INSTRUCTIONS BEFORE COMPLETING FORM	
1. REPORT NUMBER ONR TR. No. 13	7. GOVT ACCESSION NO AD A119906	3. RECIPIENT'S CATALOG NUMBER	
4. TITLE (and Subtitle) Wave Kinematics and Sediment Suspension at Wave Breaking Point		5. TYPE OF REPORT & PERIOD COVERED	
7. AUTHOR(s) Paul Anche Hwang and Hsiang Wang		8. PERFORMING ORG. REPORT NUMBER	
9. PERFORMING ORGANIZATION NAME AND ADDRESS		10. PROGRAM ELEMENT, PROJECT, TASK AREA & WORK UNIT NUMBERS	
11. CONTROLLING OFFICE NAME AND ADDRESS Department of Civil Engineering University of Delaware, Newark, DE 19711		12. REPORT DATE 1982	
14. MONITORING AGENCY NAME & ADDRESS (if different from Controlling Office)		13. NUMBER OF PAGES	
		15. SECURITY CLASS. (of this report)	
		15a. DECLASSIFICATION/DOWNGRADING SCHEDULE	
16. DISTRIBUTION STATEMENT (of this Report)  This report has been approved for public release and sale; its distribution is unlimited.			
17. DISTRIBUTION STATEMENT (of the abstract entered in Block 20, if different from Report)			
18. SUPPLEMENTARY NOTES			
19. KEY WORDS (Continue on reverse side if necessary and identify by block number) Waves, breaking waves, mass transport velocity, suspended sediment, sediment fall velocity, wave spectrum, stream function wave theory, shallow water wave theory			
20. ABSTRACT (Continue on reverse side if necessary and identify by block number) At the point of wave breaking, the flow field and suspended sediment were studied in the laboratory. The flow field was comprised of the instantaneous velocity and the drift velocity on sloping beach. The drift velocity as well as its mean were established through laboratory measurements. A sediment suspension model was proposed based on the diffusion model. Included in the formulations were the fall velocity reduction			

in an oscillating flow field, the sediment grading and the degree of agitation in the flow field.

The wave spectrum at breaking in a finite water depth was discussed and a modified Wallops spectral model developed. In addition, a stream function wave spectrum was calculated, and the two spectra compared to the laboratory data.

Unclassified

SECURITY CLASSIFICATION OF THIS PAGE(When Data Entered)

**LATE  
LME**